Assessing the post-hooking lifetime of hydrogen pipelines damaged by anchors

E.A.M. van Noord

TU Delft

Assessing the post-hooking lifetime of hydrogen pipelines damaged by anchors

by

E.A.M. van Noord

to obtain the degree of Master of Science
at the Delft University of Technology,
to be defended on Thursday August 17, 2023

Student number:	4575202	
Project duration:	April 18, 2022 – August 17, 2023	
Thesis committee:	Dr. C. L. Walters,	TU Delft, daily supervisor
	Dr. J. Jovanova,	TU Delft, committee member
	Dr. L. Pahlavan,	TU Delft, committee member
Company supervisor:	Dr. P. Liu	Intecsea

Cover image: Collection of anchors retrieved from Adobe Stock [1].

Preface

It is my great pleasure to present this thesis, the result of my Master's degree in Offshore and Dredging Engineering at Delft University of Technology. This master thesis presents the research conducted to investigate the behavior of pipelines subjected to external loads, specifically the dragging of pipelines by anchors. The purpose of this work is to gain valuable knowledge with respect to the vulnerability of hydrogen pipelines and to contribute to the development of safe and reliable hydrogen transportation infrastructure.

This study is supervised by Dr. C.L. Walters, Associate Professor Ship and Offshore Structures at the Maritime and Transport Technology Department of Delft University of Technology. This research project has been an incredibly enriching experience, and I am grateful for the opportunity to have pursued this work at Intecsea under the supervision of Dr. P. Liu. I would like to express my sincere thanks to Dr. Liu for his guidance and expertise. I am also grateful for the assistance of Siamak Akhshik, Pedro Ramos, and Renée van Zanten, who provided invaluable help and support during the course of this project.

Finally, I would like to thank my family and friends for their unwavering support and encouragement throughout this journey. Their love and support have been a constant source of strength, and I am deeply grateful for their presence in my life.

Thank you for taking the time to read this preface. It is my hope that this work contributes to gaining valuable knowledge with respect to the vulnerability of hydrogen pipelines and that it accelerates the dialogue in establishing a hydrogen economy.

E.A.M. van Noord
Delft, July 2023

Abstract

The increasing focus on reducing greenhouse gas emissions has led to the attractiveness of offshore hydrogen pipelines in achieving sustainable energy goals. Hydrogen, as a transport medium for energy, offers a viable alternative for transmitting large amounts of energy from offshore facilities to the shore. By storing hydrogen and subsequently converting it back into electricity during periods of peak demand, this approach aligns with the goal of establishing a green, net-zero economy by 2050. However, maritime activities in the proximity of offshore pipelines introduce a serious risk of damaging pipelines by accidental or emergency anchoring scenarios. Damage from dropped or dragged anchors can displace and harm pipelines, leading to environmental risks, safety hazards, and costly repair operations. Comparing hydrogen pipelines to existing oil and gas pipelines, there are significant differences. While oil leakage from anchor hooking poses risks to the environment and marine ecosystems, hydrogen imposes new risk factors which must be taken into account. Hydrogen negatively affects the structural integrity of pipelines, and anchor hooking leads to elevated stress levels within the pipeline material, accelerating fatigue crack growth, and reducing the operational lifespan of the pipeline. This leads to the following research question: *”What is the post-hooking lifetime of a hydrogen pipeline damaged by an anchor?”*

To address this research question, the methodology applied in this thesis consists of two main approaches: numerical simulations and a fatigue crack growth model. The simulations specifically consider an incident where an 8-inch pipeline was damaged by an AC-14 High Holding Power (HHP) anchor. The pipeline is internally pressurised at maximum gauge pressure, and simulations are conducted considering daily and yearly variations in loading cycles, specifically at 10% and 50% pressure reductions. Through these simulations, the stress distribution and variation within the pipeline material resulting from the anchor impact are investigated, providing insights into the behaviour of the pipeline under such conditions. The fatigue crack growth model used in this study is based on the Paris law, which describes the relationship between crack depth and the number of cycles required for crack propagation under cyclic loading conditions. The presence of hydrogen significantly accelerates the rate of fatigue crack growth. As a result, adjustments are made to the Paris law to account for this effect, particularly in determining the range in which the law remains applicable. The crack growth analysis focuses on determining a critical crack depth, which could possibly lead to pipeline failure. A Failure Assessment Diagram (FAD) is used to determine the maximum allowable crack size, ensuring the safety of the pipeline. The FAD, along with the wall thickness of the pipeline, serves as a critical criterion for assessing structural integrity. The remaining lifetime of the pipeline following an accident depends on which criterion, either the FAD or the wall thickness, indicates failure first.

The crack growth analysis conducted in this research reveals that as the crack depth progresses under the influence of hydrogen, it eventually reaches a critical depth that introduces a potential risk of pipeline failure. Specifically, when considering yearly pressure variations, the crack reaches this critical depth in slightly over 8 years. Although the attained crack depth at this point is not yet through-thickness, the crack growth rate experiences a significant increase after 8 years, ultimately resulting in a through-thickness crack 9 years after the initial impact. The findings of this study have significant implications for the future development and maintenance of offshore hydrogen pipelines. By understanding the consequences of anchor hooking incidents and their impact on the operational lifespan of hydrogen pipelines, this research contributes to the development of robust and resilient infrastructure for a sustainable energy future.

Contents

1 Introduction 1

2 Literature review 5
- 2.1 Anchor damage causing pipeline incidents 5
  - 2.1.1 Oil spill off California coast 6
  - 2.1.2 Transmediterranean pipeline system 6
  - 2.1.3 Straits of Mackinac pipeline 7
  - 2.1.4 Probability of anchor dragging 8
- 2.2 Process of pipeline-anchor interaction 9
  - 2.2.1 Pipeline's response to anchor impact 9
  - 2.2.2 Pipeline bending 11
  - 2.2.3 DNV regulations and design requirements 12
  - 2.2.4 Protecting subsea pipelines 13
- 2.3 Hydrogen interaction with pipeline steels 14
  - 2.3.1 Dissolution of hydrogen in steel 14
  - 2.3.2 Distribution of hydrogen in steel 15
  - 2.3.3 Hydrogen embrittlement mechanisms 15
- 2.4 Fatigue of pipelines exposed to hydrogen 16
  - 2.4.1 Fatigue crack growth in inert environments 17
  - 2.4.2 Fatigue crack growth in hydrogen environments 18
- 2.5 Pipeline failure 19
  - 2.5.1 Crack tip plasticity 20
- 2.6 Conclusions and research objectives 20
  - 2.6.1 Conclusions 20
  - 2.6.2 Research objectives 21

3 Methodology 23
- 3.1 Numerical simulations 23
- 3.2 Fatigue crack growth model 23
- 3.3 Flowchart: exchange of information 24

4 Numerical simulations 27
- 4.1 Model set-up 29
  - 4.1.1 Anchor and pipeline design 29
  - 4.1.2 Meshing 30
  - 4.1.3 Anchor and pipeline parameters 31
- 4.2 Analysis settings and boundary conditions 32
  - 4.2.1 Analysis settings 32
  - 4.2.2 Initial and boundary conditions 32
  - 4.2.3 End of the simulation 34

5 Fatigue crack growth model 37
- 5.1 Fatigue crack growth in a hydrogen environment 39
  - 5.1.1 Regions on the fatigue crack growth curve: crack growth rate versus stress intensity range 39
  - 5.1.2 Influence of hydrogen on the Paris law 40
  - 5.1.3 Near-threshold region 41
  - 5.1.4 Crack development 42
  - 5.1.5 Unstable crack growth 45
- 5.2 Model set-up 45
  - 5.2.1 Integration of ANSYS results 45
  - 5.2.2 Calculation procedure 45
  - 5.2.3 Crack growth curve: crack depth versus number of cycles 46
  - 5.2.4 Failure criteria 46

6 Results **51**
6.1 Numerical simulation results 51
6.1.1 Stress variations 51
6.1.2 Mesh independence study 55
6.2 Crack growth model results 56
6.2.1 Maximum allowable crack depth from Failure Assessment Diagram 56
6.2.2 Number of cycles to failure 58

7 Discussion and recommendations **61**
7.1 Relevance 61
7.2 Limitations 62
7.3 Recommendations for future research 63

8 Conclusion **65**

A Anchor and pipeline properties numerical simulations **69**
A.1 Pressure parameters 69
A.2 Pipeline parameters 70
A.3 Anchor parameters 71

B Crack growth model properties **73**
B.1 Crack growth model parameters 73
B.2 Stress intensity magnification factor 75
B.2.1 Membrane stress 75
B.2.2 Bending stress 76

Bibliography **77**

List of Figures

1.1 Global hydrogen transmission pipelines will reach a total length of 200000 km in the NZE Scenario, both offshore and onshore [2]. 1
1.2 Visual representation of the Kvitebjørn gas pipeline at the damage location [3] . 2

2.1 Accidental scenarios causing damage to offshore pipelines [4] 5
2.2 Damage discovery at Transmediterranean Pipeline System [5] 7
2.3 Trapped anchor at Transmediterranean Pipeline System [5] 7
2.4 Enbridge's proposed oil tunnel under the Straits of Mackinac [6] 7
2.5 Overview of a typical subsea pipeline. The figure indicates the section of the pipeline Yutao et al. researched for their probability analysis. [4] 8
2.6 Results from impact and stretch tests [7] 10
2.7 Comparison of actual load scenario versus impact experiments [8] 11
2.8 Bending moment versus curvature [9] 12
2.9 Typical hooking scenario at a free span: a) trawl board approaches pipeline, b) trawl board is lifted off of the seabed as the warp line comes in contact with the pipeline, c) trawlboard slides until stuck at the span shoulder [10] 13
2.10 Schematic view of energy relations. E_a refers to the activation energy for interstitial diffusion. E_b and E_t respectively present the binding and activation energy for trap sites [11]. 15
2.11 Typical fatigue crack growth behavior in metals [12] 17
2.12 Possible effects of hydrogen on fatigue cracking behavior [13] 18
2.13 Tensile curves of different steel grades tested in air and hydrogen: a) X52, b) X65, c) X100 [14] 19
2.14 Tensile curves of a X100 specimen tested in hydrogen at different gas pressures. [14] 20
2.15 Tensile curves of a X100 specimen tested in hydrogen and air at different strain rates [14] 20
2.16 Relative dimensions for the applicability of linear elastic fracture mechanics [15] 20

3.1 Overview of methodology flowchart 25

4.1 Flowchart of the numerical simulation for evaluating anchor hooking incidents on hydrogen pipelines. 28
4.2 YZ plane for anchor-pipe configuration. 29
4.3 XZ plane for anchor-pipe configuration. 29
4.4 Contact between anchor and solid pipeline with beam element. 30
4.5 Quadrilateral dominant meshing on the shank and fluke in ANSYS. 30
4.6 3D 20-node, solid elements are used to specify the mesh in the radial, hoop, and longitudinal direction. 31
4.7 3 elements in the longitudinal direction are defined per pipeline section. 12 elements are defined near the impact point. 31
4.8 Remote points corresponding to the fixed boundary condition, MPC connection, and displacement of the model (from left to right). 33
4.9 MPC connection between the beam element and solid pipeline. 34

5.1 Simultaneous processes of the fatigue crack growth model (left) and fracture assessment (right). 38
5.2 Regions of fatigue crack growth rate in (a) non-embrittling environment and (b) gaseous hydrogen environment. Adapted from [16]. 40
5.3 Internal surface flaw in cylinder orientated axially [17]. 41
5.4 Fatigue striation [18]. 44
5.5 Butt weld as illustrated by $BS7910 : 2013$ [17]. 44
5.6 First phase on the fracture flowchart: define the assessment line and cut-off value. 47

5.7 The Failure Assessment Diagram consists of the assessment line K_r and cut-off value $L_{r,max}$. . . . 48
5.8 Second phase on the fracture flowchart: determine L_r and find K_r associated with σ_{max}. . . . 48
5.9 Third phase on the fracture flowchart: solve the toughness ratio for $K_{I,max}$ and determine the maximum allowable crack depth a_{max} using the equation for the stress intensity factor. . . . 49

6.1 The end of the simulation is determined based on the highest reaction force experienced by the anchor during the simulation. . . . 52
6.2 The pipeline deformation at the end of the simulation at $T = 6.4528\ s$. . . . 52
6.3 Three elements through thickness at the location where the maximum von-Mises stress is obtained. From the location the membrane and bending stresses at different pressure levels are retrieved. . . . 54
6.4 Stress on the inner and outer wall at maximum pressure (p_{max}), 90% pressure ($p_{90\%}$), and 50% pressure ($p_{50\%}$). . . . 55
6.5 The mesh independence study shows that convergence is obtained at a minimum of 5000 elements. . . . 56
6.6 The matching value for K_r can be found by drawing the intersection at $L_r = 0.8$. . . 57
6.7 The crack growth curve with criteria for the maximum allowable crack depth, impacting the determination of post-hooking lifetime. Taking into account daily variations in pressure, the number of cycles until failure is 22421 days. . . . 58
6.8 The crack growth curve with criteria for the maximum allowable crack depth, impacting the determination of post-hooking lifetime. Taking into account yearly variations in pressure, the number of cycles until failure is approximately 8 years. . . 59

7.1 Free body diagram of the forces applied to the pipeline. . . . 62

List of Tables

5.1 Values to the material constants in Equation 5.3 considering the influence of hydrogen on the fatigue crack growth curve [19]. 41

6.1 Values for the inner and outer stress in the x-direction and corresponding membrane and bending stress at p_{max}, $p_{90\%}$, and $p_{50\%}$. 54
6.2 Calculation for the daily and yearly variations in membrane and bending stress. . 54

A.1 Model parameters to define pressure inside the pipeline. 69
A.2 Pipeline parameters and values. 70
A.3 Anchor parameters and values [20]. 71

B.1 Parameters used in the crack growth model. The stress intensity magnification factors at the deepest and surface points are respectively denoted by (d) and (s). 74

List of Abbreviations

3D	Three-dimensional
AIDE	Adsorption Induced Dislocation Emission
API	American Petroleum Institute
ASME B31.12 − 2019	The American Society of Mechanical Engineers B31.12-2019
BS 7910 : 2013	British Standard 7910:2013
DNV	Det Norske Veritas
EBSD	Electron Backscatter Diffraction
FAD	Failure Assessment Diagram
FEM	Finite Element Method
HA − FCG	Hydrogen Assisted - Fatigue Crack Growth
HE	Hydrogen Embrittlement
HEDE	Hydrogen Enhanced Decohesion
HELP	Hydrogen Enhanced Localized Plasticity
HESIV	Hydrogen Enhanced Strain Induced Vacancies
HHP	High Holding Power
IEA	International Energy Agency
MPC	Multi Point Constraint
NDE	Non-Destructive Evaluation
RT	Room Temperature
SCF	Stress Concentration Factor
NZE	Net Zero Emissions

List of Symbols

Greek symbols	
Δa	Increase in crack depth for a sigle cycle step
ΔK	Stress intensity range
ΔK_{th}	Fatigue threshold value
ΔN	Step size for number of cycles
$\Delta\sigma$	Stress range, difference between the maximum and minimum stress
$\Delta\sigma_b$	Stress range, bending stresses
$\Delta\sigma_m$	Stress range, membrange stresses
η	Usage factor
μ	Variable in the Failure Assessment Diagram
ν	Poisson's ratio
ρ	Material density
ρ_{sw}	Seawater density
σ_b	Bending stress
σ_m	Membrane stress
σ_{max}	Maximum stres
σ_{min}	Minimum stress
σ_u	Tensile ultimate strength
σ_Y	Tensile yield strength
$\sigma_{Y,c}$	Compressive yield strength

Roman symbols	
a	Flaw height for surface flaw
a_0	Initial crack depth
a_{max}	Maximum allowable crack depth
B, t	Wall thickness
C_1, C_2, C_3	Material constants for the Paris law under the influence of hydrogen
C_H	Dissolved hydrogen concentration
c	Half flaw length for surface or embedded flaws
c_0	Initial half flaw length for surface or embedded flaws
D, D_o	Outer pipe diameter including coating
d	Deepest point of the flaw
da/dN	Fatigue crack growth rate
E	Young's Modulus
E_b	Hydrogen trap activation energy
E_t	Slope of the stress-strain curve
F	Impact load
F_{far}	Tension in the pipeline far away from contact point
F_{nc}	Tension in the pipeline near contact point
f_w	Correction factor [17]
g	Gravitational acceleration
H_2	Scientific notation to indicate hydrogen gas
H_{abs}	Absorbed hydrogen atoms
H_{ads}	Adsorbed hydrogen atoms
$H_{p,c}$	Permanent dent depth
K	Cyclic strength coefficient
$K_{I,max}$	Maximum stress intensity factor
K_{Ic}, K_{IH}, K_c	Fracture threshold value
K_{max}	Maximum stress intensity in a single cycle
K_{min}	Minimum stress intensity in a single cycle
K_r	Toughness ratio
$K_{r,max}$	Maximum toughness ratio

k_m	Stress magnification factor due to misalignment [17]
k_{tb}	Bending stress concentration factor [17]
k_{tm}	Membrane stress concentration factor [17]
L	Attachment length (of the weld)
L_b	Length of the beam element in ANSYS
L_s	Length of the solid pipeline in ANSYS
L_r	Load ratio
$L_{r,max}$	Cut-off value
M	Bulging correction factor [17]
M_b	Stress intensity magnification factor (bending stress) [17]
M_{kb}	Stress intensity magnification factor as a result of the presence of the weld (bending stress) [17]
M_{km}	Stress intensity magnification factor as a result of the presence of the weld (membrane stress) [17]
M_m	Stress intensity magnification factor (membrane stress) [17]
m	(Anchor) mass
m_1, m_2, m_3	Material constants for the Paris law under the influence of hydrogen
N	Number of cycles
N_f	Variable in the Failure Assessment Diagram
n	Cyclic strain hardening exponent
P'	Weight of the anchor [21]
P_{H_2}	Hydrogen partial pressure
$p_{50\%}$	50% pressure accounting for yearly changes in loading cycles
$p_{90\%}$	90% pressure accounting for daily changes in loading cycles
p_{atm}	Atmospheric pressure
p_e	Hydrostatic pressure
p_g	Gauge pressure
p_i	Design pressure
p_{max}	Maximum pressure
R	Minimum breaking load of chain cable [21]
r_i	Internal pipeline radius
r_o	Outer pipeline radius
S	Solubility constant
s	Surface point of the flaw
T	Time
t_1, t_2	Start and end of impact duration time
v_1, v_2	Initial and final velocity
Y	Stress intensity correction factor

1

Introduction

Relevance

In 2019, The European Green Deal was introduced by the European Commission, striving to make the EU the first climate-neutral continent by 2050. The first objective to reach is to reduce the net greenhouse gas emissions by at least 55% by 2030 compared to 1990 levels [22]. On a global level, the International Energy Agency (IEA) shows a pathway for the global energy sector to achieve net zero CO_2 emissions by 2050, also referred to as the Net Zero Emissions (NZE) scenario. This scenario predicts that hydrogen infrastructure requires an annual investment of \$52bln-\$82bln, mostly for the pipelines and storage of hydrogen. The demand for hydrogen transmission infrastructure experiences rapid growth in the NZE scenario. At present, around 5000 km of hydrogen pipelines have been installed globally. By 2030, the length of hydrogen pipelines is projected to reach approximately 15000 km, and by 2050, it is expected to expand to a total of 200000 km, as illustrated in Figure 1.1. This expansion includes the construction of new pipelines as well as the repurposing of existing ones [2].

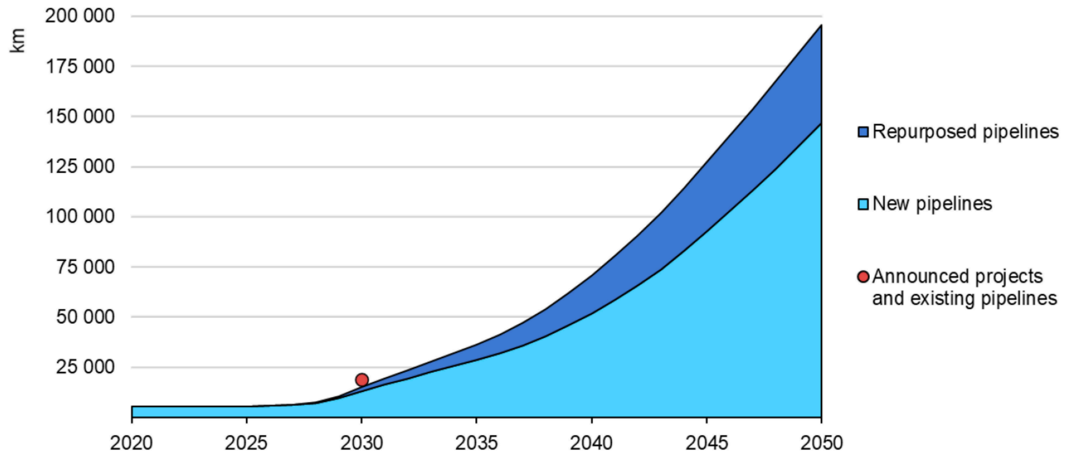

IEA. CC BY 4.0.

Figure 1.1: Global hydrogen transmission pipelines will reach a total length of 200000 km in the NZE Scenario, both offshore and onshore [2].

To reach the goals set by the European Green Deal, by 2050 300 GW of offshore wind energy should be installed in the EU [23]. The expansion of offshore energy production presents challenges in transporting energy to shore. Offshore hydrogen production presents an interesting opportunity in conjunction with offshore wind energy [24] [25]. Energy transport via molecules, in the form of hydrogen, is considered as a viable alternative to transport large amounts of energy to shore. This method involves the generation of hydrogen via water electrolysis, after the desalination of seawater [26]. The power for the offshore production of hydrogen can be generated by offshore wind turbines. Hydrogen gas can be stored and, when energy demand is high, reformed into water to release electricity. In this way, the offshore hydrogen production contributes to the objective of reaching a green, net zero economy by 2050.

Today, damage to offshore pipeline infrastructure, for instance as a result of anchoring incidents or even intentional sabotage, brings significant concerns due to the large financial and environmental risks involved. These risks range from people's safety, environmental impact resulting from leakage, to costly and time-consuming repair operations that lead to financial losses due to operational downtime. Using historical data, Liu et al. presented the leading causes of accidental breakdown for offshore steel pipelines and concluded that anchoring damage is among the 3 most important causes [4]. A dragged or dropped anchor can displace and damage a pipeline and cause permanent impact damage. Such accidents could happen to a pipeline crossing an anchorage area or during emergency ship stopping and mainly due to a vessel operating close to an offshore platform.

One example of an incident that demonstrates the large economic and environmental impact of accidental pipeline damage as a result of an anchoring incident, is the incident that happened at the 30-inch Kvitebjørn oil pipeline in the North Sea. The Kvitebjørn pipeline was dragged out of position by a ship's anchor, and a leak was discovered 10 kilometers from the platform during a routine inspection a year after the incident [27]. As can be seen in Figure 1.2, the anchor chain broke, and the pipeline was released at approximately 53 meters from its initial position. The repair of the damaged pipeline at 210 meters water depth was time intensive, and it took over a year before the pipeline was back in operation [28].

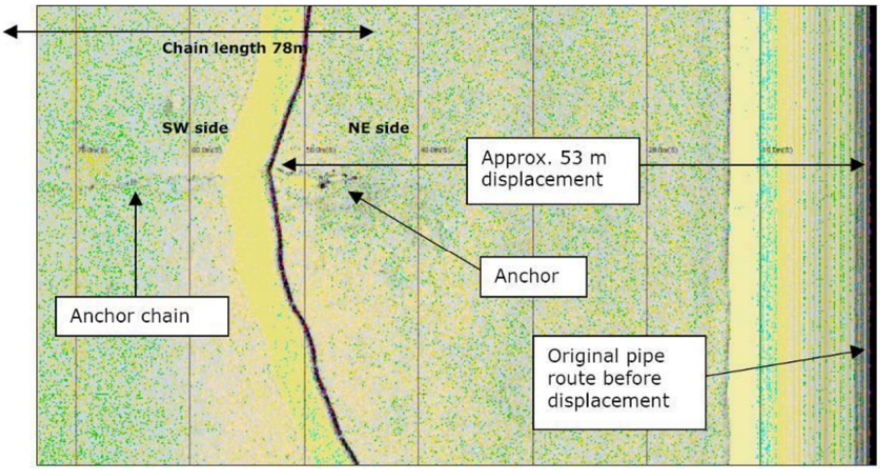
Chain length 78m
SW side
NE side
Approx. 53 m displacement
Anchor
Anchor chain
Original pipe route before displacement

Figure 1.2: Visual representation of the Kvitebjørn gas pipeline at the damage location [3]

.

The anticipated growth of offshore hydrogen infrastructure, specifically focused on offshore hydrogen pipelines, necessitates an assessment of the associated risks. A comparison between oil and gas and hydrogen pipelines highlights significant differences. While the leakage of oil pipelines caused by anchor hooking presents great risks to the environment, human life, and marine ecosystems, the overall risk of pipeline failure as a result of anchor damage is expected to be larger for hydrogen pipelines. Compared to oil, hydrogen has a stronger negative effect on the structural integrity of the pipeline, as fatigue crack growth is accelerated in the presence of hydrogen, thereby reducing the operational lifespan following an anchor hooking incident [16] [29]. Damage to an offshore hydrogen pipeline should be detected in time to prevent detrimental effects on the integrity of the pipeline. If not detected in time, there is a risk of pipeline failure and subsequent shutdown. The downtime resulting from shutting down the pipeline for repairs leads to a significant loss in production and revenue. Additionally, the repair process itself involves various expenses, such as labor, equipment, and materials.

Research question

Considering the increasing focus on reducing greenhouse gas emissions and the attractiveness of offshore hydrogen pipelines in reaching the desired goals in the coming decades, the significant risks to these pipelines should be evaluated. Damage resluting from anchor hooking requires careful consideration, as it is among the 3 most important causes of pipeline failure. The Kvitebjørn pipeline incident demonstrates the economic and environmental consequences that must be accounted for when a gas pipeline sustains damage from a dragged anchor. The transportation of hydrogen through offshore pipelines imposes new risk factors which must be taken into account. When a pipeline is dragged by an anchor, the stress distribution within the pipeline can change significantly, which influences the fatigue behaviour of the pipeline. The presence of hydrogen introduces additional challenges compared to oil pipelines due to its potential to accelerate fatigue of the pipeline material and increase its brittleness, thereby raising the risk of pipeline fracture. While the combustion of hydrogen does not contribute to the emission of greenhouse gases, the leakage of hydrogen into the atmosphere poses risks to the environment. A recent study by Sand et al. shows that the impact of hydrogen leakage on global warming is 12 times stronger than that of CO_2 [30]. Also, from an economic standpoint, it is of great importance to prevent the occurence of fractures in hydrogen pipelines. Repairing a damaged offshore pipeline is costly due to the combination of downtime, resulting in loss of production and revenue, and repair expenses. Therefore, it is essential to gain insight into the expected lifetime of a pipeline after an incident, so that well-informed repair decisions can be made based on a thorough understanding of the impact's effects, minimising the environmental and economic risks. As such, the following research question for the master's thesis project is composed:

"What is the post-hooking lifetime of a hydrogen pipeline damaged by an anchor?"

The following sub-questions are introduced to answer the main research question:

1. What is the resulting stress distribution and variation within the pipeline material after an anchor hooking incident?
2. How is the rate of fatigue crack growth in an anchor hooking problem affected in the presence of hydrogen?
3. When does the crack reach a critical depth, possibly leading to pipeline failure?

To evaluate the structural response and integrity of the system under realistic operating conditions, a recent anchor dragging incident is simulated. This incident addresses an 8-inch buried pipeline in the North Sea. To answer the first sub-question, numerical simulations are used to analyse the structural response of a hydrogen pipeline subjected to anchor impact. The second and third sub-questions require extensive calculations to establish the crack growth curve, specifically determining the maximum allowable crack depth for failure. The results obtained from the numerical simulations assist in determining the post-hooking lifetime of the pipeline via the crack growth model.

Overview

Chapter 2 offers an in-depth exploration of the relevant literature prior to delving into the research question. This literature review is structured to provide an understanding of the anchor hooking problem for hydrogen pipelines, discussing incidents caused by anchor impact, the anchor-pipeline interaction process, the interaction of hydrogen with pipeline steels including hydrogen embrittlement, fatigue crack growth in different environments, and pipeline failure. The methodology of this research is elaborated on in Chapter 3. The methodology consists of two primary components: the numerical simulations executed by ANSYS, as outlined in Chapter 4, and the establishment of a fatigue crack growth model in Matlab to assess the post-hooking lifetime, as discussed in Chapter 5. The results of both processes are presented in Chapter 6. Subsequently, Chapter 7 discusses the study's findings and provides recommendations for future research. Finally, Chapter 8 discusses conclusions and answers the research question.

2

Literature review

The first chapter of this master's thesis outlines the most important findings of the literature review that has been conducted. The focus of the literature review is to fully comprehend the problem of anchor dragging and the effects on hydrogen pipelines as a consequence of uncontrolled dragging across the seabed. It is most likely that the anchor chain will break during anchor dragging and the pipeline (and anchor) will be dropped on the seabed. The question rises whether the pipeline has the capacity to survive the rapid large plastic deformation. If the pipeline survives the impact of the anchor hooking, it is expected that the damage will influence the operational life of the pipeline.

2.1. Anchor damage causing pipeline incidents

Based on an analysis of submarine pipeline failure accident statistics , third-party damage and corrosion are the main causes of submarine pipeline failure. Moreover, the impact of an anchor is a primary risk of third-party damage [8]. Liu et al. [4] looked at historical data and concluded that a large number of accidents to offshore pipelines were caused by impact, ship anchoring, and corrosion, as shown in Figure 2.1. Therefore, the impact of an anchor is one of the factors that must be taken into consideration to guarantee the safe operation of submarine pipelines.

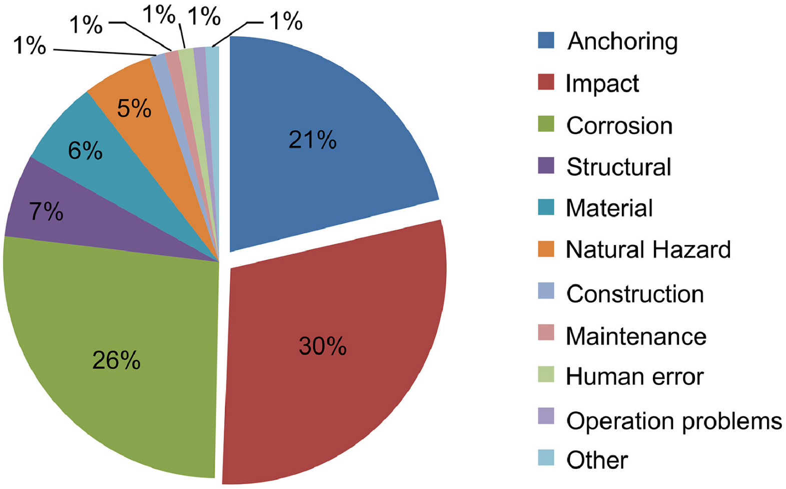

Figure 2.1: Accidental scenarios causing damage to offshore pipelines [4]

.

Sriskandarajah and Wilkins [31] consider two cases whereby a ship can drag its anchor across a pipeline: a ship either attempts to anchor in the vicinity of a pipeline or its anchor slips resulting in uncontrolled drifting of the ship. The first scenario is referred to as emergency anchor dragging and is related to different emergency situations, such as mechanical failure, bad weather and collision. The second scenario, commonly known as accidental anchor dragging, refers to an unintentional drop of the anchor, possibly caused by a failure of the equipment.

Pipeline-anchor interaction is divided into two phases. First initial impact occurs as the anchor contacts the pipeline, after which the pipeline is dragged across the seabed. The initial contact of the anchor may cause local damage due to permanent deformation of the pipe wall or to loss of weight coating. Impact is concerned with the local denting that occurs within the time period immediately following contact of the anchor and the pipeline. The subsequent dragging across the seabed results in bending of the pipeline and large tensile loads.

The transport of existing and future raw materials by offshore pipelines is threatened by the evergrowing frequency of maritime activities. There is an increasing concern about ship-related hazardous events that may damage offshore pipelines, due to anchoring activities and impact consisting of dropped objects and fishing activities. These aforementioned third party activities are the most contributing factor to pipeline failure, with 38% occurrence [32] [4].

Repair of a pipeline is a challenging and critical operation. Several experiences point out that anchor hooking causes a significant lateral displacement together with local dent and out-ofroundness and sometimes, as in the case described in this paper, the damage can be extensive requiring the replacement of more than a few pipe joints [5]. The impact could cause leakage of the pipeline, resulting in a huge environmental disaster and heavy economic losses. Investigations and assessments of several incidents caused by anchor impact are summarized below.

2.1.1. Oil spill off California coast

A 16-inch steel offshore oil pipeline, with a wall thickness of 12.7 mm and covered in 25.4 mm of concrete, off the southern California coast was likely damaged by a ship's anchor several months to a year before the leak was discovered in October 2021 [33]. The pipeline runs along the ocean floor from the Elly platform, about 14.5 kilometers offshore in a water depth of 78 meters, then heads toward port.

Investigators said a large section of the pipeline was bowed after being struck and displaced 32 meters across the ocean floor. The incident caused at least 90,000 liters of oil to spill into the Pacific Ocean, when a 13-inch crack in the pipeline began leaking oil.

The operator of the pipeline, Amplify, has received a permit from the US Army Corps of Engineers to proceed with repair plans that were reviewed and approved by federal pipeline safety regulators earlier this year. The repair will involve removing the damaged segments of the pipeline from the ocean floor and the installation of replacement segments. Additionally, Amplify has agreed to install a new leak detection system and to increase inspections along sections of the pipeline.

2.1.2. Transmediterranean pipeline system

On December 19, 2008 major damage occurred at two of the five pipelines of the Transmediterranean Pipeline System [5]. A 110,000 tonnes tanker crossed the pipelines' route with one of the anchors dragging across the seabed. A 26-inch pipeline was critically damaged to catastrophic failure, and the following 20-inch pipeline was severly bent and displaced more than 40 meters from its original position by the ship's 12 ton anchor. Subsequently the anchor chain snapped, leaving the anchor trapped underneath the pipeline (Figure 2.3), and beneficially causing the remaining lines to stay intact.

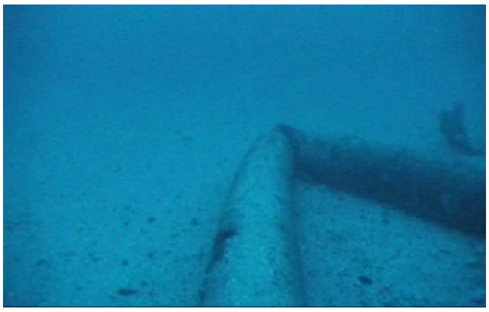

Figure 2.2: Damage discovery at Transmediterranean Pipeline System [5]

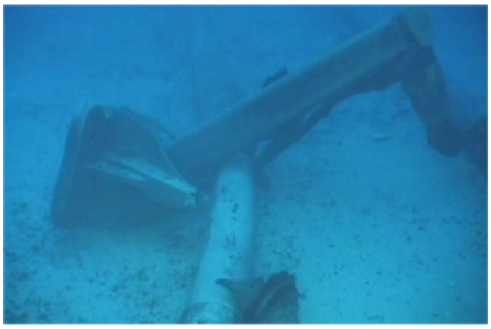

Figure 2.3: Trapped anchor at Transmediterranean Pipeline System [5]

Detailed survey was conducted in order to measure the actual pipeline layout, to evaluate the out of roundness in correspondence of anchor impact and to verify with close visual survey the possible presence of dents and gouges. To continue safely operating the system, both the 26-inch and the 20-inch pipeline had to be repaired. Unlike the severly damaged and partially flooded 26-inch pipeline, the 20-inch pipeline did not show any leak and, hypothetically, it could safely resume operating under protective measures. As it was not possible to quantify the structural integrity of this pipeline to endure operating loads for the remaining operating life, the pipeline had to be repaired. The pipeline system was operational again nine months after the accident.

2.1.3. Straits of Mackinac pipeline

The Line 5 pipeline in the Straits of Mackinac, the connecting waterway between Lakes Michigan and Hurron of the Great Lakes, was built in 1953 and designed to last 50 years. Line 5 moves almost 90 million liters of oil and natural gas liquids per day. The 30-inch steel pipeline splits into two 20-inch pipelines when crossing the Straits of Mackinac. Meanwhile, the pipeline is exceeding its projected operational life of 50 years and has failed at least 33 times since 1968. Operating in a busy waterway, makes the pipeline vulnerable to anchor strikes, which puts the Great Lakes at great risk [6]. On April 1, 2018, an anchor strike damaged Line 5 and nearby electric cables along the lake bottom. A tugboat was held responsible for the release of approximately 2300 liters of toxic coolant and insulating fluid. The operator of Line 5, the Canadian corporation Enbrigde, proposed to build a replacement pipeline in a new tunnel with concrete walls, eliminating the possibility of an anchor strike, see Figure 2.4.

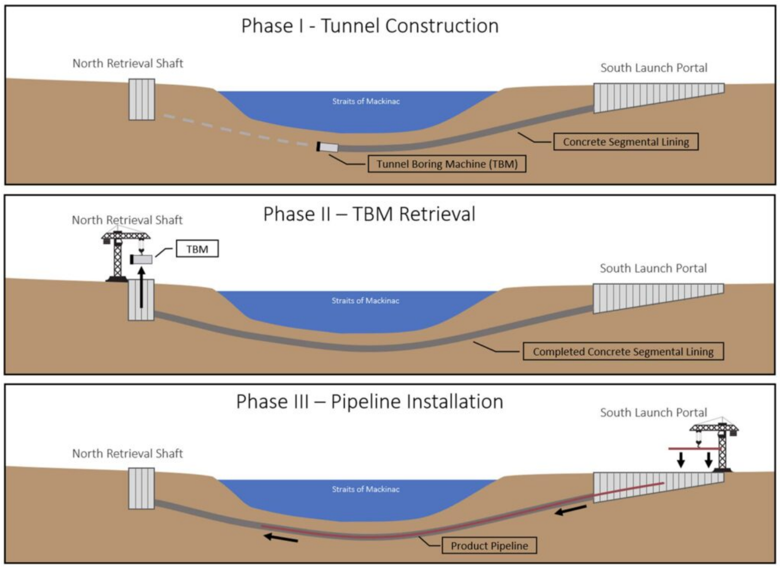
Phase I - Tunnel Construction
North Retrieval Shaft
South Launch Portal
Straits of Mackinac
Concrete Segmental Lining
Tunnel Boring Machine (TBM)
Phase II – TBM Retrieval
North Retrieval Shaft
TBM
South Launch Portal
Straits of Mackinac
Completed Concrete Segmental Lining
Phase III – Pipeline Installation
South Launch Portal
North Retrieval Shaft
Straits of Mackinac
Product Pipeline

Figure 2.4: Enbridge's proposed oil tunnel under the Straits of Mackinac [6]

.

2.1.4. Probability of anchor dragging

As demonstrated by the aforementioned cases, pipeline damage due to anchor dragging can have severe consequences. Additionally, as demonstrated by Figure 2.1, anchoring is one of the most occuring causes for pipeline damage. In this research, anchoring is regarded as the impact from anchor dragging. Two different types of anchor dragging are considered, when evaluating the probability this kind of impact occurs during the operational life of a pipeline. Current risk assessment research analyses the following types of anchoring scenarios [34]. A ship could hit a pipeline as a result of ordinary, planned anchoring, either in an authorized area crossed by a pipeline or in an area of offshore activities (eg. pipelaying operations or an offshore platform). A different scenario is anchoring in case of an emergency. Threatening situations onboard, which may seriously harm the safety of the people or the ship, can lead to anchoring in an unpredicted area.

From incident statistics it is difficult, to distinguish between the accidental and the emergency dragged anchor, due to lack of details in the incident records [35]. Generally, it is assumed ships would deploy their anchor on purpose only if their anchors are capable of reaching the seabed and thus, most researches on the probability of anchor hooking focus on emergency anchoring accidents.

To assess the risks to pipelines, Yutao et al. [2] assumed that accidents occur primarily because of ship anchors and fishing activities. Figure 2.5 shows the section of an offshore pipeline they considered in their research and provides a comprehensible overview of a pipeline's route from an offshore platform to onshore. This middle section considered by Yutao et al. is minimally affected by offshore platform operations and onshore activities.

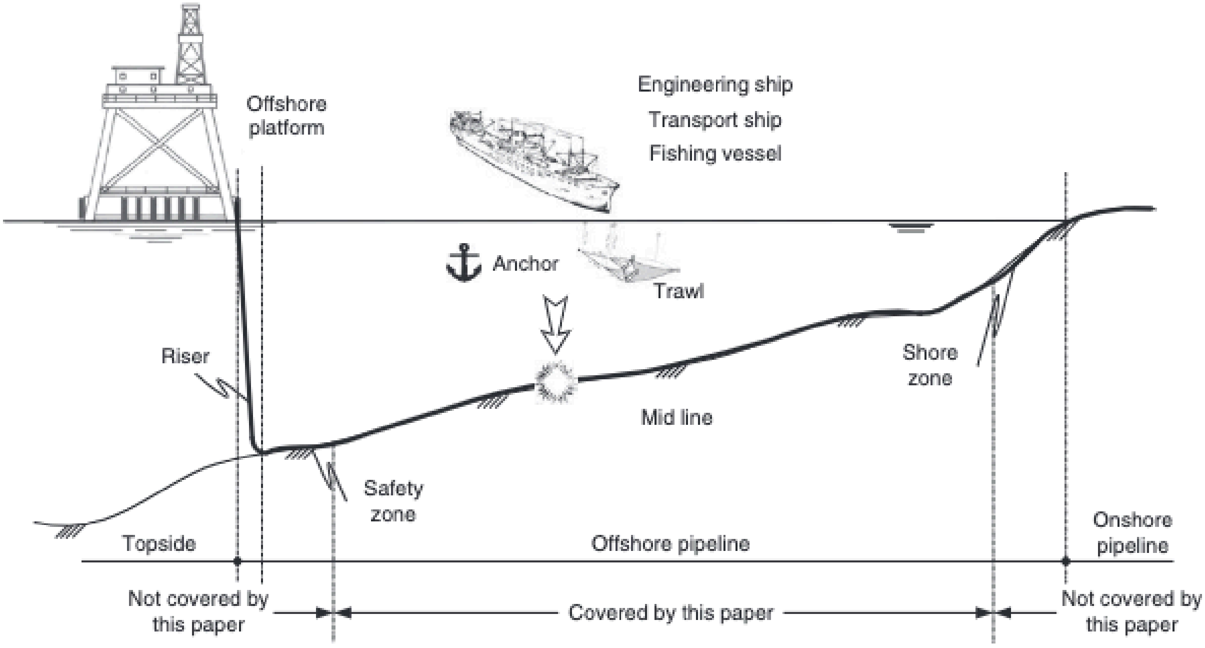

Figure 2.5: Overview of a typical subsea pipeline. The figure indicates the section of the pipeline Yutao et al. researched for their probability analysis. [4]

.

Multiple risk studies analysing anchor damage to offshore pipelines are accomplished to decide on minimum burial depth and protection cover requirements. Hvam et al. [34] conducted a risk study to analyse anchor damage to offshore pipelines as a result of an emergency situation onboard; this could either be a failure of propulsion or steering machinery or a collision. It was concluded that anchor damage to pipelines is a major risk during pipeline construction and operations.

The risk study by Hvam et al. assesses the main parameters contributing to the frequency of pipeline-anchor interaction and pipe damage. The frequency of emergency anchoring operations is a function of ship traffic data at a specific location, failure rates regarding situations that lead to emergency anchoring and procedures following an emergency situation. This approach results in a first estimate for the frequency of pipeline-anchor interaction in a specific area. Eventually, soil conditions, anchor and ship characteristics determine whether an anchor hooks onto a pipeline and, consequently, drags the pipeline across the seabed. Generally, dense sands and stiff clays could cause the anchor to work improperly [31].

2.2. Process of pipeline-anchor interaction

The anchor dragging problem can be roughly divided in four different elements. First, an anchor can affect an offshore pipeline as a result of either accidental or emergency anchoring. This has been extensively demonstrated in the previous section by means of different pipeline-anchor incidents over the past years.

As mentioned earlier, a ship would only make use of their anchor on purpose if it is capable of reaching the seabed. Thus, in most instances, a ship will first reduce speed and then drop its anchor in order to get a high probability of successful anchoring. If there is a pipeline lying within the drag length, there is a risk of hooking incidents. As the ship is decelerating, this leads to uncontrolled dragging of the pipeline. The pipeline is dragged across the seabed until it either fails immediately or is released by the ship. The pipeline snaps back, but is usually displaced from its original position.

If the pipeline survives the impact of the anchor hooking, it is expected that the damage will influence the operational life of the pipeline. After the impact, the welds should withstand fatigue loading. As the pipelines taken into consideration are fully saturated with hydrogen, the next step is to investigate the influence of hydrogen on metals, since it has a deteriorating effect on the material properties.

Finally, the question arises whether the pipeline fails or is able to withstand the impact under the presence of hydrogen. Failure modes for subsea pipelines consist of hydrogen embrittlement, fatigue cracking, rupture and leakage.

This chapter focuses on the first two steps of the process, namely the initial response of the pipeline due to anchor hooking, and consequentely dragging and snap back. The succeeding steps are discussed in Chapter 2.3, which explains the deteriorating effect hydrogen has on steel, in Chapter 2.4, focusing on the fatigue crack growth in the presence of hydrogen, and in Chapter 2.5, concluding with the failure of the pipeline.

2.2.1. Pipeline's response to anchor impact

Anchor-pipeline interaction may be divided into two phases: first, the initial impact as the anchor contacts the pipeline and, second, the subsequent dragging of the pipeline across the seabed. After releasing the anchor, it is dragged by the decelerating ship until the pipeline is hooked. When the dragging anchor hits the pipeline, it has a kinetic energy which is related to the actual velocity of the ship and the anchor's weight. This kinetic energy is assumed to be fully transferred to the pipeline.

The kinetic energy is described by AL-Whartan [36], as shown in Equation 2.1, where m equals the anchor's mass and v_1 and v_2 respectively initial and final velocities. Direct impact force on the pipeline is represented by an impulse loading , I, which is equal to the integral of the impact load F over the entire impact duration from time t_1 to t_2:

$$I = \int_{t_1}^{t_2} F dt = mv_2 - mv_1 \tag{2.1}$$

Assuming the dragged anchor hooks the pipeline, it applies a point load to the pipeline and makes the pipeline deflect as a beam. Both Hvam [34] and Sriskandarajah [37] further describe this impact. Sriskandarajah studies the interaction between a pipeline and fishing gear, which can be considered similar to the impact of a dragged anchor. Impact is concerned with the local denting that occurs within the time period immediately following contact of the fishing gear and the pipeline. The initial contact of the anchor may cause local damage due to permanent deformation of the pipe wall or to loss of weight coating.

Martin Kristoffersen from the Norwegian University of Science and Technology published multiple researches on offshore pipelines subjected to accidental loads. One of his researches on damage caused by trawl gear impact, substantiates Sriskandarajah's findings on the impact from fishing gear [7]. The experiments consist of two main steps: A simply supported pipe made from X65 steel was first struck by a trolley with a given mass and velocity in the pendulum accelerator. The second step consists of straigthening the pipe using a tension machine. Two pipes were impacted at different velocities and subsequently stretched. The results for the different impact velocities are shown in Figure 2.6.

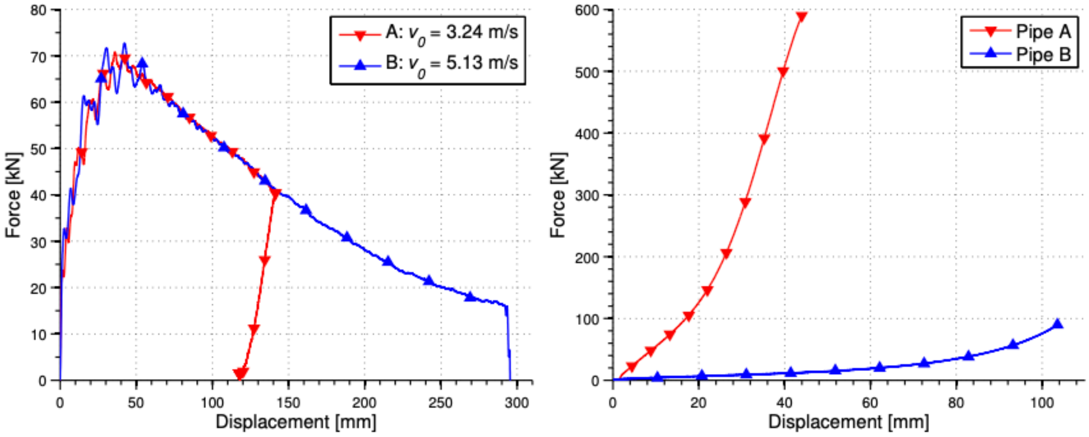

(a) Impact data (b) Stretch data

Figure 2.6: Results from impact and stretch tests [7]

The experiments show that the force increases in the beginning of the impact when the deformation is still local, and starts to decrease when a transition is made from local to global deformation. The remainder of the kinetic energy after reaching the peak, is mainly absorbed by global deformation.

The ultimate goal during the impact experiments was to simulate the actual load scenario's corresponding to impact and rebound and straightening. The main difference between the experiments and a real case is the absence of axial forces as the pipeline is deformed. This difference is explained in detail by Kristoffersen [8] and visualised in Figure 2.7. As can be seen, the real case is divided in three different stages, namely *(1)* local denting, *(2)* occurence of large global deformations as the impact continues and *(3)* straightening of the pipe. During the experiments *(1)* and *(2)* occur simultaneously. The axial forces developed in the real case are absent during the experiments, because the test pipe is simply supported. The straightening of the pipeline during the experiments corresponds to the release and snap back to its initial position due to the axial forces in the real case.

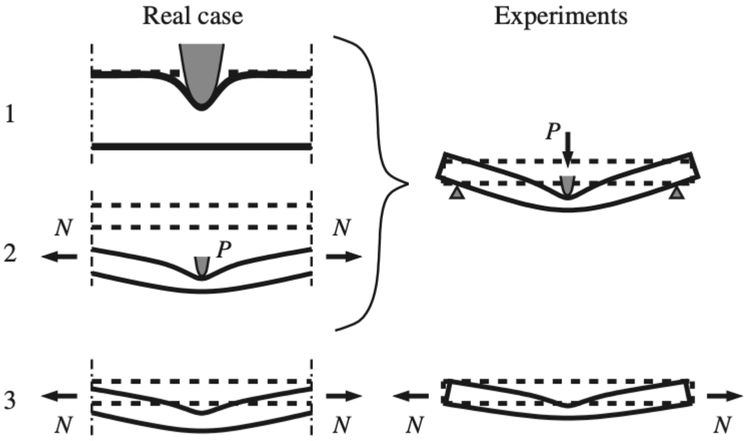

Figure 2.7: Comparison of actual load scenario versus impact experiments [8]

2.2.2. Pipeline bending

During its operational life, a pipeline has to endure extreme loads. The main load effect on offshore pipes is bending combined with longitudinal forces while subjected to external hydrostatic pressure during installation, and internal pressure while in operation. Hvam emphasizes the importance of the actual pipeline capacity to absorb the impact [34]. Impact of a dropped anchor causes mainly local deformation, as an inward deflection of the damaged pipeline is observed. The consequential dent depth depends on the available kinetic energy as described previously. For a dragging anchor, it is assumed that the pipeline can endure the first impact of the anchor hooking onto the pipeline, which initiates the deflection process. At first, the pipeline is subjected to global deformation. In the elastic range of the material, there is no permanent change. Increasing the load makes the hooking point move in the direction of the applied force, which also causes a larger part of the pipeline to deflect. As the hooking load increases, the large deflections trigger the membrane effect, generating a stiffening of the pipe to the additional loads.

The different stages during a hooking event can be seen in Figure 2.8. The proportional relationship between bending moment and curvature is interestingly described by Hauch and Bai [9]. The two curves show the development of the bending moment while an increasing curvature is applied. The dashed line is representative for pipelines that, in addition to bending are subjected to longitudinal force and/or pressure. Longitudinal forces and pressure are absent for the solid line.

As the pipeline is hooked and, consequently, dragged across the seabed, it is subjected to excessive bending. Until the point of *Linear limit* has been reached, no permanent deformation occurs and the pipeline will return to its initial shape. After the point of *Ultimate moment capacity* is reached, *Start of catastrophic capacity reduction* occurs immediately since the pipeline is subjected to combined load. On the contrary, for pure bending without the presence of longitudinal forces or pressure, after the ultimate moment capacity is reached, the material softens Eventually, a pipe subjected to increased bending may fail due to local buckling or fracture.

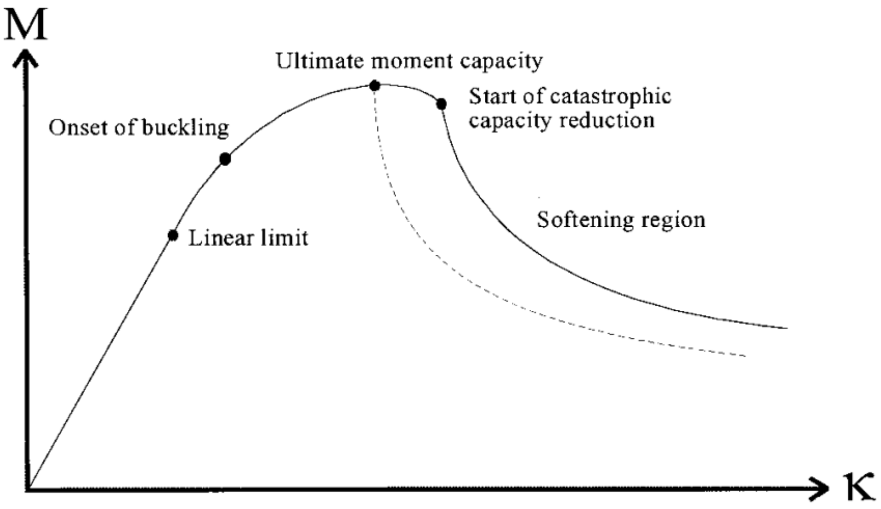

Figure 2.8: Bending moment versus curvature [9]

Several studies focus on pipeline impact from trawl gear or anchors. A load cycle of impact, hooking, pull-over and release has been investigated by Kristoffersen et al. [7]. By conducting both impact experiments and numerical simulations, fracture was observed during stretching for both pipes. Although the results for pipe stretching, which corresponds to the events of pull-over and release, were not adequately represented by the numerical simulations, the force-displacement curves for the numerical simulations were in accordance with the impact experiments. A notable result related to impact velocity, is that the pipe is forced to withstand the load as a bending moment rather than an axial load due to larger deformations.

In his study, AL-Whartan [36] presents the static and dynamic deflections, and axial and bending stresses on three span lengths (14, 28 and 49 meters) of a free span pipeline subjected to three different loading functions analysed by a discrete element method . The three different loading functions he considers are impulse impact, ramp impact and anchor dragging. An unsupported span due to loss of contact with the seafloor can experience excessive stresses due to its weight in addition to other factors such as hydrodynamic forces and impact loads. Freespan can occur when a pipeline is layed on an uneven bottom, or it can develop due to varying erosion and scouring around the pipeline, initiated by waves and current which affect mostly buried pipelines. When an anchor is hooked to a pipeline and drags it out of it position, tension develops in the pipeline. As the ship continues to apply tension on the pipeline, the pipeline deflection, axial and bending stresses continue to build up. For the specific case AL-Whartan investigated, this could result in local pipeline buckling and plastification, if the applied tension continues to increase after 18 seconds. From this research for three different loading functions analysed, it was concluded that, as the span length increases, bending stresses decrease.

2.2.3. DNV regulations and design requirements

Pipeline design to withstand impact from dragging anchors has been researched for many years. As early as 1972, problems from dragging anchors have been recognized as a serious threat to offshore pipelines. Brown [38] describes pipeline design to protect the pipeline from such impact. Important aspects contributing to design desicions, are the marine environment and soil conditions.

Next to the information from the literature, Det Norkse Veritas (DNV) publishes classifications on pipeline design and protection. The design of submarine pipelines is often performed according to the DNV-ST-F101 standard [39], which gives criteria and recommendations on concept development, design, construction, operation and abandonment of submarine pipeline systems. This standard comes with a range of recommended practices, of which DNV-RP-F107 [40] and DNV-RP-F111 [10] focus specifically on pipeline protection.

DNV-RP-F107 makes recommendations for the risk assessment of pipeline protection and includes scenarios that can cause damage to pipelines installed offshore. It states that collisions with anchors are the main cause of damages to pipelines by external forces. A load cycle of impact, hooking, pull-over and release produces a complex stress and strain history which is not particularly well covered in the guidelines.

DNV-RP-F111 contains empirical equations for pipeline denting with regard to interactions between trawl gear and pipelines. The definitions as described in this practice are also applicable to the anchor hooking problem. Although the risk of hooking is relevant for both pipelines laying on the seabed as free span pipelines, free spans represent an increased risk of hooking, as the trawl board (or anchor) digs easier under the pipeline and gets hooked. Figure 2.9 illustrates a typical hooking at a free span.

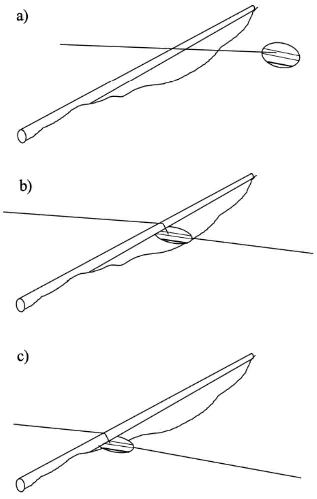

Figure 2.9: Typical hooking scenario at a free span: a) trawl board approaches pipeline, b) trawl board is lifted off of the seabed as the warp line comes in contact with the pipeline, c) trawlboard slides until stuck at the span shoulder [10]

An acceptable design against impact should withstand denting, collapse and fatigue. The maximum accepted ratio of permanent dent depth to the outer diameter of the pipeline is given by the following equation:

$$H_{p,c}/D = 0.05\eta \tag{2.2}$$

This equation uses $H_{p,c}$ to identify the characteristic permanent plastic dent depth, D for the outer diameter of the pipeline and η for the usage factor. Values for η range from 0.0 to 0.7.

2.2.4. Protecting subsea pipelines

A pipeline without any form of protection is easily displaced and damaged by a dragging anchor. Next to that, pipeline characteristics, in terms of buoyant weight and stiffness have a significant effect on the behaviour of a pipeline subjected to third-party activity. The protection of subsea pipelines has been a major subject for research over the years. Anchor damage to offshore pipeline is analysed by risk studies and includes examining potential accidental and emergency scenarios to calculate the anchor-pipeline interaction frequency. Hvam extensively describes different emergency anchoring scenario's to establish a frequency model [34]. Burying or covering the pipeline with rocks are common methods for protection. Not only does this prevent the pipeline from moving, but the extent of pipeline burial or any other form of protection also effects the anchor forces exerted on a pipeline [31].

Brown discusses the various modes of protection that can be used to reduce the risk of damage to an acceptable level [38]. Burying or covering a pipeline with rocks are not always a possibilty due to the marine environment or soil conditions. Appropiate protection methods considered by Brown, are the use of armored concrete coatings and engineered backfill. Important considerations to take into account are the frequency of occurence of a dragged anchor or trawl gear during the pipeline's lifetime, the size of a ship's anchor and the cost of repair in case of damage. Most importantly, sufficient protection causes an anchor to 'walk over' the pipeline without hooking.

Later research from Gaudin et al. confirms what was already assumed and researched by Brown in 1972 [41]. Pipelines may be either buried deeply enough to prevent any interaction with anchors, or protected by a specific rock cover to limit lateral displacements. A complete protection method should provide any insight into the interaction mechanism between the anchor, the chain and the seabed. The conclusions for this research are evident, considering Brown's earlier statements. First, it is necessary to have enough material in front of the pipeline to allow enough room for the anchor to be lifted before it actually reaches the pipeline. Next to that, the size of the rock must be compatible with the size of the chain to limit the penetration of the chain through the rock protection.

Succesful anchoring is highly dependent on the soil conditions. Whereas anchor penetration is limited in dense sandy soils, it is deeper in soft soils. The extent of penetration of an anchor into the seabed will affect the interaction with a pipeline. Selker [42] performed a study on anchor dragging as part of a process on risk based burial depth. In sandy soils, pipeline burial would reduce the likelihood of anchor impact. But a buried pipeline in softer soil is not necessarily safer during an anchor dragging event than a non-buried pipeline. As a partly embedded pipeline is hooked and displaced laterally, it is pulled out onto the seabed and the same conditions apply as for a non-buried pipeline. Considering deeper burial, the critical failure mechanism changes from a global failure mechanism to a more local one and the denting criterion becomes more important. If the surrounding soil supports the cross section in such way that a large local load can develop, the pipeline is more severely damaged.

2.3. Hydrogen interaction with pipeline steels

The previous chapter desribed the anchor hooking problem from the first contact between anchor and pipeline, to dragging the pipeline across the seabed. The relationship between the bending moment and the curvature shows the different stages experienced by the pipeline. This research specifically focuses on anchor dragging of pipelines exposed to hydrogen, which has a deteriorating effect on the mechanical properties of metals.

To better comprehend the interaction of hydrogen with pipeline steels, a complete understanding of the physical processes involved is needed. The first process described is the uptake of gaseous hydrogen through the surface. This process consists of broadly two steps, namely adsportion and absorption.

After the hydrogen atoms are absorbed into the metal, they will move through the structure. The distribution of hydrogen in steel depends on the presence of trappig sites.

The entry of atomic hydrogen into the metal lattice causes loss of ductitliy, strength, and toughness. This phenomenon is known as hydrogen embrittlement (HE) and often causes huge economic losses and even catastrophic damage. Different HE mechanisms will be introduced in this chapter.

2.3.1. Dissolution of hydrogen in steel

Hydrogen dissolved in metals as a result of internal and external hydrogen can afect the mechanical properties of the metals. High-pressure hydrogen gas, electrochemical hydrogen charging and corrosion reactions are the main sources of hydrogen in metals. The uptake of gaseous hydrogen into the metal bulk involves three steps, each described below in consecutive order [43].

The first step is physical adsorption or physisorption. The hydrogen gas comes into contact with the metal surface and is adsorbed due to the van der Waals interactions. This is a reversible process which generally requires a low energy level for adsorption [44].

The adsoprtion process consists of two phases, of which the second is chemisorption. Contrary to physisorption, this is a slow process. It requires high dissociation energy of the hydrogen gas molecules and high adsorption energy. This high energy level depends on the metal-hydrogen and hydrogen-hydrogen bond energies. During this step, the hydrogen gas (H_2) dissociates to two adsorbed hydrogen atoms (H_{ads}), see Equation 2.3 [45].

$$H_2(g) \leftrightarrow 2H_{ads} \tag{2.3}$$

Finally, the adsorbed hydrogen (H_{ads}) is absorbed by the material (H_{abs}). This third step is demonstrated in Equation 2.4. As both equations are reversible processes, the hydrogen atoms can either be absorbed into the bulk (Eq. 2.4) or recombined into hydrogen gas (Eq. 2.3).

$$H_{ads} \leftrightarrow H_{abs} \tag{2.4}$$

Eventually, for high pressure hydrogen gas, equilibrium will be reached between the concentration of hydrogen in the steel and the partial pressure of hydrogen gas in the environment. The dissolved hydrogen concentration (C_H) in a metal follows Sieverts' law [46], which is as follows:

$$C_H = S\sqrt{P_{H_2}} \tag{2.5}$$

This equation uses S to identify the solubility constant and P_{H_2} for the hydrogen partial pressure.

2.3.2. Distribution of hydrogen in steel

Hydrogen can dissolve in a metal through the interactions between hydrogen and material defects, which affects the mechanical properties of the metal [43]. Various types of defects appear in a real crystal structure. Defects are categorized by their dimensions [47].

0-dimensional	point defect, vacancies or interstitial atoms
1-dimensional	line defect, dislocation, micromechanical deformation behavior
2-dimensional	surface defects, grain boundaries, phase boundaries or twin boundaries
3-dimensional	volume defects, voids or precipitates

Hydrogen atoms typically diffuse through the metal via interstitial lattice [48] [11]. However, the diffusion is obstructed by hydrogen atoms residing in hydrogen traps. These traps are known to play an important role in the transport of hydrogen [49]. The above mentioned defects strongly interact with hydrogen and thus act as hydrogen traps. As the potential well for a trap site is deeper than for an interstitial site, this causes the hydrogen atoms to stay longer in the trap site. Hydrogen traps can be divided into reversible and irreversible traps. The distinction is based on the hydrogen trap activation energy E_b. Irreversible trap sites are classified as sites with a very deep potential well, such that there is no possibility for the hydrogen atom to get out of the site. The probability of an atom 'jumping out' of a trap site increases with an increase in temperature. This situation refers to a reversible trap site. Figure 2.10 illustrates schematically the course of the potential energy.

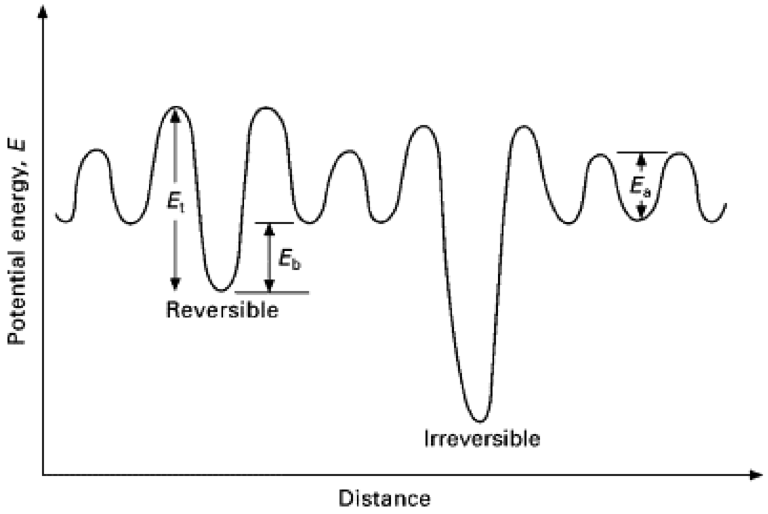

Figure 2.10: Schematic view of energy relations. E_a refers to the activation energy for interstitial diffusion. E_b and E_t respectively present the binding and activation energy for trap sites [11].

2.3.3. Hydrogen embrittlement mechanisms

The phenomenon of hydrogen embrittlement describes the deterioration of mechanical properties of a material due to the interaction with hydrogen. Hydrogen embrittlement is primarily causing issues during transmission and utilization of hydrogen [50]. In the presence of hydrogen, fracture occurs at stresses and/or strains substantially lower than without the presence of hydrogen [51].

The degradation process of hydrogen embrittlement is by far more complex. Several mechanisms have been proposed to explain the phenomena of HE. The following four mechanisms are discussed: hydrogen enhanced decohesion (HEDE), hydrogen enhanced localized plasticity (HELP), hydrogen enhanced strain induced vacancies (HESIV) and adsorption induced dislocation emission (AIDE).

Hydrogen Enhanced Decohesion (HEDE)

The concept of HEDE was introduced in 1926 by Pfeil et al. [43]. The mechanism describes that, under the presence of an increasing hydrogen concentration, also an increase in the weakening of the metallic interatomic bonds takes place. Consequently, brittle cracks initiate and propagate as the cohesive strength at grain boundaries or other interfaces is reduced. High concentrations of hydrogen can be found at several locations. Katzarov and Paxton indicate four locations: (i) crack tips, (ii) ahead of crack tips, where dislocation shielding effects lead to the highest tensile stress, (iii) ahead of crack tips, where particle-matrix interfaces exist, and (iv) regions of maximum hydrostatic stress [52]. Thus far, there is no experimentally demonstrated evidence for the HEDE mechanism. The research presented by Katzarov and Paxton focusses on presenting a theoretical analysis of dissolved hydrogen in α-FE. They found a reduction in the ideal cohesive strength, from 30 to 22 GPa.

Hydrogen Enhanced Localized Plasticity (HELP)

In 1972, Beachem et al. proposed the HELP mechanism [53]. This mechanism was established when tear ridges on brittle fracture surfaces were observed. Katzarov et al. published two researches on hydrogen embrittlement, of which the first is an analysis of hydrogen-enhanced localized plasticity [54]. The interactions between the hydrogen atmosphere and dislocations make this model particularly remarkable. This mechanism suggests that dislocations are unlocked in the presence of hydrogen. This increases the dislocation mobility, which leads to localized plasticity, hence the name of this mechanism. Research by Robertson supports the HELP mechanism. He performed experiments in-situ in a transmission electron microscope (TEM) to investigate the effect of hydrogen on dislocation dynamics, and showed that hydrogen increases the mobility of dislocations [55].

Hydrogen Enhanced Strain Induced Vacanies (HESIV)

The fracture process in the presence of hydrogen can also be described by the HESIV mechanism. A cluster of vacancies, formed during straining, change the material behaviour. The HESIV model was first proposed by Nagumo [56] [57]. An interesting aspect of this model is that degradation is caused by the formation of strain-induced vacancies. This process is accelerated in the presence of hydrogen. Results from hydrogen thermal desorption analysis by Takai et al. show that hydrogen enhances the creation of strain-induced defects [58].

Adsorption Induced Dislocation Emission (AIDE)

The AIDE mechanism was introduced by Lynch in the late 1970's [59]. When Lynch proposed this mechanism, he was examining HE and liquid-metal embrittlement (LME) and observed similarities between the fracture surfaces of both processes. According to Lynch, hydrogen adsorption at the crack tips promotes the nucleation of dislocations, both for HE as LME. The role of hydrogen in dislocation generation was earlier researched by Clum in 1975 [60]. AIDE attributes the formation of dislocations to the weakening of atomic bonds at the surfaces of the crack tip where hydrogen is adsorbed. The mechanism also explains the crack growth, which is induced by the nucleation and growth of microvoids in front of crack tips [61].

2.4. Fatigue of pipelines exposed to hydrogen

From the previous chapter it has become evident that the presence of hydrogen influences the toughness and ductility of the steel dramatically. The mechanical integrity of pipelines transporting hydrogen needs to be validated, which makes it essential to consider hydrogen-assisted fatigue crack growth behavior.

First, it is important to create a general understanding of what happens during fatigue crack growth in inert environments. Three different regions can be distinguished during fatigue crack growth in inert environment, which will be elaborated upon in the first part of this chapter. Next, fatigue crack growth in hydrogen environments is discussed and the concept of hydrogen-assisted fatigue crack growth is introduced.

Finally, an important phase during the anchor dragging process is taken into account, which is the excessive bending of the pipeline. Bending of a pipeline in this specific situation is associated with high strain rates.

2.4.1. Fatigue crack growth in inert environments

As pipelines in operation are subjected to the risk of anchor damage, it is important to consider fatigue. Small defects or cracks are always present, but form a risk, as they can grow under loading. The crack growing with each cycle is known as fatigue crack growth [62]. Fatigue cracks typically initiate near or at stress concentrations that lie on or just below the surface of a material [63].

Figure 2.11 shows the fatigue crack growth curve. The crack growth rate da/dN is plotted against the nominal stress intensity range ΔK ($\Delta K = K_{max} - K_{min}$). As can be seen, the crack growth curve indicates three regions (I, II, III). The characteristics of each region will be discussed below. The following definitions are mostly retrieved from Anderson's book [64].

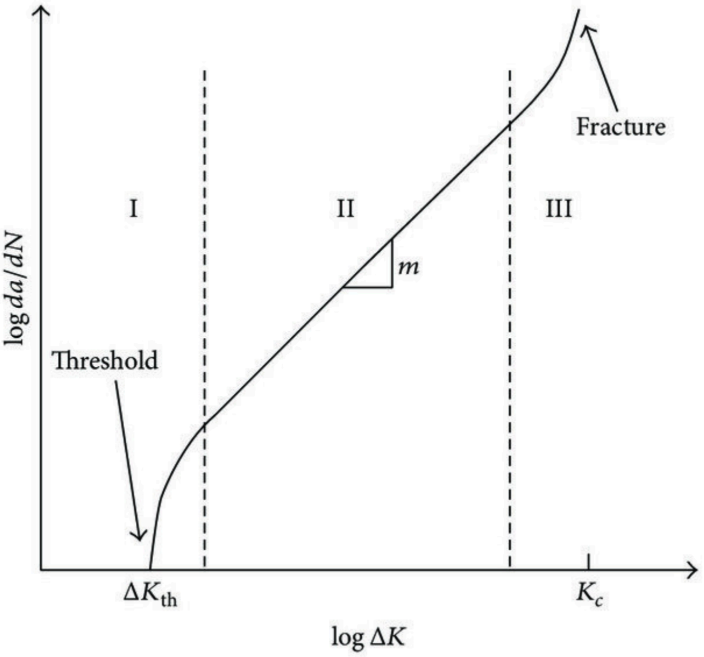

Figure 2.11: Typical fatigue crack growth behavior in metals [12]

Region I: Near-threshold region

The first region describes the early development of a fatigue crack at low values of da/dN and ΔK. An interesting value is indicated on the bottom left, namely the threshold value ΔK_{th}. Where da/dN approaches zero, the crack will not grow. However, above this threshold value, cracks begin to propagate. The fatigue threshold value depends on several parameters, such as the frequency of loading and environmental conditions.

Region II: Paris region, crack propagation

The largest part of fatigue crack growth rate behavior is described by a linear trend in region II. In this region, the crack growth behavior can be described by a power law, commonly referred to as the Paris law [65]:

$$\frac{da}{dN} = C\Delta K^m \tag{2.6}$$

The values for the material constants C and m are determined experimentally.

Region III: High crack growth rates near failure

Crack growth in the third region is rapid and unstable, until failure occurs. The accelerating crack growth can be identified by the upper tail in the high ΔK region. Region III is characterised by K_{max} approaching K_c, which is the fracture toughness of the material. Usually, this region is ignored for fatigue life predicitions as it does not affect the total crack propagation life.

2.4.2. Fatigue crack growth in hydrogen environments

In 1973, Wei and Simmons studied the environment enhanced fatigue crack growth in high-strength steels. [13]. They proposed three general patterns of the effects of hydrogen on the fatigue behavior, see Figure 2.12. The seperate figures show the behavior in both inert and hydrogen environments. The characteristics of the three types will be briefly discussed.

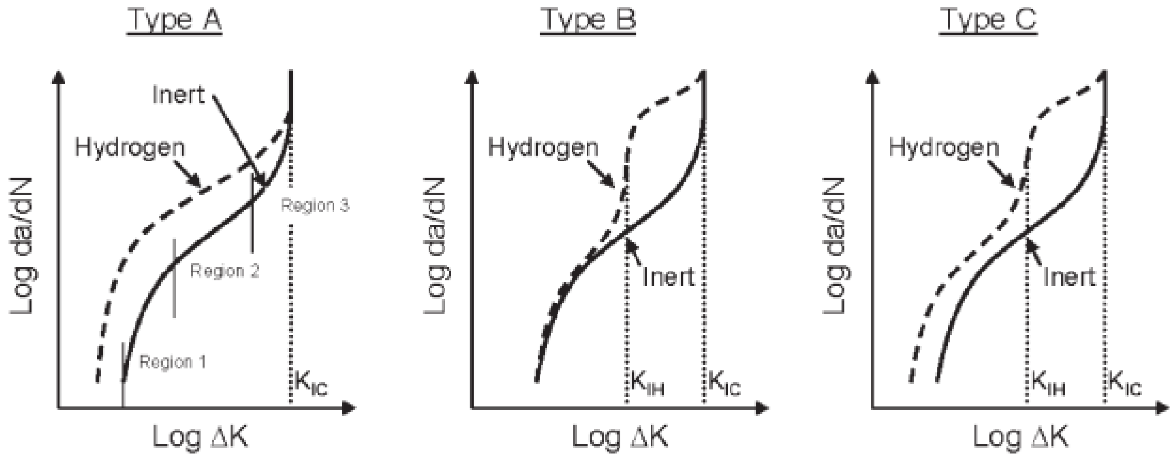

Figure 2.12: Possible effects of hydrogen on fatigue cracking behavior [13]

As can be seen on the most left of Figure 2.12, the stress intensity factor necessary to start the crack growth process is significantly lower in the presence of hydrogen for Type A behavior. Secondly, an important characteristic is that the crack growth rate is increased at given K levels.

Considering Type B behavior, the response in both inert and hydrogen environments is approximately the same up until the threshold value of K_{IH}. The crack growth rate for a given value of K increases dramatically after this threshold.

Characteristic for Type C is that it actually represents combined behavior of Type A and Type B. Most materials show fatigue cracking behavior as presented on the most right in Figure 2.12. Type A behavior is noticed for levels below K_{IH} (see vertical dashed line), and Type B behavior above this threshold.

Nanninga et al. specifically pay attention to the effects of atomic hydrogen on the process of fatigue crack growth, which is called hydrogen-assisted fatigue crack growth (HA-FCG) [66]. Different testing variables, such as frequency, pressure and stress ratio, influence HA-FCG. From their experiments, it was observed that general pipeline steels experience significantly increased fatigue crack growth rates in high-pressure hydrogen environments. This is also mentioned in a more recent study by Ryan and Mehmanparast [67]. Additionally, the magnitude of HA-FCG depends on the concentration of hydrogen in steel, which is highly dependent on the hydrogen pressure.

To this day, describing fatigue behavior in a hydrogen environment remains a complex process. An additional challenge is the increase in demand for high strength steels due to economic and environmental reasons, as high strength steels are highly sensitive to hydrogen embrittlement [68] [69]. However, HA-FCG is not impacted by the strength of steel [70]. What is specifically interesting for this research, is the effect of strain rate on fatigue crack growth behavior.

2.5. Pipeline failure

What is essentialy relevant in the context of this research, is pipeline failure. A comparison study by Nanninga et al. addresses hydrogen embrittlement in three pipeline steels in high pressure gaseous hydrogen environments [14]. Specimens taken from pipe sections of API-5L steel grades X52, X64 and X100 were compared with the results obtained from tests in air at normal temperature and pressure. The behavior in different environments for different steel grades can easily be observed from Figure 2.13. The tensile response is clearly different in hydrogen compared to air. For all three steel grades, a significant shift to the left can be noticed, which indicates a smaller strain at failure. In general, the presence of hydrogen causes the fatigue crack to propagate faster. This higher crack growth rate also affects the ductility of the material, hence the material will fail quicker.

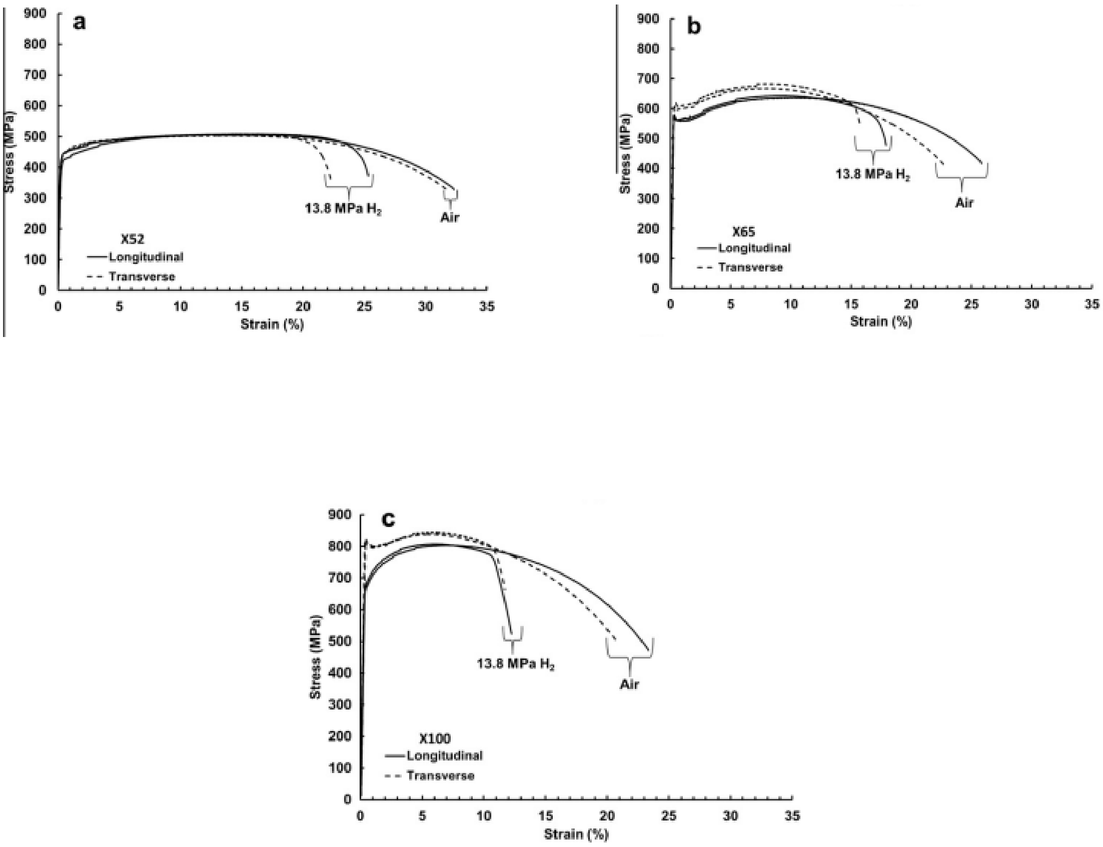

Figure 2.13: Tensile curves of different steel grades tested in air and hydrogen: a) X52, b) X65, c) X100 [14]

In Figure 2.14, different tensile curves for a X100 steel specimen tested in hydrogen are shown. From this figure, a relationship between increasing pressure and decreasing tensile ductility can be observed. Additionally to testing at varying gas pressures, Nanninga et al. also studied the effect of strain rate on tensile behavior. The curves for experiments at different strain rates in air and hydrogen can be seen in Figure 2.15. A loss in ductility can again be observed when testing in hydrogen. Although the shape of the curves in Figure 2.15 is very similar to those in Figure 2.14, no such relationship as obtained for hydrogen at different gas pressures could be retrieved.

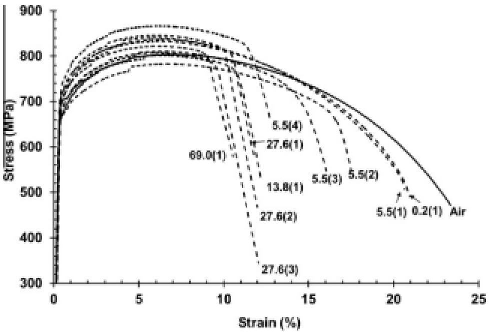

Figure 2.14: Tensile curves of a X100 specimen tested in hydrogen at different gas pressures. [14]

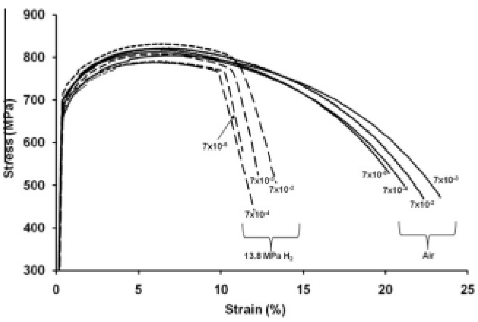

Figure 2.15: Tensile curves of a X100 specimen tested in hydrogen and air at different strain rates [14]

2.5.1. Crack tip plasticity

Figure 2.16 shows the relative dimensions to take into account for the applicability of linear elastic fracture mechanics. The image on the left shows the dimensions of the plastic zone compared to the crack length, in which the crack length is indicated with a, the remainder of the uncracked material with b and the region of plasticity surrounding the crack tip with r_y. If r_y is small compared to a and b, linear elastic fracture mechanics can not be applied [15]. A notch is shown on the right in Figure 2.16. If the notch root radius ρ is of the same order of size or larger than the crack length, linear elastic fracture mechanics can not be used.

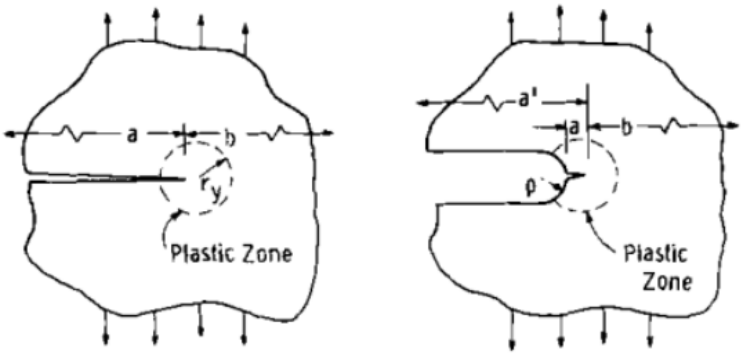

Figure 2.16: Relative dimensions for the applicability of linear elastic fracture mechanics [15]

2.6. Conclusions and research objectives

After discussing the literature relevant to the topic of anchor dragging of hydrogen pipelines, conclusions can be drawn from the review. From the current literature review it became evident that there exists a research gap in HA-FCG behaviour for pre-strained materials. A main research objective can be formulated through the conclusions and research gaps.

2.6.1. Conclusions

This literature review focused on reviewing relevant and state-of-the-art findings on pipelines affected by plastic strain and the change in mechanical properties in the presence of hydrogen. The following key findings can be formulated:

- After impact and corrosion, ship anchoring is the most occuring cause for accidental breakdown. There are several known causes of anchors damaging oil and gas pipelines.
- As the demand for hydrogen is growing, the anchor hooking problem has to be revised for steel pipelines carying hydrogen.
- As the pipeline is dragged across the seadbed and snaps back to its initial position, plastic strain is developed, which attracts hydrogen.

- At high strain rates, there is not enough time for hydrogen to accumulate at the grain boundaries.
- The crack growth rate, which is dependent on the rate at which hydrogen can penetrate into the metal, is affected by the degree of plasticity.

2.6.2. Research objectives

Extensively studying the current literature showed that there exists a research gap in HA-FCG behaviour for offshore pipelines damaged by a hooked anchor. The questions that arise are whether a hydrogen pipeline would get damaged more easily during the dragging event and if the pipeline would continue to survive the operational static and dynamic loads even with the large strain incurred.

To answer this rather broad question, the research objectives for this master's thesis can be summarized as follows:

- What is the resulting stress distribution and variation within the pipeline material after anchor impact?
- How is the rate of fatigue crack growth in an anchor hooking problem affected in the presence of hydrogen?
- When does the crack reach a critical depth, possibly leading to pipeline failure?

3

Methodology

This chapter applies the fundamental concepts and theories discussed in the existing literature to the methodology used in this thesis. This thesis aims to evaluate the main research question by determining how anchor hooking affects the post-incident life in a pipeline in the presence of hydrogen. The scope of the research is divided into two main components: numerical simulations and a fatigue crack growth model.

The numerical simulations focus on analysing the interactions between the anchor and the pipeline. The fatigue crack growth model allows for the estimation of the remaining useful life of the pipeline by determining the number of cycles until failure. Additionally, the application of a Failure Assessment Diagram (FAD) assists in determining the maximum allowable crack size that ensures the structural integrity and safety of the pipeline.

3.1. Numerical simulations

The numerical approach in ANSYS 2022 R2 simulates the interaction between an anchor and a hydrogen pipeline during the process of hooking and dragging, and assesses the impact of a dragging anchor on a pipeline. To simulate the behaviour of the anchor and pipeline, a three-dimensional (3D) model is constructed using the ANSYS software. This approach enables the understanding of the stress variation within the pipeline and provides insights into the behaviour of both the anchor and the pipeline. This study simulates a recent anchor dragging incident, in which an 8-inch pipeline was hooked and damaged by an AC-14 High Holding Power (HHP) anchor. While the incident under investigation involved a buried pipeline, this thesis does not consider the influence of the surrounding soil in order to simplify the scope of the thesis. However, as 8-inch pipelines are typically buried, the presence of soil is acknowledged. The pipeline is fixed at a distance of 20 m from the anchor, representing the exposed section after the incident.

3.2. Fatigue crack growth model

The second phase in determining the post-hooking lifetime is the development of a model in Matlab to characterise the crack growth curve, which represents the relationship between the crack length (a) and the number of cycles (N) required for the crack to propagate under cyclic loading conditions. This model primarily relies on the Paris-Erdogan law, which establishes a relationship between the rate of crack propagation in a material and the stress intensity range. To determine the number of cycles until failure, the maximum allowable crack size should be defined. In parallel with the fatigue assessment, a fracture assessment is conducted to establish the maximum allowable crack size. The maximum allowable crack size is determined through the use of a FAD, which provides a criterion for defining the maximum acceptable crack size in the material. The result obtained from the FAD serves as a critical criterion in the subsequent fatigue assessment for assessing the number of cycles until failure.

3.3. Flowchart: exchange of information

This section explains the flowchart in Figure 3.1, which provides a high-level understanding of the information transfer within the processes described in Section 3.1 and Section 3.2, highlighting the main steps involved. This flowchart helps to better understand the different relevant factors influencing the number of cyles until failure. Figure 3.1 visually represents the exchange of information between the numerical simulations, fatigue crack growth model, and the simultaneous process of establishing the FAD. This visual representation enhances the understanding of the interaction between these models and the critical aspects involved in the assessment of fatigue crack growth and failure.

Within the overall framework of the analysis, there are three distinct streams of information: results from the numerical model in ANSYS, a fatigue crack growth model in Matlab, and a fracture assessment using the FAD. These streams represent different aspects of the analysis process and collectively contribute to a comprehensive understanding of the system's behaviour.

The process begins by conducting a numerical simulation using ANSYS software to model the interaction between an anchor and a pipeline. The analysis of the stress distribution takes into account factors such as the maximum pressure exerted on the pipeline and the pressure variations resulting from daily and yearly changes. By considering these pressures, the calculation of membrane and bending stresses is performed at the specific location along the pipeline where the highest von-Mises stress is observed. These stress calculations provide important information for the subsequent analysis and assessment of the anchor-pipeline system.

Next, a fatigue crack growth model in Matlab is utilised to evaluate how cracks in the pipeline grow under cyclic loading. The crack size is continuously evaluated until it reaches the maximum allowable crack size. The stress calculations from the ANSYS simulation are used to determine the stress intensity range. A crack growth curve is plotted, showing the relationship between crack size and the number of cycles, enabling the determination of the number of cycles until failure. Simultaneously, a FAD is used to establish the maximum allowable crack size for the fatigue assessment. An assessment line is defined on the diagram, as well as a cut-off value. The ANSYS simulation provides the maximum reference stress, corresponding to the maximum stress experienced by the pipeline. Subsequently, the maximum stress intensity factor is solved to find the maximum allowable crack size.

Although the flowchart identifies the key points of information exchange, a more specific desription of the sources that provide the input data is required to conduct a more focused analysis. Each process can be further elaborated and presented in more detail through successive steps within the respective flowcharts. Additional information and detailed flowcharts regarding the numerical simulations and the fatigue crack growth model can be found in Chapter 4 and Chapter 5, respectively, which specifically address these aspects.

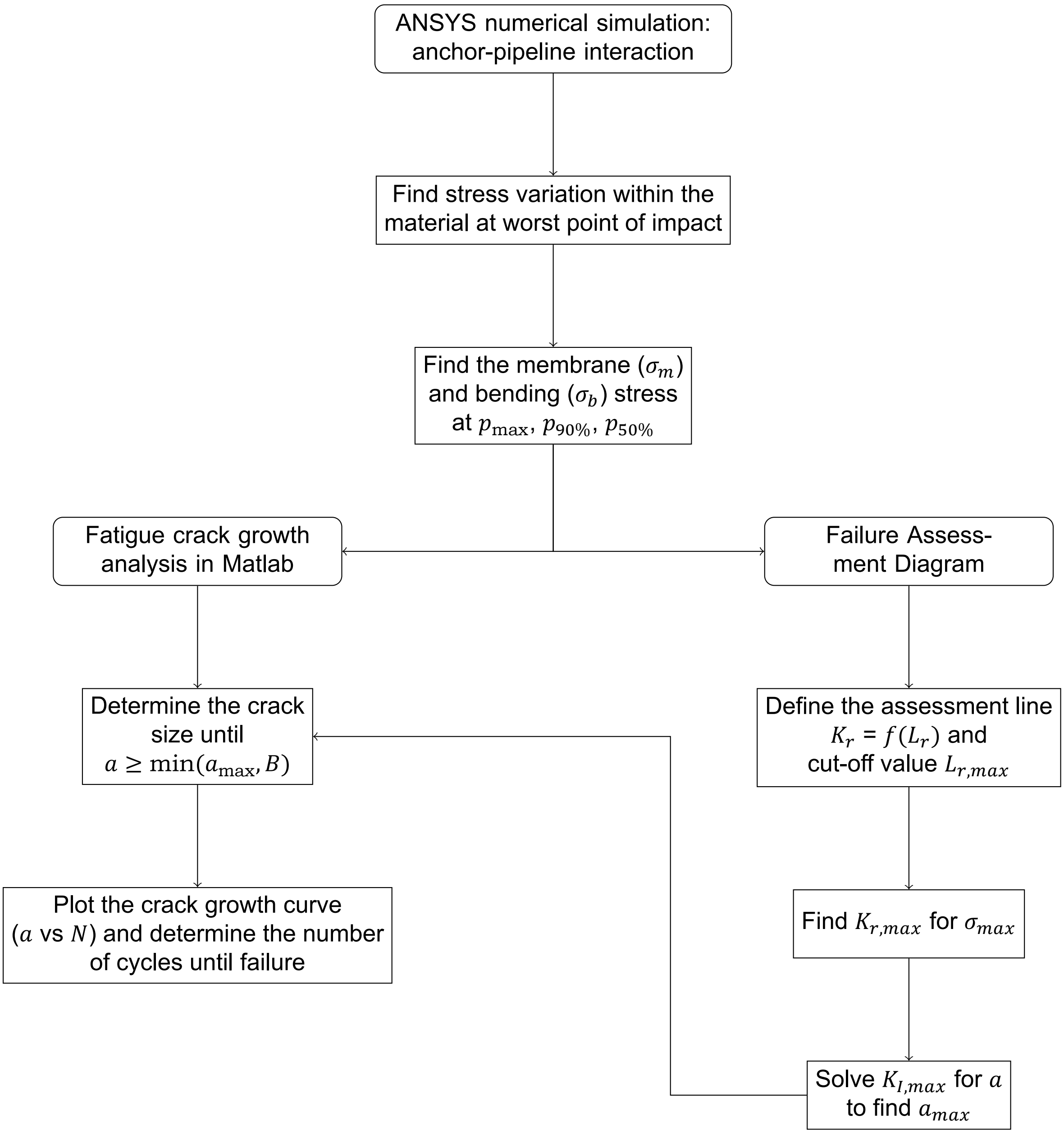
ANSYS numerical simulation: anchor-pipeline interaction
Find stress variation within the material at worst point of impact
Find the membrane (σ_m) and bending (σ_b) stress at $p_{\max}$, $p_{90\%}$, $p_{50\%}$
Fatigue crack growth analysis in Matlab
Failure Assessment Diagram
Determine the crack size until $a \geq \min(a_{\max}, B)$
Define the assessment line $K_r = f(L_r)$ and cut-off value $L_{r,max}$
Plot the crack growth curve (a vs N) and determine the number of cycles until failure
Find $K_{r,max}$ for σ_{max}
Solve $K_{I,max}$ for a to find a_{max}

Figure 3.1: Overview of methodology flowchart

4

Numerical simulations

After explaining the fundamentals of anchor dragging and its impact on pipelines, it is necessary to expand upon these principles by exploring more complex loading conditions to replicate real-world scenarios as closely as possible. To better comprehend and analyse pipeline behaviour under varying loading conditions, a model is created using ANSYS Finite Element Method (FEM) software. Using this software will allow for a better understanding of the response of pipelines to different loading conditions, thus providing more accurate predictions in practical applications.

The presented flowchart in Figure 3.1 provides a concise overview of the key stages involved in the simulation aimed at assessing anchor hooking incidents on hydrogen pipelines. It outlines the essential simulation outputs required as inputs for the subsequent fatigue crack growth model and fracture assessment. However, for a more comprehensive understanding of the underlying procedures, the flowchart in Figure 4.1 offers a more detailed overview of numerical simulation set-up.

This chapter focuses on the establishment of the model, providing a detailed description of the anchor and pipeline designs. Important design decisions involve determining the contact behaviour, which describes the physical interaction between the anchor and the pipeline, as well as establishing the length of the pipeline. Section 4.1 explains the various components and design decisions involved in setting up the ANSYS model for simulating the anchor-pipeline interaction. A detailed table containing the parameters and corresponding values can be found in Appendix A. Lastly, boundary conditions are needed to ensure the model functions correctly. Section 4.2 will discuss the boundary conditions in conjunction with the applied analysis settings.

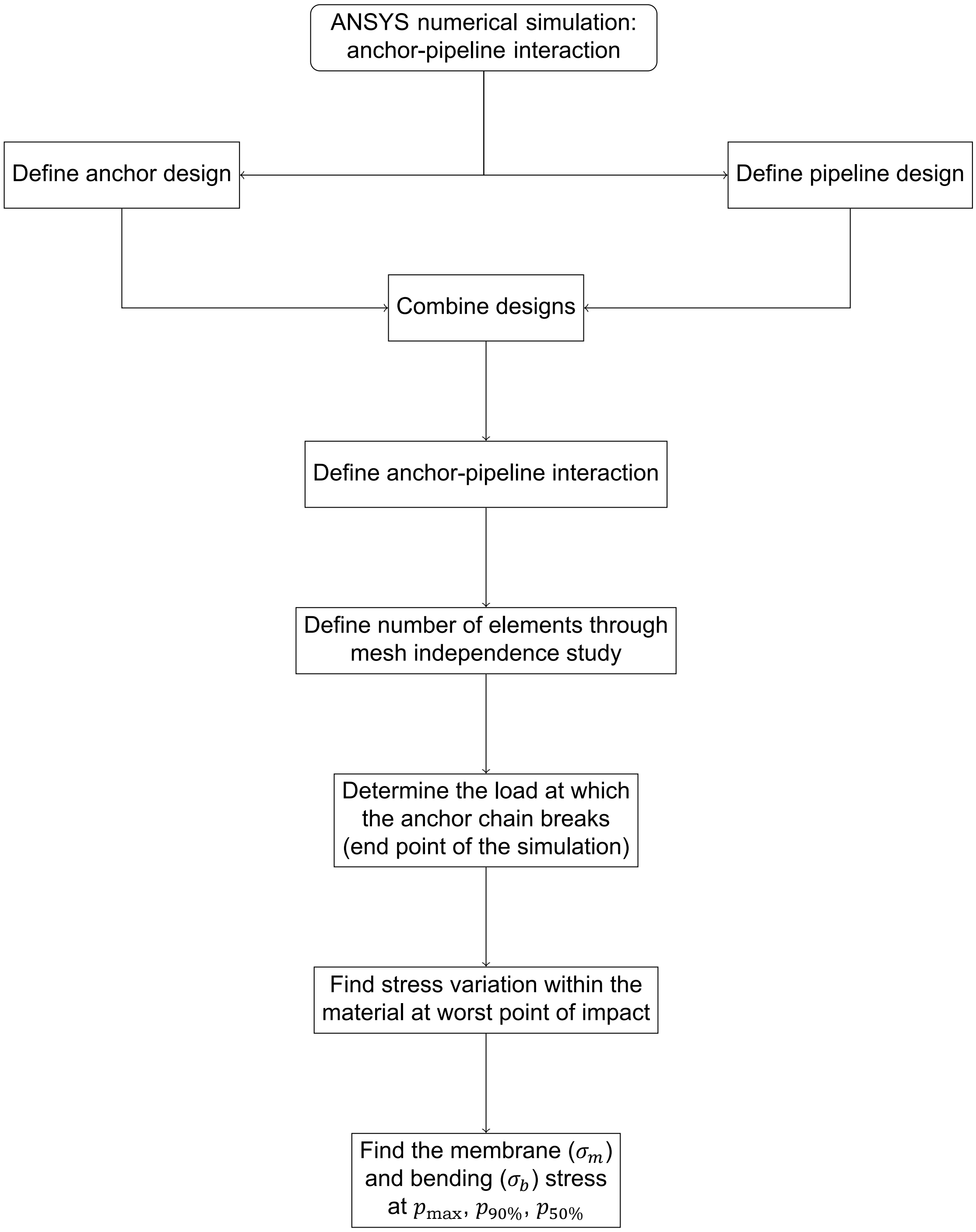
ANSYS numerical simulation: anchor-pipeline interaction
Define anchor design
Define pipeline design
Combine designs
Define anchor-pipeline interaction
Define number of elements through mesh independence study
Determine the load at which the anchor chain breaks (end point of the simulation)
Find stress variation within the material at worst point of impact
Find the membrane (σ_m) and bending (σ_b) stress at $p_{\max}$, $p_{90\%}$, $p_{50\%}$

Figure 4.1: Flowchart of the numerical simulation for evaluating anchor hooking incidents on hydrogen pipelines.

4.1. Model set-up

This section explains the various components and design decisions involved in setting up the ANSYS model for simulating the anchor-pipeline interaction. As accurate simulation results rely heavily on the correctness of the decisions and parameters set in the model, an overview of the different components involved in the simulation is provided, along with the reasoning behind the design decisions made.

4.1.1. Anchor and pipeline design

The initial stage of establishing a full working model for simulating the behaviour of a pipeline during dragging involves the design of the anchor and pipeline. This step is crucial as it forms the foundation for the subsequent stages of the modelling process.

A complete SOLIDWORKS model of an AC-14 HHP anchor has been made available online by Babalola Sunday [20]. The SOLIDWORKS model is converted to a SpaceClaim model, as this is the preferred 3D modelling format in ANSYS Workbench for this research. Since a complete model of the anchor was already available, the subsequent task involves generating a pipeline using SpaceClaim and integrating both models. The pipeline model in SpaceClaim is based on the information provided on the 8-inch pipeline, including dimensions, material properties, and operating conditions. Once the pipeline model is created, it needs to be accurately positioned and orientated in relation to the anchor model. The coordinate system is located at the center of the pipeline. More specifically, the x-axis is orientated along the longitudinal direction of the pipeline, while the y-axis follows the direction of movement towards the pipeline as dictated by the flukes of the anchor. Additionally, the z-axis is orientated upward from the seabed. By locating the coordinate system in this way, it is ensured that the simulation accurately represents the real-world conditions of the system being modelled.

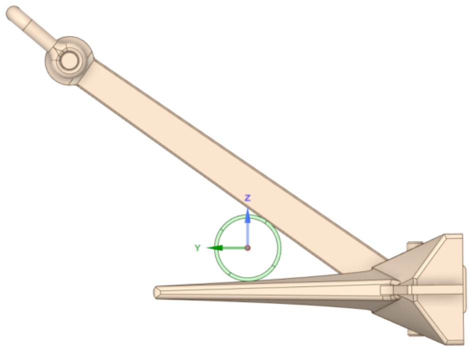

Figure 4.2: YZ plane for anchor-pipe configuration.

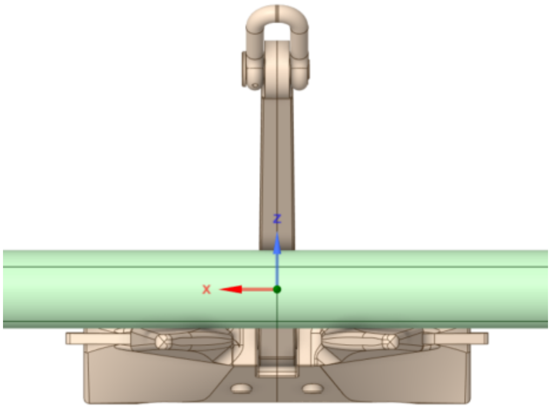

Figure 4.3: XZ plane for anchor-pipe configuration.

In Figure 4.2 and Figure 4.3 it is shown that the pipeline and anchor components are in contact. To accurately capture the physical interaction between these components in the model, it is essential to define the contact behaviour. In this case, the contact between the pipeline and the upper part of the anchor (shank) as well as the lower part of the anchor (fluke) is considered as frictional contact. This choice of contact type is appropriate for the simulation as it involves sliding between the contacting surfaces. The friction coefficient is defined as 0.1

The pipeline in the ANSYS model is assembled out of two sections. A smaller, solid pipeline section is used to demonstrate the local effects of the anchor-pipeline interaction. For the remaining part of the pipeline, a slightly different approach is taken compared to the previous one. A significantly longer beam element with a cross-sectional profile that matches the shape of the pipeline is created. This approach allows for more accurate modelling of local deformations while reducing the computational requirements. Figure 4.4 depicts both the solid pipeline, identifiable by its partition into different sections as needed during the meshing process, and the elongated beam element.

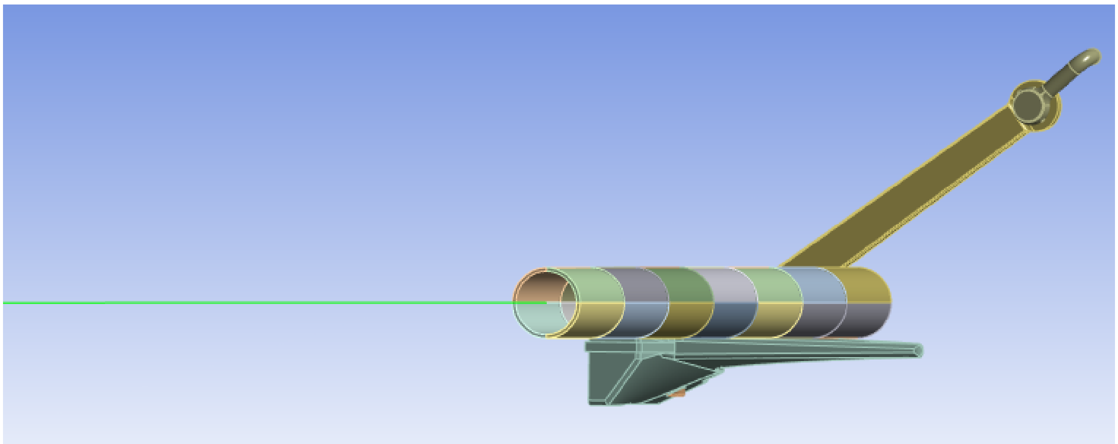

Figure 4.4: Contact between anchor and solid pipeline with beam element.

The solid pipeline and the beam element have different lengths due to the specific considerations of the incident. The length of the solid pipeline corresponds to the damaged area, which covers a distance of 7 m. This segment accurately captures the local behaviour resulting from the anchor impact. On the other hand, a significantly larger beam element is necessary to account for the development of far-field membrane tension. According to the survey report, a pipeline section of approximately 120 m was dredged with the anchor location as the center point. However, it is important to note that this section does not accurately represent the exposed portion during the dragging incident and the pipeline's condition after the incident. It is assumed that approximately 40 m of the pipeline section was exposed during the dragging incident, with the anchor location as the center point, while the rest of the pipeline remained buried. Due to the implementation of symmetry boundary conditions, the model is divided in half at the center of the anchor. As a result, only half of the anchor and half of the pipeline are considered in the analysis. By applying the symmetry boundary condition, only half of the previously mentioned length of 40 m is taken into consideration in the model. This means that the solid pipe considers a section of 3.5 m, while the beam element has a length of 16.5 m. The application of symmetry boundary conditions is discussed in Section 4.2.2.

4.1.2. Meshing

The meshing process in the model involves three distinct steps, corresponding to defining the meshing on the anchor and two sections of the pipeline. First, the meshing on the anchor is specified. Since the anchor is considered to behave as a rigid body, the quality of the mesh becomes less critical compared to deformable bodies. Rigid bodies do not experience internal deformation or strain, and are assumed to maintain their shape and size under applied loads. In this case, an automatic method using quadrilateral elements is selected to define the meshing for the anchor. The mesh is applied to the specific areas of the anchor that come into contact with the pipeline, namely the shank and the fluke. Figure 4.5 provides a visual representation of this meshing configuration.

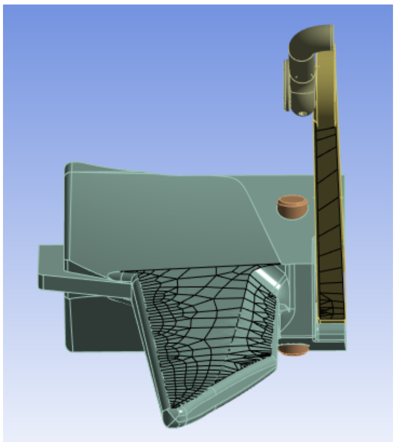

Figure 4.5: Quadrilateral dominant meshing on the shank and fluke in ANSYS.

The set-up for the meshing is defined in three directions, namely radial, hoop, and longitudinal. This makes it possible to specify the number of elements in each direction. This analysis uses 3D 20-node, solid elements, defined as SOLID186 in ANSYS, in the meshing process. A mesh independence study is conducted to determine the appropriate number of elements in each direction. The details of this study can be found in Section 6.1.2, and the present section presents the final results obtained. For the 8-inch pipeline considered in this study, 3 elements are defined through thickness. Figure 4.6 illustrates a small section of the pipeline, offering a clear depiction of the distributed elements throughout its thickness. The figure also shows the distribution of elements in the hoop direction. The pipeline is divided into four separate sections, with a defined number of divisions in the hoop direction for each section. Specifically, 10 divisions are defined per section, resulting in a total of 40 elements in the hoop direction for the entire cross section. The right side of the pipeline highlights the presence of these elements.

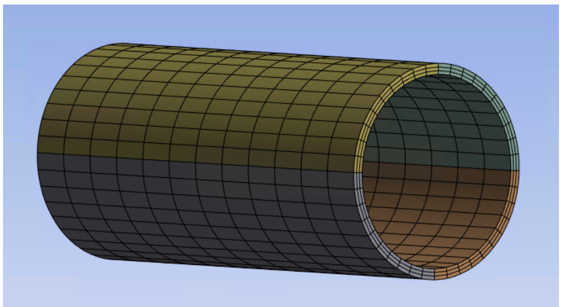

Figure 4.6: 3D 20-node, solid elements are used to specify the mesh in the radial, hoop, and longitudinal direction.

Finally, the longitudinal direction of the solid pipeline is considered for element specification. The pipeline is divided into multiple sections longitudinally, allowing for a more detailed mesh near the impact point. The 3.5 m solid pipeline is partitioned into 7 sections, each with a length of 0.5 m. To capture local behaviour, a more detailed mesh is applied to the two sections closest to the contact point of the anchor on the pipeline. Specifically, in the vicinity of the impact point, 12 elements are defined in the longitudinal direction. The remaining sections consist of 3 elements per section in the longitudinal direction. Figure 4.7 shows the differences in mesh sizing in the longitudinal direction.

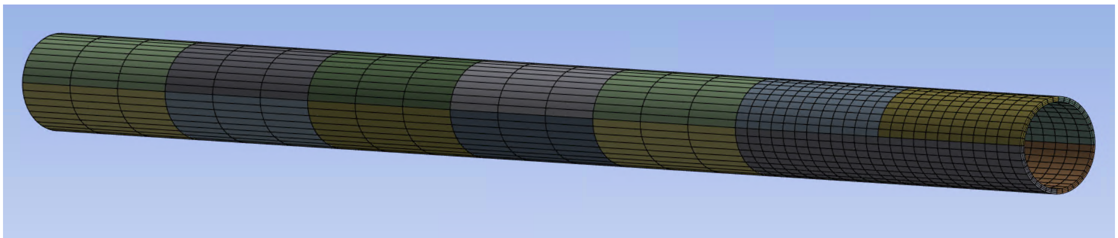

Figure 4.7: 3 elements in the longitudinal direction are defined per pipeline section. 12 elements are defined near the impact point.

The mesh divisions of the solid pipeline are determined based on a prescribed number of divisions in each direction, while the meshing of the beam element follows a different approach. Throughout the entire length of 16.5 m, elements with a length of 0.5 m are used, conforming to the assumption of using a minimum of five times the diameter, which is a typical practice.

4.1.3. Anchor and pipeline parameters

To accurately simulate the behaviour and interaction of a pipeline and anchor, the relevant parameters based on the design requirements and specifications need to be defined. It is necessary to input data such as geometric dimensions and material properties into the ANSYS finite element analysis to complete the establishment of a fully working model. The engineering data for the anchor has already been defined by Babalola Sunday in his SOLIDWORKS model [20]. Table A.3 presents the same parameters along with their respective values and units. The 8-inch pipeline taken into consideration has material grade L360NB, which is the API 5L X52 equivalent. The relevant dimensions and material properties for the pipeline are presented in Table A.2.

4.2. Analysis settings and boundary conditions

Boundary conditions are a critical aspect of finite element analysis in ANSYS. They define the conditions that a structure or component experiences at its boundaries, which in turn affects its behaviour and response to external loads. This section explores the different types of analysis settings and boundary conditions available in ANSYS and how these are applied in this analysis.

4.2.1. Analysis settings

The ANSYS version number that is used to make the model is ANSYS 2022 R2. The Transient Structural solver is used to execute the hooking incident. ANSYS Transient Structural analyses time-dependent or dynamic structural problems. The simulations in ANSYS consists of three distinct steps, representing the initial pressurisation of the pipeline, the hooking incident, and the stress-pressure relationship afterwards. The first and the third step are static processes, and when time integration is turned off in the Transient Structural solver, the analysis becomes a static analysis. During the second step, time intergration is turned on, as the dynamic interaction between the pipeline and the anchor is likely to exhibit time-dependent behaviour. This is because the pipeline's response and deformation will depend on factors such as the applied forces, the movement of the anchor, and the material properties of the pipeline. During the dragging process, the forces and displacements acting on the pipeline will vary with time as the anchor moves.

The "Analysis Settings" defined in ANSYS specify the step controls. In the first step, the pipeline is statically pressurised and time integration is disabled. During a period of 1 s, the pipeline is pressurised with gauge pressure to establish equilibrium without the anchor impact. The simulation easily converges during this step. The initial and minimum time steps are set to 0.1 s, while the maximum time step is set to 0.5 s. The anchor impact is then applied in the second step, which causes the anchor and pipeline to move. This step considers the motion over time, and time integration is enabled. The duration of this step is determind based on the maximum force the anchor chain can experience before it breaks. This will be further explained in Section 4.2.3. Smaller time steps are necessary for the model to converge. The initial and minimum time steps are set to 1e-4 s, while the maximum time step is set to 1e-2 s. The third time step considers the simulation after impact, and the stress-pressure relationships are determined. The pipeline is statically pressurised again, either at p_{max}, $p_{50\%}$, or $p_{90\%}$. Once again, time integration is turned off during this step. The initial and minimum time steps are set to 0.1 s, while the maximum time step is set to 0.5 s.

4.2.2. Initial and boundary conditions

This section provides an overview of the initial and boundary conditions used in this model, along with the implementation of the displacement of the anchor-pipeline system. The initial condition applied to the system is the pressure inside the pipeline. The boundary conditions define the behaviour at the end of the pipeline and the symmetry plane used in the analysis.

The pipeline is subjected to internal pressurisation using gauge pressure, which is determined by the difference between the internal pressure and the external pressure. The internal pressure, or design pressure, for an 8-inch hydrogen pipeline is typically 4000 kPa or 40 bar [71]. The external pressure at the seabed is calculated by adding the atmospheric pressure and the hydrostatic pressure. The standard atmospheric pressure is measured as 101 kPa. At a depth of 36.5 m, the hydrostatic pressure is estimated to be around 367 kPa. By substracting the external pressure from the internal pressure, the pipeline in the model is internally pressurised at a gauge pressure of 3532 kPa. During the analysis, the pipeline is pressurised in the first step, before the system is subjected to movement in the second step.

Next, the displacement of the anchor is taken into consideration. The process of anchor hooking is considered to represent this displacement, where the anchor is released from the ship and drags along the seabed until it hooks onto the pipeline. The ship continues to move forward, but the interaction between the hooked anchor and the pipeline generates resistance, resulting in a gradual deceleration of the ship's speed. It is important to note that the focus of the analysis is on the displacement rather than the velocity, as the initial anchor-pipeline impact is not explicitly taken into consideration. The simulation under consideration does not account for the impact resulting from the velocity of the anchor on the pipeline. This is primarily due to the presence of initial contact between the anchor and the pipeline before the simulation starts. As a result, the velocity of the anchor becomes less relevant in this context. Instead, the focus is on defining the displacement of the anchor as it interacts with the pipeline. In the simulation, the anchor is displaced from its original position by 2.5 meters over 9 seconds, resulting in the dragging of the pipeline along with it.

A remote point is created to apply the above defined displacement to the model. Remote points in ANSYS offer a convenient way to apply loads or constraints at specific locations that are not directly associated with nodes or elements of the model. The displacement of the anchor is assigned to the remote point located at the shackel pin, which is located at the top of the shank. Similar to the anchor's overall rigid behaviour, the behaviour at this remote point is also considered rigid. Rigid behaviour of a remote point assumes that the deformations and rotations within the vicinity of the remote point are negligible compared to the overall behaviour of the system. Figure 4.8 displays the remote points that are established within the model, including the remote point located at the shackel pin. This particular remote point is associated with the application of the displacement, indicated by 'A' in Figure 4.8. Additionally, there are other remote points where boundary conditions are applied, which will be elaborated on hereafter.

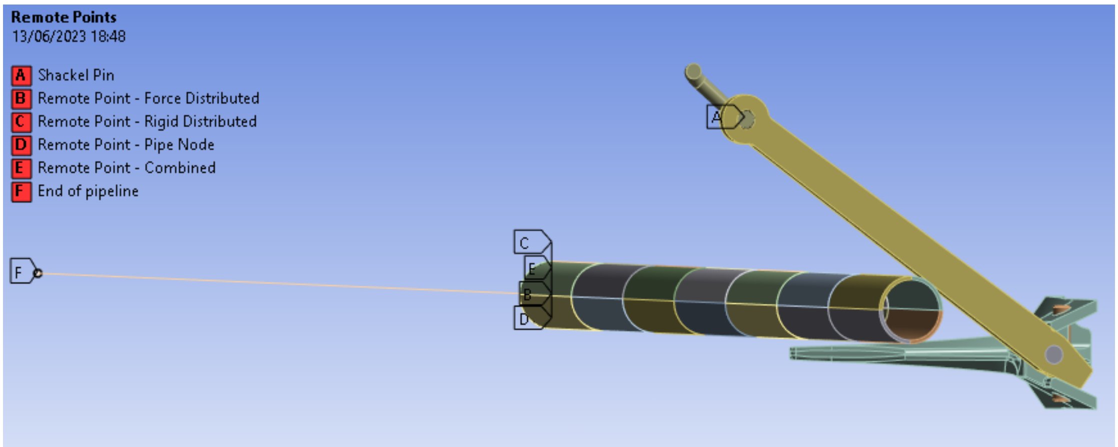
Remote Points
13/06/2023 18:48
A Shackel Pin
B Remote Point - Force Distributed
C Remote Point - Rigid Distributed
D Remote Point - Pipe Node
E Remote Point - Combined
F End of pipeline
A
C
E
B
D
F

Figure 4.8: Remote points corresponding to the fixed boundary condition, MPC connection, and displacement of the model (from left to right).

The boundary conditions in the analysis are essential for determining the behaviour of the pipeline at its ends and at the impact point. In the numerical simulations conducted in ANSYS, the fixed boundary condition is applied to the end of the pipeline section. This condition restricts the movement and rotation of the pipeline in the x, y, and z directions. By fixing the pipeline at the end section, it prevents unrestricted motion, ensuring that the pipeline remains in place and does not continue to move endlessly. The fixed boundary condition is applied to the end of the beam element, indicated by 'F' in Figure 4.8. The pipeline (solid pipe and beam element) is fixed at a distance of 20 m, with the anchor location as the center point. This assumption implies that the fixed condition at this distance accounts for the exposed part of the pipeline, while the remaining pipeline sections are still buried.

The last set of remote points, denoted as 'E' in Figure 4.8, serves as the link between the solid pipeline and the beam element. The motion of nodes of the solid pipeline, referred to as the contact surface, can be effectively linked to a pilot node on the beam element, referred to as the target surface, using a surface-based constraint. This constraint allows for the coupling of displacements between the contact surface and the pilot node. By establishing this connection, the behaviour of the contact surface can be accurately represented in relation to the motion of the pilot node on the target surface. The connection between the solid pipeline and beam element is achieved using the Multi Point Constraint (MPC) formulation. Multiple remote points with different characteristics are required to establish the MPC connection between the two elements. Figure 4.9 shows what this MPC connection between the solid pipeline and beam element looks like.

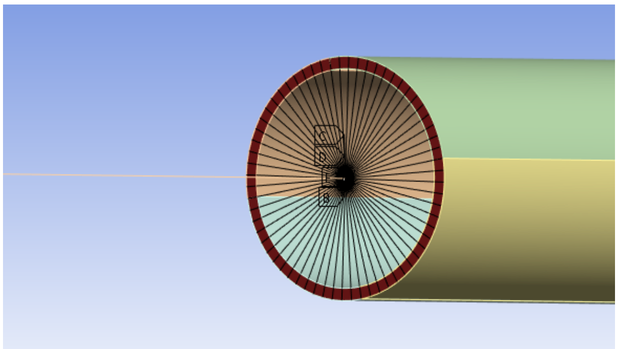

Figure 4.9: MPC connection between the beam element and solid pipeline.

The first remote point, associated with the node on the beam element in the plane of the end of the solid pipeline, represents a reference point on the pipeline. It serves as a connection point for the MPC formulation and helps establish the relationship between the beam element and solid pipeline. The second remote point defines a force-distributed constraint. This constraint corresponds to the face of the pipeline exhibiting deformable behaviour. This remote point represents a location on the pipeline's surface where deformations and movements occur during the analysis.The third remote point in the set corresponds to the rigid surface constraint. By applying the rigid surface constraint, the displacements and rotations of the contact nodes on the solid pipeline are constrained to match those of the pilot node on the beam element. Combining these three remote points into a single remote point in the MPC formulation ensures that the behaviours and constraints associated with each remote point are collectively considered at the combined remote point. This allows for the coupling and interaction between the beam element and the solid pipeline, enabling an accurate representation of their interconnected behaviour.

The final boundary condition describes the behaviour at the impact point. Symmetry boundary conditions are used in ANSYS to simulate the presence of a symmetry plane in a model. A symmetry plane is a plane of symmetry that divides the model into two halves that are mirror images of each other. Symmetry boundary conditions are applied to the faces of the model that lie on the symmetry plane. A symmetry boundary condition assumes that the displacement, stress, and strain fields on one side of the symmetry plane are identical to those on the other side. Symmetry conditions are often used in ANSYS to simplify the analysis and reduce computational effort when studying symmetric structures. Figure 4.8 shows what half of the anchor and pipeline model looks like in ANSYS. The symmetry planes are defined at the shank and the faces on the right side of the pipeline shown in this figure.

4.2.3. End of the simulation

In order to obtain meaningful results, it is necessary to establish a termination point for the simulation. Therefore, one of the anchor-pipeline interaction scenarios discussed in Section 2.1 is analysed. In the case study of the Transmediterranean Pipeline Systems described in Section 2.1.2, an anchor hooking incident occurred where two pipelines were damaged by the anchor of a ship. Subsequently, the anchor chain broke, leaving the anchor trapped beneath the pipeline. In the specific case study considered in this thesis, the anchor was found in close proximity to the pipeline as well. The point at which the anchor chain breaks serves as a limiting condition, as it is assumed that the pipeline experiences external loads from the anchor until this point. Once the anchor chain breaks, the simulation is terminated, and the results can be obtained. Typically, when the anchor chain breaks, the applied load on the anchor is released, potentially causing the pipeline to snap back. However, this simulation does not account for the snap-back effect, which would result in the pipeline slightly moving back from its stretched position.

The minimum breaking load of chain cables is determined based on the guidelines provided by DNV-RU-INV [21]. According to these guidelines, the minimum breaking load (R) of a chain cable is calculated based on different ranges of anchor weight (P') . In the case of the AC-14 HHP anchor discussed in Section 4.1.1, which has an approximate weight of 2300 kg, the minimum breaking load is defined as follows for anchor weights exceeding 2000 kg:

$$R = 0.25 \cdot P' \tag{4.1}$$

By solving this equation for an anchor weight of 2300 kg, a minimum breaking load of 575 kN is obtained. The subsequent application of this minimum breaking load in the analysis will be elaborated upon in Section 6.1.1.

5

Fatigue crack growth model

Fatigue crack growth is a phenomenon that occurs in materials subjected to repeated loading and unloading cycles, ultimately leading to the propagation of cracks in the material. This type of crack growth is of significant concern in structural materials. Understanding the mechanics of fatigue crack growth and its behaviour is crucial for the design and maintenance of safe and reliable structures.

In the specific context of this study, which aims to investigate the post-hooking lifetime of hydrogen pipelines damaged by anchors, the flowchart presented in Figure 3.1 in Chapter 3 briefly outlined the key points of information exchange between the different models. The flowchart in Figure 5.1 offers a more detailed overview of the interconnected nature of the fatigue crack growth model and fracture assessment. The flowchart also highlights the main sources of input that contribute to these processes. The stress variation obtained from ANSYS simulations plays a crucial role in providing essential data for the evaluation of fatigue crack growth and potential failure. Both the fatigue and fracture streams depend on the results derived from ANSYS, emphasising their significance in the overall analysis and assessment.

First, this chapter discusses the concept of the fatigue crack growth curve, which describes the relationship between the crack growth rate, applied stress intensity factor and crack length. Next, Section 5.2 explains the model set-up used to simulate the fatigue crack growth behaviour of materials in the presence of hydrogen. A crucial aspect of this analysis is the stress distribution obtained from ANSYS simulations. The integration of the results derived from ANSYS into the fatigue and fracture assessment process is thoroughly explained. Continuing with this section, it initially focuses on the left segment of the flowchart illustrated in Figure 5.1, followed by an examination of the right segment. By following the flowchart and exploring the interconnected processes, this section provides a comprehensive understanding of the fatigue crack growth model and fracture assessment, highlighting the significance of integrating the stress distribution obtained from ANSYS simulations.

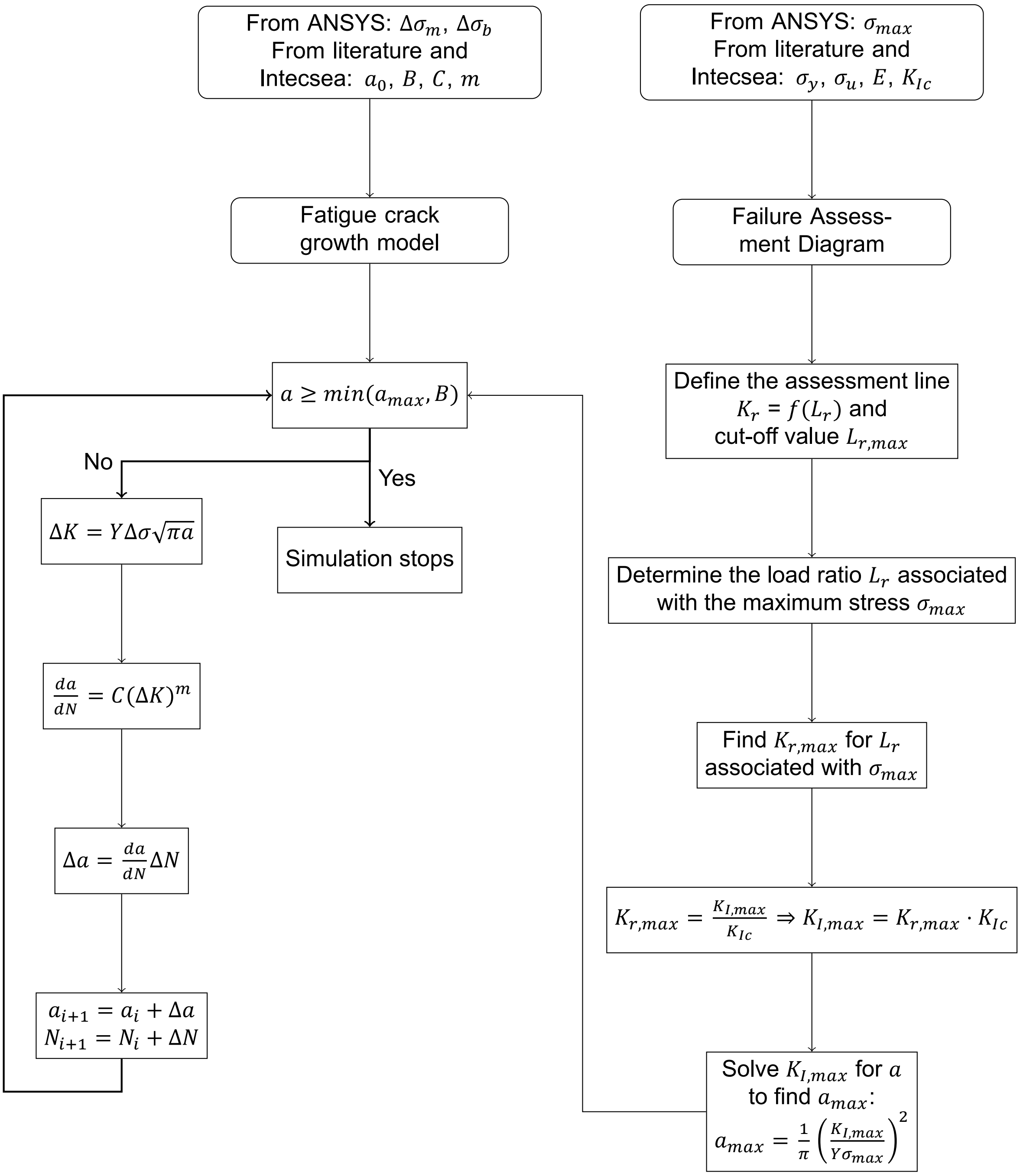
From ANSYS: $\Delta\sigma_m$, $\Delta\sigma_b$
From literature and Intecsea: a_0, B, C, m
Fatigue crack growth model
$a \geq min(a_{max}, B)$
No
Yes
$\Delta K = Y \Delta\sigma \sqrt{\pi a}$
Simulation stops
$\frac{da}{dN} = C(\Delta K)^m$
$\Delta a = \frac{da}{dN} \Delta N$
$a_{i+1} = a_i + \Delta a$
$N_{i+1} = N_i + \Delta N$
From ANSYS: σ_{max}
From literature and Intecsea: σ_y, σ_u, E, K_{Ic}
Failure Assessment Diagram
Define the assessment line $K_r = f(L_r)$ and cut-off value $L_{r,max}$
Determine the load ratio L_r associated with the maximum stress σ_{max}
Find $K_{r,max}$ for L_r associated with σ_{max}
$K_{r,max} = \frac{K_{I,max}}{K_{Ic}} \Rightarrow K_{I,max} = K_{r,max} \cdot K_{Ic}$
Solve $K_{I,max}$ for a to find a_{max}:
$a_{max} = \frac{1}{\pi} \left(\frac{K_{I,max}}{Y \sigma_{max}} \right)^2$

Figure 5.1: Simultaneous processes of the fatigue crack growth model (left) and fracture assessment (right).

5.1. Fatigue crack growth in a hydrogen environment

In Chapter 2.4, the basics of fatigue crack growth were discussed briefly, and the fatigue crack growth curve was introduced in Figure 2.11. This chapter specifically focuses on the parameters and equations that are relevant to fatigue crack growth in the presence of hydrogen. As hydrogen is known to have a significant impact on fatigue crack growth behaviour, it is important to study its effects and consider it in the development of a crack growth model. The different stages of the fatigue crack growth curve relevant to fatigue crack growth in a hydrogen environment are discussed in this section in more detail. Furthermore, this section also outlines the relevant material constants and equations that are necessary to model fatigue crack growth in the presence of hydrogen.

5.1.1. Regions on the fatigue crack growth curve: crack growth rate versus stress intensity range

Paris and Erdogan conducted several tests to study the rate of crack growth da/dN, and they found a correlation between the rate of crack growth and the stress intensity range ΔK [65]. The range is defined as the difference between the maximum and minimum stress intensity factor in a single load cycle, respectively K_{max} and K_{min}, and is dependent on the applied stress, crack depth, and geometry of the pipeline [64]. Specifically, σ_{max} represents the maximum value of applied stress and σ_{min} represents the minimum value of applied stress. The crack depth is indicated by a, and the factor Y corrects for the geometry of the pipeline, plasticity, bulging, welding, and loading. The following relationships are defined based on these definitions:

$$K_{max} = Y\sigma_{max}\sqrt{\pi a} \tag{5.1a}$$

$$K_{min} = Y\sigma_{min}\sqrt{\pi a} \tag{5.1b}$$

$$\Delta K = K_{max} - K_{min} = (Y\Delta\sigma)\sqrt{\pi a} \tag{5.1c}$$

Further experiments have revealed a distinct trend in all da/dN versus ΔK graphs, showing two asymptotes that indicate the start and end of a crack's life. The fatigue crack growth curve typically has three distinct regions. The two asymptotes and three distinct regions are clearly indicated in Figure 5.2(a). Regions I through III are characterised as follows:

I Near-threshold region: This region is characterised by a low rate of crack growth, and it corresponds to the initial stages of fatigue loading. In this region, the applied cyclic loading causes microstructural damage to the material, leading to the formation of small cracks. These cracks do not grow significantly during this stage, and the rate of crack growth remains low. The fatigue crack growth curve typically shows two asymptotes at the lower and upper ends of the curve. The lower asymptote is referred to as the fatigue crack growth threshold value, ΔK_{th}. This parameter influences the point at which the crack growth rate begins to increase significantly.

II Crack propagation: This region is characterised by rapid crack growth at an accelerating rate. After crack initiation, the crack propagates through the material under the influence of cyclic loading. The slope of the curve becomes steeper in this region, indicating faster crack propagation. An important equation that describes the propagation of the crack in this region is known as the Paris law. The Paris law, along with the impact of hydrogen on this relationship, is throughly discussed in Section 5.1.2.

III Final fracture: This final region is defined by the rapid propagation of the crack within the material until it ultimately fails. In this region, the crack has grown to a critical size or length. The upper asymptote in the fatigue crack growth curve represents the fracture toughness value of the material, K_{Ic}, which signifies the critical stress intensity level beyond which the crack will propagate unstably, leading to failure. This fracture toughness value serves as an indicator of the maximum stress intensity that the material can withstand before failure. The corresponding value for both the fatigue threshold and fracture toughness are given in Table B.1.

5.1.2. Influence of hydrogen on the Paris law

The relationship in the second region of the fatigue crack growth curve, is referred to as the Paris region. Although the Paris law is already given in Equation 2.6 in Chapter 2.4, the same equation is presented below, to have a complete overview in this section of the different equations needed to obtain a crack growth curve. The power law relationship in the Paris region is the following:

$$\frac{da}{dN} = C\Delta K^{m} \tag{5.2}$$

C and m are the material constants for the Paris law, which can be determined from experimental results. For this analysis, the values for the material constants will be retrieved from the literature for steel in a hydrogen environment. It is important to note that the precise location and shape of each region of the fatigue crack growth curve can vary depending on a variety of factors, such as the material properties, loading conditions, and environmental factors. Nevertheless, the general trends described above for regions I through III are commonly observed and can be used to analyse the fatigue behaviour of materials.

The fatigue crack growth curve, as outlined in the previous section, provides an effective way of portraying the crack growth behaviour under cyclic loading. Nevertheless, it is necessary to consider the effects of hydrogen on the material since its presence can lead to a considerable acceleration of the rate of fatigue crack growth, thus altering the fatigue crack growth curve. Nibur and Somerday conducted an analysis on the effects of H_2 on regions I through III and described these changes in detail [16]. Their findings showed that the largest effects of gaseous hydrogen are observed in region II. This region shows three divisions, which are sequentially indicated as IIa, IIb, and IIc. Region IIa shows similarties to the initial stage of region II on the left. In region IIb, the rate of fatigue crack growth is increased in the presence of hydrogen. Consequently, the slope of the curve is changed in this region. This change is caused by an increased diffusion of hydrogen towards the crack tip [72]. Region IIc shows approximately the same slope as the curve in a non-embrittling environment. The changes in the shape of the curve are visualised in 5.2.

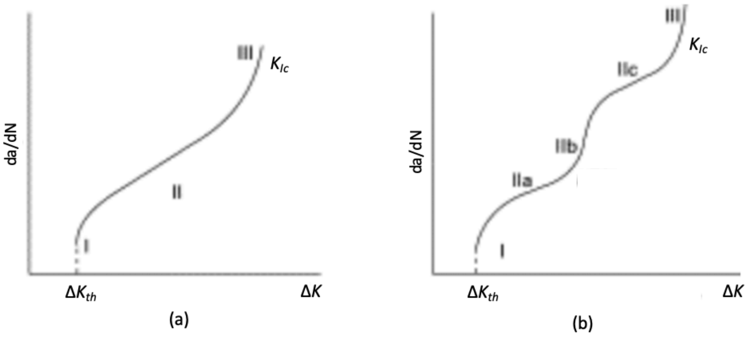

Figure 5.2: Regions of fatigue crack growth rate in (a) non-embrittling environment and (b) gaseous hydrogen environment. Adapted from [16].

The modification of the curve's shape impacts the range in which the Paris law is applicable, leading to corresponding adjustments in the law itself. This results in the identification of three distinct regions within this range. The modifications made to the equation for the Paris law, as originally presented in Equation 5.2, are reflected in Equation 5.3. The relationship and the values to the material constants presented in Equation 5.3 are derived from ASME B31.12-2019 (*The American Society of Mechanical Engineers*) [19]. The specific values assigned to the material constants in Equation 5.3 are defined in Table 5.1.

$$\frac{da}{dN} = C_1\Delta K^{m_1} + \left[\left(C_2\Delta K^{m_2}\right)^{-1} + \left(C_3\Delta K^{m_3}\right)^{-1}\right]^{-1} \tag{5.3}$$

Table 5.1: Values to the material constants in Equation 5.3 considering the influence of hydrogen on the fatigue crack growth curve [19].

Material constant	SI value by ASME B31.12-2019
C_1	4.0812 E-09
m_1	3.2106
C_2	4.0862 E-11
m_2	6.4822
C_3	4.8810 E-08
m_3	3.6147

The Paris law is dimensionally complex. To properly define the units for the material constants C and m in the Paris law, it is crucial to consider the units used for the variables involved. The stress intensity range ΔK is expressed in $N/mm^{\frac{3}{2}}$. The crack depth a is defined in mm. Then, da/dN is measured in $mm/cycle$. The units of C are dependent on the value of m.

5.1.3. Near-threshold region

The first region on the fatigue crack growth curve is characterised by a slow, gradual increase in the crack growth rate as the applied cyclic loading is increased. The crack initiates or grows from an initial starting point. The dimensions of this starting point are commonly indicated by a_0 and c_0, which are the parameters for respectively the initial crack depth and initial crack length.

The British Standard 7910:2013 ($BS7910 : 2013$) demonstrates examples of different flaw profiles [17]. A schematic overview of the flaw considered in the fatigue crack growth model is shown in Figure 5.3. The figure shows an internal surface flaw in a cylinder orientated in the axial direction. The current dimensions of the crack are indicated by a and $2c$, respectively referring to the crack depth and crack length. In this figure, the deepest point of the flaw is indicated by d and the point where the flaw intersects the free surface by s.

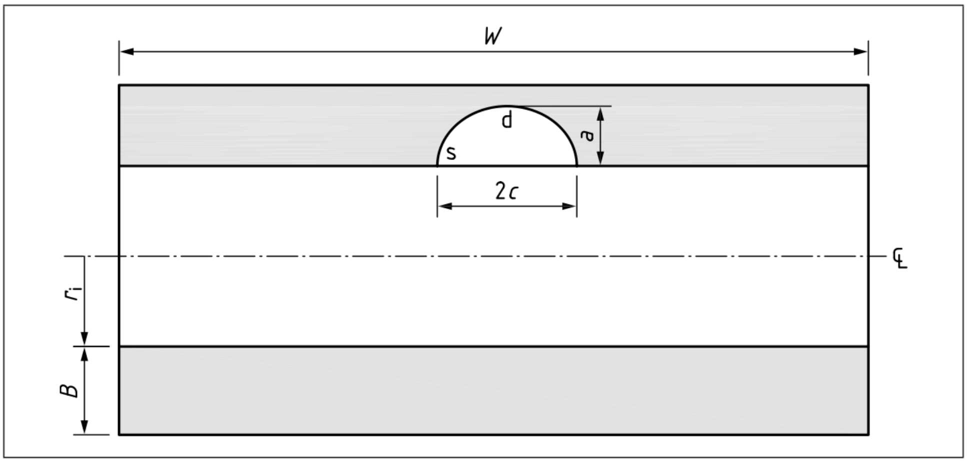

Figure 5.3: Internal surface flaw in cylinder orientated axially [17].

A fatigue crack growth rate assessment requires information on the crack size. In this analysis, the initial crack depth and initial crack length are assumed, and not explicitly provided as part of the case study. This existing crack is expected to grow due to the anchor-pipeline interaction. Assuming the presence of initial cracks in the material is justifiable due to workmanship considerations, which refers to the quality of the work. Workmanship is an important criterion for passing Non-Destructive Evaluation (NDE). NDE techniques are commonly used in manufacturing processes to detect defects, assess structural integrity, and ensure quality control. $BS7910 : 2013$ provides guidance on the minimum flaw size that can be reliably detected using different inspection capabilities (Table T.3 in $BS7910 : 2013$ [17]), and values for both a_0 and c_0 are presented in this Table based on the geometry of the specimen presented in Figure 5.3. Due to workmanship considerations, the industry tends to be cautious and allows only a smaller crack depth of 2 mm, compared to the 3 mm that is presented by $BS7910 : 2013$ [17]. This additional margin provides some allowance for potential errors in NDE sizing and accounts for the possibility of future defect growth that might occur after the initial inspection. As a reference, a detectable defect size of 2 mm x 15 mm (depth x length) is considered, indicating the maximum allowable dimensions for flaws in the analysed pipeline. The values of a_0 and c_0 used in the crack growth analysis can be found in Table B.1.

The point at which the crack growth rate begins to increase significantly is known as the fatigue crack growth threshold. The fatigue crack growth threshold is an important property of a material as it represents the maximum cyclic stress range that the material can withstand without initiating rapid crack growth. This is the region near the threshold point where the crack is just starting to grow. In the fatigue crack growth curve presented in Figure 5.2, this phenomenon is represented by an almost vertical line observed in the low ΔK region.

5.1.4. Crack development

The second region on the fatigue crack growth curve is characterised by a faster rate of crack growth compared to the first region. The crack growth rate remains relatively constant over a range of stress intensity factors, which can be characterised by the Paris law. The stress intensity range is an important parameter in Equation 5.2 and in the field of fracture mechanics. It helps to determine the local stress distribution around the crack tip and forecast the growth of the crack. For fatigue assessments the corresponding stress intensity range is calculated using Equation 5.1c. In the equation for fatigue assessments the following applies:

$$(Y\Delta\sigma) = Mf_w\left(k_{tm}M_{km}M_m\Delta\sigma_m + k_{tb}M_{kb}M_b\left[\Delta\sigma_b + (k_m - 1)\Delta\sigma_m\right]\right) \tag{5.4}$$

This definition follows directly from $BS7910 : 2013$ [17]. The first parameters in Equation 5.4 are the bulging correction factor M and the correction factor f_w. These two factors are defined for various types of flaws. In this particular study, an internal surface flaw in a cylinder orientated in axial direction is considered, which has been introduced prior to this section. The specific parameters and their corresponding values for this configuration are outlined in Table B.1.

The subsequent parameters examined in the equation are the stress concentration factors denoted by k_{tm} and k_{tb}, which are defined for membrane and bending stresses, respectively. A stress concentration factor (SCF) is a dimensionless factor that quantifies the increase in stress at a specific location in a structure, compared to the nominal or average stress in the surrounding region. In the present study, k_{tm} and k_{tb} are assumed to be equal to 1, as no specific information regarding the pipeline weld is available and a through-thickness crack is considered.

Next, the stress magnification factor k_m is introduced, which accounts for any misalignment that may be present in the structure. Bending stresses occuring as a consequence of any deformation from the intended shape or misalignment can be computed by multiplying the applied membrane stress by the stress magnification factor. The calculation for this factor is defined by $BS7910 : 2013$ and is computed using Equation 5.5 [17]. This equation introduces two new parameters, σ_s and P_m, respectively representing the bending stress and applied stress. In this study, σ_s is approximated by the value for the bending stress obtained at maximum pressure in the ANSYS model. Similarly, P_m is approximated by the value for the membrane stress obtained at maximum pressure.

$$k_m = 1 + \frac{\sigma_s}{P_m} \tag{5.5}$$

To solve the equation for the stress intensity range presented in Equation 5.1c for a semi-elliptical weld-toe flaw, the magnification factors for the membrane and bending loading stresses, denoted as M_{km} and M_{kb}, respectively, need to be determined. M_{km} and M_{kb} apply when the flaw is in a region of local stress concentration. The solutions for the stress intensity factor magnification factors are based on 3D-stress analysis of semi-elliptical cracks at weld toes. The validity limits for the solutions given in Equation 5.6 and Equation 5.10 are:

$$0.005 < a/B < 0.9$$
$$0.1 \leq a/c \leq 1.0$$
$$0.5 \leq L/B \leq 2.75$$

The stress intensity magnification factors can be calculated for the deepest and the surface point. These two points are indicated by d and s, respectively, in Figure 5.3. To calculate the stress intensity magnification factor for the deepest point, which considers membrane stresses, Equations 5.6 through 5.9 are utilised. The value for M_{km} is obtained by summing up the functions f_1, f_2 and f_3. To obtain the solutions for these functions, a new set of parameters, represented by g_1 through g_8, is introduced. The solutions to these parameters are also considerably extensive. Hence, the solutions to these parameters are provided in Appendix B.

$$M_{km} = f_1\left(\frac{a}{B}, \frac{a}{c}\right) + f_2\left(\frac{a}{B}\right) + f_3\left(\frac{a}{B}, \frac{L}{B}\right) \tag{5.6}$$

$$f_1\left(\frac{a}{B}, \frac{a}{c}\right) = 0.43358\left(\frac{a}{B}\right)\left(g_1 + \left[g_2\left(\frac{a}{B}\right)^{g_3}\right]\right) + 0.93163e^{\left[\left(\frac{a}{B}\right)^{-0.050966}\right]} + g_4 \tag{5.7}$$

$$f_2\left(\frac{a}{B}\right) = -0.21521\left[1 - \left(\frac{a}{B}\right)\right]^{176.4199} + 2.8141\left(\frac{a}{B}\right)^{-0.10740\left(\frac{a}{B}\right)} \tag{5.8}$$

$$f_3\left(\frac{a}{B}, \frac{L}{B}\right) = 0.33994\left(\frac{a}{B}\right)^{g_5} + 1.9493\left(\frac{a}{B}\right)^{0.23003} + \left[g_6\left(\frac{a}{B}\right)^2 + g_7\left(\frac{a}{B}\right) + g_8\right] \tag{5.9}$$

For the use of the stress intensity magnification factor that takes into account the contribution of bending stresses, an amended range should be employed. Equations 5.10 through 5.13 can be applied when $0.005 \leq a/B \leq 0.5$ to calculate the stress intensity magnification factor for the deepest point, which considers bending stresses. If $0.5 < a/B \leq 0.9$, the value for the stress intensity magnification factor is given as M_{kb} = 1.0. Similar to the equations for the membrane stress, the solution to the bending stress is also complex and can be obtained by summing up the functions f_1, f_2 and f_3. To obtain the solutions for these functions, a second set of parameters, represented by g_1 through g_9, is introduced. Hence, the solutions to these parameters are provided in Appendix B.

$$M_{kb} = f_1\left(\frac{a}{B}, \frac{a}{c}\right) + f_2\left(\frac{a}{B}\right) + f_3\left(\frac{a}{B}, \frac{L}{B}\right) \tag{5.10}$$

$$f_1\left(\frac{a}{B}, \frac{a}{c}\right) = 0.065916\left(\frac{a}{B}\right)^{g_1 + \left[g_2\left(\frac{a}{B}\right)^{g_3}\right]} + 0.52086e^{\left[\left(\frac{a}{B}\right)^{-0.10364}\right]} + g_4 \tag{5.11}$$

$$f_2\left(\frac{a}{B}\right) = -0.02195\left[1 - \left(\frac{a}{B}\right)\right]^{2.8086} + 0.021403\left(\frac{a}{B}\right)^{g_5} \tag{5.12}$$

$$f_3\left(\frac{a}{B}, \frac{L}{B}\right) = 0.23344\left(\frac{a}{B}\right)^{g_6} - 0.14827\left(\frac{a}{B}\right)^{0.20077} + \left[g_7\left(\frac{a}{B}\right)^2 + g_8\left(\frac{a}{B}\right) + g_9\right] \tag{5.13}$$

To calculate the parameters g_1 through g_8 for the membrane stress intensity magnification factor and g_1 through g_9 for the bending stress intensity magnification factor, three ratios are introduced, namely a/c, a/B and L/B. The a/c and a/B ratios take the increasing crack depth a into account, as a result of fatigue crack growth. The a/c ratio illustrates the relationship between the depth of the crack and half the crack length. However, this ratio is assumed to be constant based on consistent spacing of the fatigue striations, which are observed on the fracture surface of a material undergoing fatigue. In this analysis, it is assumed that the crack depth and crack length maintain a proportional relationship during the fatigue crack growth process. Figure 5.4 illustrates fatigue striations on the fracture surface. The a/B ratio illustrates the relationship between the depth of the crack and the wall thickness, and takes the increasing crack depth into account during the fatigue crack growth process.

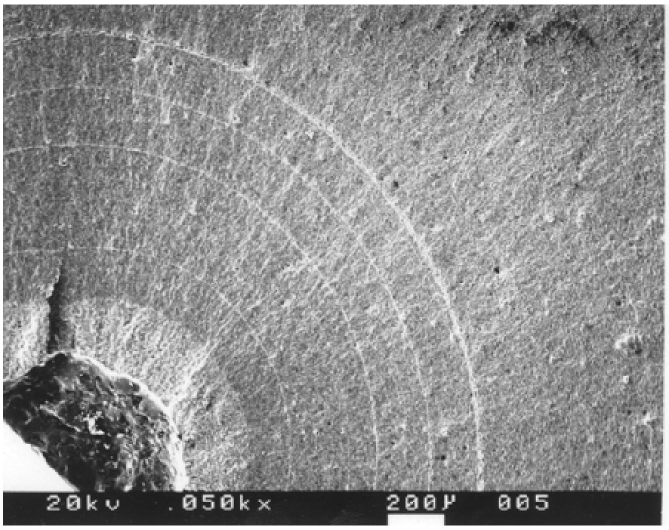

Figure 5.4: Fatigue striation [18].

L denotes the overall length of the weld attachment, measured from one weld toe to the other, while B represents the section thickness in the plane of the crack. Figure 5.5 illustrates the common geometry of a butt weld. Since no detailed information regarding the weld geometry was provided, the value of L is determined based on the experience and expertise of Intecsea, while B is equivalent to the wall thickness. Typically, the value of L is slightly less than B, and is reduced by a few millimeters. The corresponding values can be found in Table B.1.

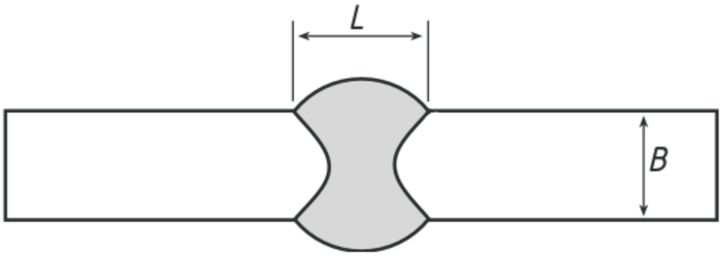

Figure 5.5: Butt weld as illustrated by $BS7910:2013$ [17].

Following the examination of the previous parameters in the equation, the stress intensity magnification factors M_m and M_b are introduced. These factors are also capable of accounting for bending and membrane stresses, and can be defined for both the deepest and surface points. Specifically for the case of an axial internal surface flaw in a cylinder, the values of M_m and M_b are provided in the relevant table in $BS7910:2013$ and are determined based on the ratios of a/B, a/c, and B/r_i [17]. The parameters a, B, c, and r_i have specific values for the configuration considered in Figure 5.3. The determination of the values for a_0 and c_0 has been explained in Section 5.1.3. Similar to the determination of the stress intensity magnification factors, the a/c ratio is assumend to be constant, and the a/B ratio accounts for the increasing crack depth. The values for B and r_i are provided as part of this case study by Intecsea. If the exact values for the a/B, a/c, and B/r_i ratios are not present in Table M2 in $BS7910:2013$, interpolation is permitted according to $BS7910:2013$ [17]. The specific ratios and interpolated values are provided in Table B.1.

Finally, to complete Equation 5.4, the parameters $\Delta\sigma_m$ and $\Delta\sigma_b$ need to be included. $\Delta\sigma$ is defined as the difference between the maximum and minimum stress, σ_{max} and σ_{min}. These parameter values are derived from the ANSYS simulations and are integrated into the fatigue assessment. Further details regarding the integration of ANSYS results into the fatigue assessment are provided in Section 5.2.1, while Section 6.1 specifies the specific values obtained from ANSYS. Equation 5.1 demonstrates the relationship between the maximum stress, minimum stress, and stress intensity range.

After introducing the various parameters in Equation 5.4, the subsequent focus is on analysing the behaviour of crack growth. The development of the crack in this region is typically characterised by a power law relationship between the stress intensity range ΔK and the material constants C and m. This power law relationship between the three parameters is defined as the Paris law in Equation 5.2. It is important to note that the behaviour of region II is different in the presence of hydrogen compared to that in air or vacuum, and this change in behaviour also affects the values of the material parameters C and m. This change in behaviour and the corresponding changes in material parameters have been discussed in detail prior to this section.

5.1.5. Unstable crack growth

The third region on the fatigue crack growth curve is characterised by a significant increase in crack growth rate. In this region, rapid crack growth occurs when the crack reaches a critical size. The critical crack size is the depth at which the crack becomes unstable and experiences rapid propagation. At this critical size, the stress intensity factor, which is a measure of the magnitude of the applied stress at the crack tip, exceeds the material's fracture toughness K_{Ic}, leading to rapid crack growth and ultimately to failure. In other words, the crack is able to propagate through the material without further increase in the applied stress, leading to a sudden and catastrophic failure of the material. The failure criteria for this model will be further discussed in section 5.2.4.

5.2. Model set-up

The preceding section discussed the different regions of the fatigue crack growth curve and how the crack growth rate varies with the applied stress intensity range in a hydrogen environment. The factors that affect the stress intensity range have been exhaustively elaborated. The associated numerical values are available in Table B.1.

This section introduces the application of the fatigue crack growth equation and its parameters given in Section 5.1 to create a mathematical model in Matlab, which generates a crack growth curve (a versus N) for the specific situation analysed in this thesis. In addition, the failure criteria that are used to determine the failure of the pipeline will also be discussed. The analysis of the failure criteria is an important aspect of the development of the fatigue crack growth model, as it enables the identification of the critical crack size and the prediction of the remaining life of the structure.

5.2.1. Integration of ANSYS results

The integration of ANSYS simulations, fatigue assessment, and fracture assessment highlights the interconnectedness of the components involved in analysing fatigue crack growth and the risk of failure. By examing the pressure spectrum, the stress distribution at critical points can be extracted from ANSYS simulations. The membrane and bending stress distribution is determined at maximum pressure ($p_{\max}$), 90% pressure ($p_{90\%}$), and 50% pressure ($p_{50\%}$), representing daily and yearly variations in pressure due to loading cycles. By considering the stress distribution obtained from ANSYS simulations and integrating it into the fracture and fatigue assessments, a comprehensive understanding of the pipeline's response to anchor impact and the potential for fatigue crack growth and failure can be achieved. This integrated approach enables accurate evaluation of the maximum allowable crack depth. From the obtained stress distribution, the maximum stress value (σ_{max}) can be determined. This σ_{max} value plays a crucial role as a direct input for the fracture assessment. It is used in the computation of the load ratio L_r, which is an critical parameter in evaluating the maximum allowable crack depth. Additionally, the stress range ($\Delta\sigma$) is derived from the maximum and minimum stress values within the stress distribution. This stress range serves as input for the fatigue assessment, where it is used to determine the stress intensity range.

5.2.2. Calculation procedure

The flowchart in Figure 5.1 depicts a crack growth simulation in a material subjected to cyclic loading. The cyclic loading causes the crack to grow incrementally with each cycle, eventually leading to failure if the crack reaches a critical size. The iterative process outlined in the flowchart allows for the estimation of the remaining fatigue life of a material in terms of the number of cycles to failure. Figure 5.1 also shows the interconnectedness of the processes within the fatigue crack growth model and ANSYS simulations.

The left side of the flowchart shows the process of setting up the a versus N curve, which is a plot of the crack depth (a) as a function of the number of loading cycles (N) that the material experiences. The iterative process involves incrementally increasing the crack depth with each cycle until the critical crack depth is reached. In Section 5.2.3, the process of iteratively determining the a versus N curve is clarified.

Once the a versus N curve is established using the above approach, the failure assessment can be performed. The right side of the flowchart shows the process of failure assessment, which is used to determine when the material will fail based on the calculated crack size and the applied stress. The maximum acceptable crack depth can either be determined from a Failure Assessment Diagram, which considers factors such as material properties and loading conditions, or when the crack depth is equal to the wall thickness, B. The maximum acceptable crack depth can be used to define a horizontal line on the a versus N curve. The point at which the crack growth curve intersects with this line indicates the number of cycles until failure for the given conditions. The FAD will be elaborated upon in Section 5.2.4.

5.2.3. Crack growth curve: crack depth versus number of cycles

The iterative process, which is depicted in the flowchart in Figure 5.1, consists of gradually increasing the crack size with each cycle until the maximum allowable crack depth is attained. The maximum allowable crack depth follows from the FAD, explained in Section 5.2.4. These processes ultimately determine the post-hooking lifetime of the pipeline. This section provides a detailed explanation of the left side of the flowchart in Figure 5.1, which describes the process of setting up the crack growth curve.

The simulation begins from the initial crack depth (a_0), which has been defined in Section 5.1.3. The primary step in the simulation, which is iteratively performed, involves verifying whether the crack depth exceeds either the maximum allowable crack depth derived from the FAD (a_{max}) or the wall thickness (B). The simulation proceeds until the crack depth reaches this criterion for the crack depth. The subsequent steps describe the process when the crack depth is below the specified criterion. The first step involves determining the stress intensity range, as this is an important parameter in the Paris law. The maximum and minimum stress (respectively σ_{max} and σ_{min}) specify the stress range ($\Delta\sigma$). These values are obtained from the stress distribution derived from ANSYS. The crack growth rate da/dN is then determined using the Paris law, which relates it to the stress intensity factor range. To calculate the amount of crack growth that occurs during each iteration, the crack growth rate is combined with the cycle step size. The step size for the number of cycles between each iteration (ΔN) is chosen according to preference. Specific values for the parameters taken into consideration for the fatigue crack growth model can be found in Appendix B.

After calculating the crack growth for a particular iteration, the corresponding crack depth is determined for that cycle step. The updated crack size is then evaluated, and its value is compared to the predefined criterion. The simulation continues until the crack size reaches a critical size that satisfies the failure condition, resulting in material failure.

5.2.4. Failure criteria

The critical crack size for fatigue crack growth scenarios is typically defined as the size of a crack at which the rate of crack growth increases rapidly and leads to eventual failure of the component. Understanding the critical crack size is essential in predicting the remaining useful life of a damaged structure.

The crack growth simulation presented in the flowchart in Figure 5.1 is used to generate a plot that shows the relationship between the crack size (a) and the number of cycles (N). To estimate the post-hooking lifetime of a hydrogen pipeline following anchor impact, two potential failure conditions can be assessed. The first condition is based on the wall thickness of the pipeline, where the crack depth reaches the thickness of the wall. The second condition is based on the FAD, which provides a maximum allowable crack depth. The FAD is a widely used approach for conducting elastic-plastic fracture mechanics analysis of structural components. These two conditions can be represented in the plot of crack size (a) versus number of cycles

(N) as two horizontal lines corresponding to the respective crack depths. The intersection of the crack growth curve with the first horizontal line determines the post-hooking lifetime of the pipeline.

This section highlights the different components located on the right side of the flowchart presented in Figure 5.1. The process of setting up the FAD and defining the maximum allowable crack depth a_{max} is examined. This maximum allowable crack depth is subsequently used as input for the fatigue assessment process. The first step is to define the assessment line and cut-off value.

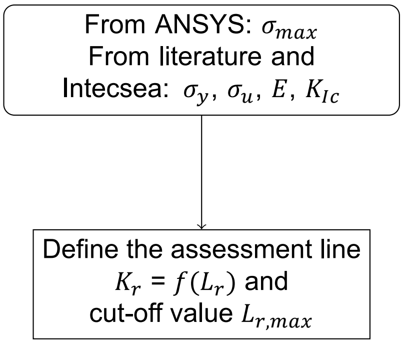
From ANSYS: σ_{max}
From literature and
Intecsea: σ_y, σ_u, E, K_{Ic}
Define the assessment line
K_r = $f(L_r)$ and
cut-off value $L_{r,max}$

Figure 5.6: First phase on the fracture flowchart: define the assessment line and cut-off value.

The approach to define the assessment line is explained by $BS7910 : 2013$ [17]. There are three different approaches, each of increasing complexity. The assessment line K_r and cut-off value $L_{r,max}$ for each approach are respectively defined by Equation 5.14 and Equation 5.15:

$$K_r = f(L_r) \tag{5.14}$$

$$L_{r,max} = \frac{\sigma_y + \sigma_u}{2\sigma_y} \tag{5.15}$$

The first option proposed by $BS7910 : 2013$ is considered sufficiently reliable and suitable for application in this thesis [17]. The equations that define the assessment line are as follows:

$$f(L_r) = \left(1 + \frac{1}{2}L_r^2\right)^{-1/2} \left[0.3 + 0.7exp(-\mu L_r^6)\right] \qquad \text{for } L_r \leq 1 \tag{5.16a}$$

$$f(L_r) = f(1)L_r^{(N_f-1)/(2N_f)} \qquad \text{for } 1 < L_r < L_{r,max} \tag{5.16b}$$

$$f(L_r) = 0 \qquad \text{for } L_r \geq L_{r,max} \tag{5.16c}$$

These equations introduce two variables, μ and N. These variables can be determined using the following relationships in Equation 5.17 and Equation 5.18:

$$\mu = min\left(0.001\frac{E}{\sigma_y}, 0.6\right) \tag{5.17}$$

$$N_f = 0.3\left(1 - \frac{\sigma_y}{\sigma_u}\right) \tag{5.18}$$

Using the aforementioned equations and definitions, it is possible to define a Failure Assessment Diagram specific to the material properties under consideration. The values for the Young's modulus (E), yield strength (σ_y), and ultimate tensile strength (σ_u) can be found in Table B.1. Figure 5.7 illustrates the FAD used in this assessment.

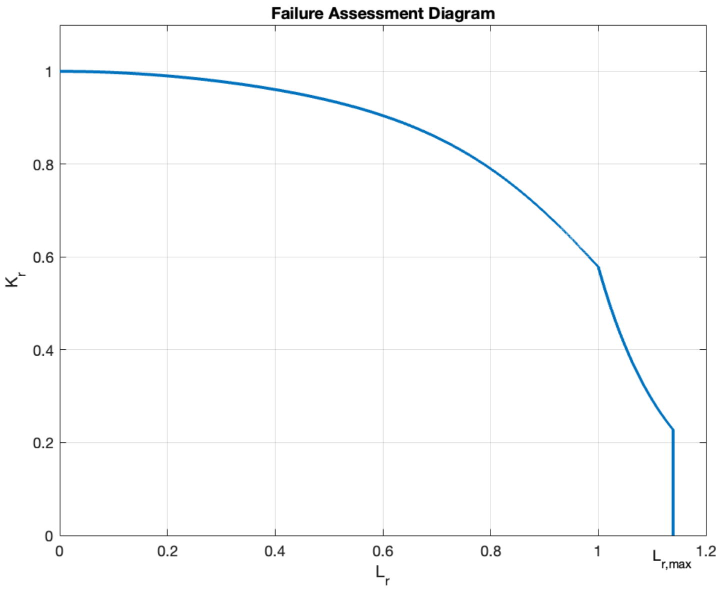

Figure 5.7: The Failure Assessment Diagram consists of the assessment line K_r and cut-off value $L_{r,max}$.

The subsequent phase involves two key stages. In the first stage, the load ratio L_r is determined based on the maximum stress σ_{max}, which is obtained using the results for σ_m and σ_b from the ANSYS simulations, using Equation 5.19. Once the value of L_r is established, the second stage focuses on finding the corresponding value for the toughness ratio K_r for σ_{max} from the FAD.

$$L_r = \frac{\sigma_{max}}{\sigma_y} \tag{5.19}$$

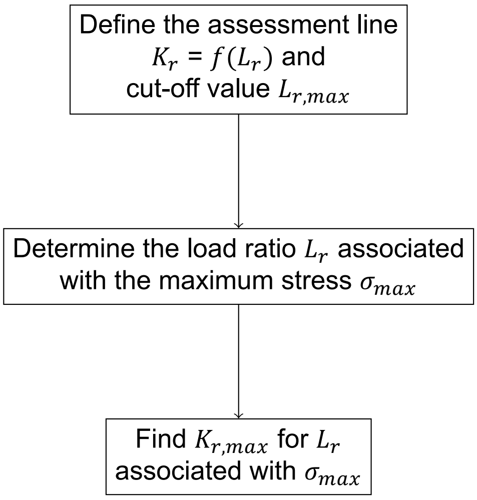
Define the assessment line $K_r = f(L_r)$ and cut-off value $L_{r,max}$
Determine the load ratio L_r associated with the maximum stress σ_{max}
Find $K_{r,max}$ for L_r associated with σ_{max}

Figure 5.8: Second phase on the fracture flowchart: determine L_r and find K_r associated with σ_{max}.

The specific K_r value that corresponds to σ_{max} is denoted as $K_{r,max}$. After obtaining the value of $K_{r,max}$ at the value of L_r corresponding to σ_{max}, the maximum stress intensity factor ($K_{I,max}$) can be calculated using the relationship for the toughness ratio. The toughness ratio depends on the relationship between the stress intensity factor and the plane strain fracture toughness. As such, the stress intensity factor corresponding to $K_{r,max}$ is denoted as $K_{I,max}$. The general definition of the toughness ratio is given by the following expression:

$$K_r = \frac{K_I}{K_{Ic}} \tag{5.20}$$

This phase involves two stages. In the first stage, the relationship for the toughness ratio is solved to obtain the value of $K_{I,max}$. Subsequently, this value is utilised to determine the maximum allowable crack depth, denoted as a_{max}. This step involves solving the equation for the stress intensity factor to find the maximum allowable crack depth a_{max}. This value serves as a criterion on the crack growth curve described in Section 5.2.3. The results to this procedure are described in Section 6.2.1.

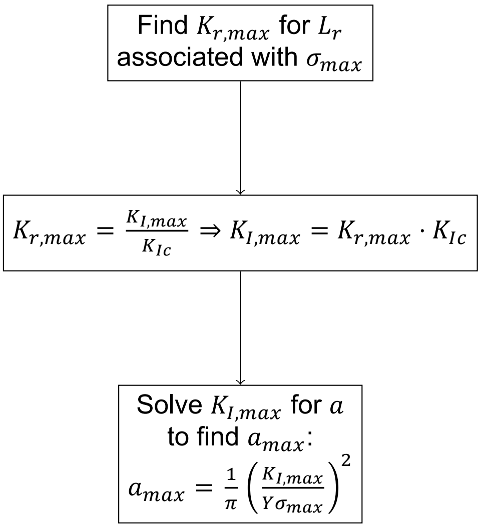
Find $K_{r,max}$ for L_r associated with σ_{max}
$K_{r,max} = \frac{K_{I,max}}{K_{Ic}} \Rightarrow K_{I,max} = K_{r,max} \cdot K_{Ic}$
Solve $K_{I,max}$ for a to find a_{max}:
$a_{max} = \frac{1}{\pi}\left(\frac{K_{I,max}}{Y\sigma_{max}}\right)^2$

Figure 5.9: Third phase on the fracture flowchart: solve the toughness ratio for $K_{I,max}$ and determine the maximum allowable crack depth a_{max} using the equation for the stress intensity factor.

6
Results

This chapter reviews the results derived from the ANSYS model, which simulates the behaviour of an offshore pipeline dragged by an anchor. In addition, the chapter assesses the fatigue crack growth model developed in Matlab, incorporating the specific behaviour of the Paris law in the presence of hydrogen and the insights derived from the ANSYS simulations. By analysing these findings, this chapter provides valuable insight into the pipeline's behaviour after anchor impact and the evaluation of fatigue crack growth in the presence of hydrogen.

The interconnectedness between ANSYS simulations, fatigue assessment, and fracture assessment has been introduced in Chapter 3. Chapter 4 follows the first part of the methodology and defines the interaction between the anchor and the pipeline. Section 5.2.3 and Section 5.2.4 provided detailed explanations of the subsequent steps within the fatigue and fracture assessments, as well as how the results from different models can be integrated. The present chapter examines the results obtained from the numerical simulations and the fatigue crack growth model.

6.1. Numerical simulation results

The first section of this chapter focuses on the results obtained from the numerical simulations in ANSYS, which have been introduced in Chapter 4. These results provide insight into the behaviour of the pipeline system under the influence of an external load applied by an anchor. The results from the mesh independence study are also presented in this section. This study serves as a means of validating the simulation model and ensures the reliability of the obtained results. The insights gained from the simulations form the basis for understanding the effects of the anchor-pipeline interaction. Eventually, this enables the assessment of the post-hooking lifetime of a pipeline damaged by an anchor.

6.1.1. Stress variations

The ANSYS simulations give insight into the membrane and bending stresses at various pressure levels in the pipeline after anchor impact. The procedure in ANSYS consists of three distinct steps, corresponding to the time steps described in Section 4.2.1. The pipeline is pressurised at p_{max} during the first time step. Next, the anchor and pipeline are moved over a distance of 2.5 m during a time period of 10 s to establish the termination point of the simulation. During this step, the pipeline is continuously pressurised at p_{max}. The termination criterion for the simulation is described in Section 4.2.3. The calculation of the minimum breaking load is defined by Equation 4.1. Solving this equation for an anchor weight of 2300 kg, results in a minimum breaking load of 575 kN. In Figure 6.1, the reaction force over time on the anchor in the y-direction is depicted. The maximum reaction force obtained during the simulation at p_{max} corresponds to approximately 185 kN. As this is the maximum reaction force obtained during the simulation, the earlier obtained value for the minimum breaking load is no longer taken into account, and the time corresponding to the maximum reaction force of 185 kN is chosen as an end point for the simulation.

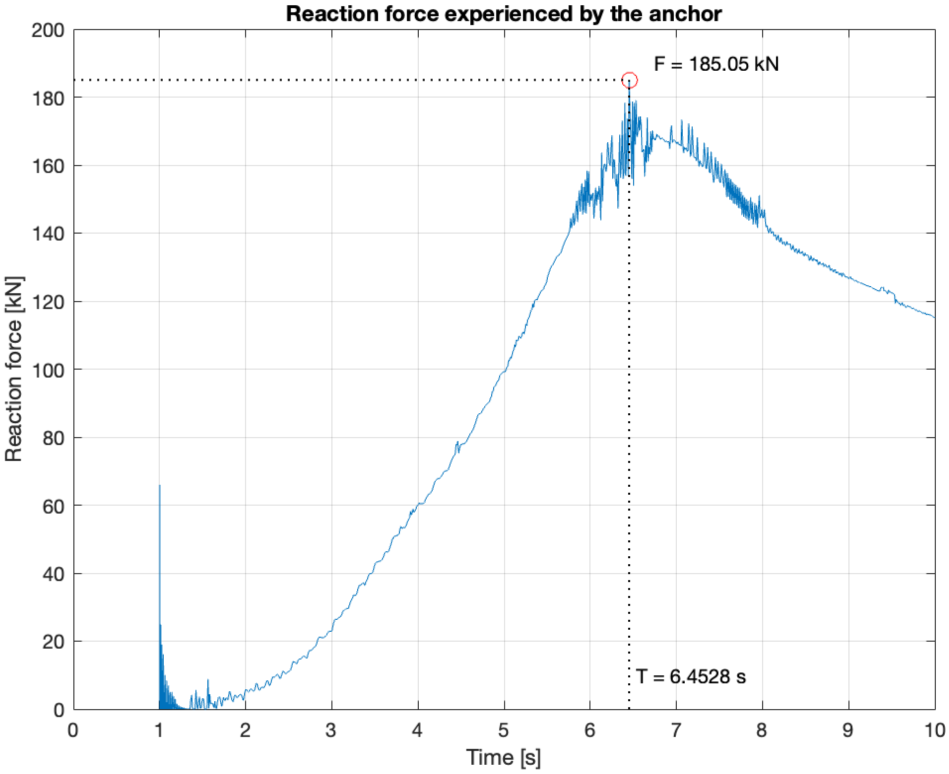

Figure 6.1: The end of the simulation is determined based on the highest reaction force experienced by the anchor during the simulation.

Figure 6.2 shows the final deformation observed after the simulation has ended at $T = 6.4528$ s. Once the pipeline is pressurised, the anchor moves in the positive y-direction, dragging the pipeline along. The change in position compared to the starting point is clearly visible in the YZ-plane, which is depicted in Figure 6.2. This deviation occurs because the pipeline is fixed at the end of the beam element, and that specific point doesn't move or rotate with respect to the x, y, or z axis. At its initial position, the faces of the pipeline at the point of impact are aligned perpendicular to the fixed end of the beam element.

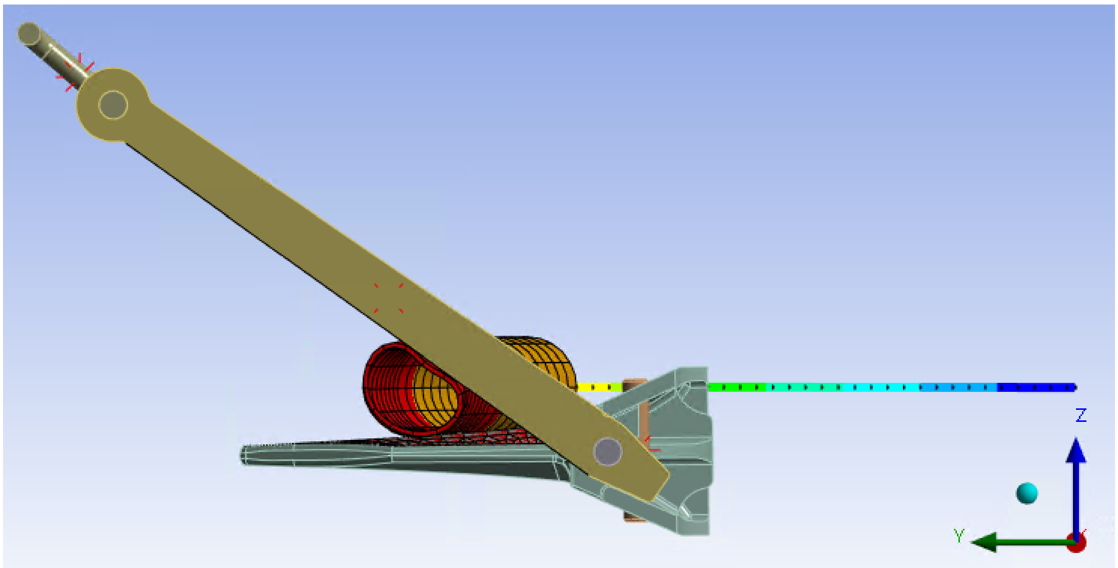

Figure 6.2: The pipeline deformation at the end of the simulation at $T = 6.4528$ s.

The third and final step is important in achieving the desired results. In Section 5.2.1, the integration of ANSYS results into the fatigue and fracture assessments was discussed, providing a brief overview of the obtained results from the ANSYS simulations. The examination of the pressure spectrum in the ANSYS simulations enables the retrieval of the stress at critical points. Once the termination point of the dragging process is established, which corresponds to the end of the second time step, the pipeline is pressurised at different levels during the third time step. Three pressure levels are evaluated: maximum pressure (p_{max}), 90% pressure ($p_{90\%}$), and 50% pressure ($p_{50\%}$), of which the last two respectively represent the daily and yearly variations in pressure resulting from loading cycles. At the end of the third time step, the membrane and bending stress are calculated at these key pressure levels. The stress levels at the maximum pressure are used in the determination of the maximum stress intensity factor (K_{max}), defined in Equation 5.1a, which plays a role in determining the maximum allowable crack depth at a later stage of the process. The stress range ($\Delta\sigma$) is computed using the stress values obtained at the maximum pressure (p_{max}), 90% pressure ($p_{90\%}$), and 50% pressure ($p_{50\%}$). The stress range is included in the calculation of the stress intensity range (ΔK), which depends on the factor $Y\Delta\sigma$. ΔK is used in the Paris law to determine the fatigue crack growth rate. The calculation of the stress intensity range is defined in Equation 5.1c.

To retrieve the membrane and bending stresses at the different pressure levels from ANSYS, the definitions for the linearisation of stress distributions from $BS7910 : 2013$ are used [17]. Equation 6.1 for the membrane stress and Equation 6.2 for the bending stress introduce two new parameters, the principal stresses σ_1 and σ_2. The equations as defined by $BS7910 : 2013$ are as follows:

$$\sigma_m = \frac{\sigma_1 + \sigma_2}{2} \qquad (6.1) \qquad\qquad \sigma_b = \frac{\sigma_1 - \sigma_2}{2} \qquad (6.2)$$

To obtain the approach used in this study, a modification is required due to the assumption that the principal stresses, as defined by the calculation from $BS7910 : 2013$, may not be equal to the maximum stress occurring through the thickness. In accordance with the definition provided in $BS7910 : 2013$, the stress distribution is linearised over the depth of the flaw. However, in the present study, it is assumed that the crack grows through the thickness, which requires a linearisation of the stress through the thickness as well. The calculation for the membrane and bending stress, as presented in Equation 6.1 and Equation 6.2, is applied with a slight modification regarding the approximation of σ_1 and σ_2. Instead of using the earlier mentioned principal stresses, the normal stress in the x-direction is obtained at the inner and outer walls of the pipeline. Both on the inner and outer wall, two nodes are located in the positive x-direction. The stresses retrieved from these nodes are denoted as $\sigma_{xx,in}$ for the stress at the inner wall and $\sigma_{xx,out}$ for the stress at the outer wall. The adapted equations are as follows:

$$\sigma_m = \frac{\sigma_{xx,in} + \sigma_{xx,out}}{2} \qquad (6.3) \qquad\qquad \sigma_b = \frac{\sigma_{xx,in} - \sigma_{xx,out}}{2} \qquad (6.4)$$

To determine the membrane and bending stress values at the specified pressure levels, a specific location is chosen from which to extract the normal stresses. The selection process involves evaluating the von-Mises stress across the entire pipeline and identifying a specific section based on the maximum von-Mises stress at p_{max}. The calculation of the membrane and bending stress involves systematically selecting three elements through the thickness. Initially, a column is chosen where the maximum von-Mises stress is observed. From this selected column, the specific row with the highest von-Mises stress is identified.

Subsequently, this section is separated from the remaining portion of the pipeline, leaving three elements through its thickness. At this location, two nodes on both the inner and outer surface, located in the positive x-direction, are considered. First, the node on the inner wall with the highest normal stress in the x-direction is identified. The stress on the outer wall is retrieved from the node that lies on the same edge (through thickness). The membrane and bending stresses can be calculated using Equation 6.3 and Equation 6.4. These values will be used in the calculation for the fatigue crack growth. The section with the three elements shown in Figure 6.3 corresponds to the bottom right section of the cross section depicted in Figure 4.8.

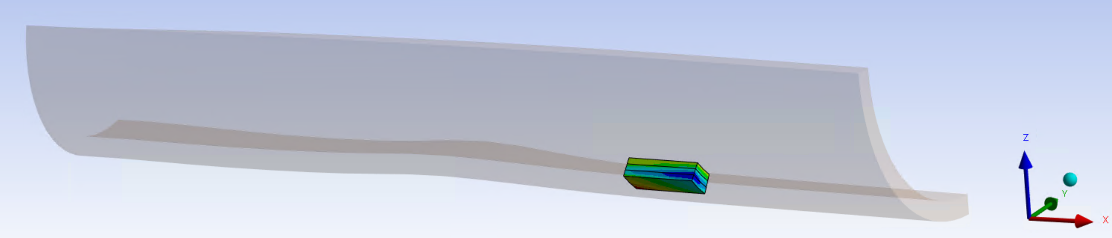

Figure 6.3: Three elements through thickness at the location where the maximum von-Mises stress is obtained. From the location the membrane and bending stresses at different pressure levels are retrieved.

Once the location has been defined, the ANSYS simulation is conducted specifically at the designated pressure levels in the third time step in order to obtain the membrane and bending stress values. The internal pressurisation of the ANSYS model is achieved through gauge pressure. For this analysis, $p_{\max}$ is assumed to be equal to the gauge pressure and is set at 3532 kPa, while $p_{90\%}$ corresponds to 3179 kPa and $p_{50\%}$ corresponds to 1766 kPa.

After executing the model under the specified pressures, $\sigma_{xx,in}$ and $\sigma_{xx,out}$ are evaluated at the specific location. The corresponding values for these parameters are presented in Table 6.1. By solving Equation 6.3 and Equation 6.4, the values for σ_m and σ_b at $p_{\max}$, $p_{90\%}$, and $p_{50\%}$ are found. These values are also represented in Table 6.1. Following these calculations, the stress range is determined by subtracting the stress values obtained at $p_{\max}$, $p_{90\%}$, and $p_{50\%}$. The daily stress range is determined by taking the difference between the stress levels at the maximum pressure and 90% pressure, while the yearly stress range is determined by taking the difference between the stress levels at the maximum pressure and 50% pressure. This procedure is similar for membrane and bending stress. The values for the membrane and bending stress ranges for daily and yearly variations are presented in Table 6.2.

Table 6.1: Values for the inner and outer stress in the x-direction and corresponding membrane and bending stress at $p_{\max}$, $p_{90\%}$, and $p_{50\%}$.

		p_{max}	$p_{90\%}$	$p_{50\%}$
$\sigma_{xx,in}$	[MPa]	280	276	251
$\sigma_{xx,out}$	[MPa]	270	270	262
σ_m	[MPa]	275	273	256.5
σ_b	[MPa]	5	3	-5.5

Table 6.2: Calculation for the daily and yearly variations in membrane and bending stress.

$\Delta\sigma_{m,daily}$	[MPa]	2
$\Delta\sigma_{b,daily}$	[MPa]	2
$\Delta\sigma_{m,yearly}$	[MPa]	18.5
$\Delta\sigma_{b,yearly}$	[MPa]	10.5

Figure 6.4 displays the stress values on the inner and outer walls of the pipeline at different pressure levels. From these values, the corresponding membrane and bending stress are calculated.

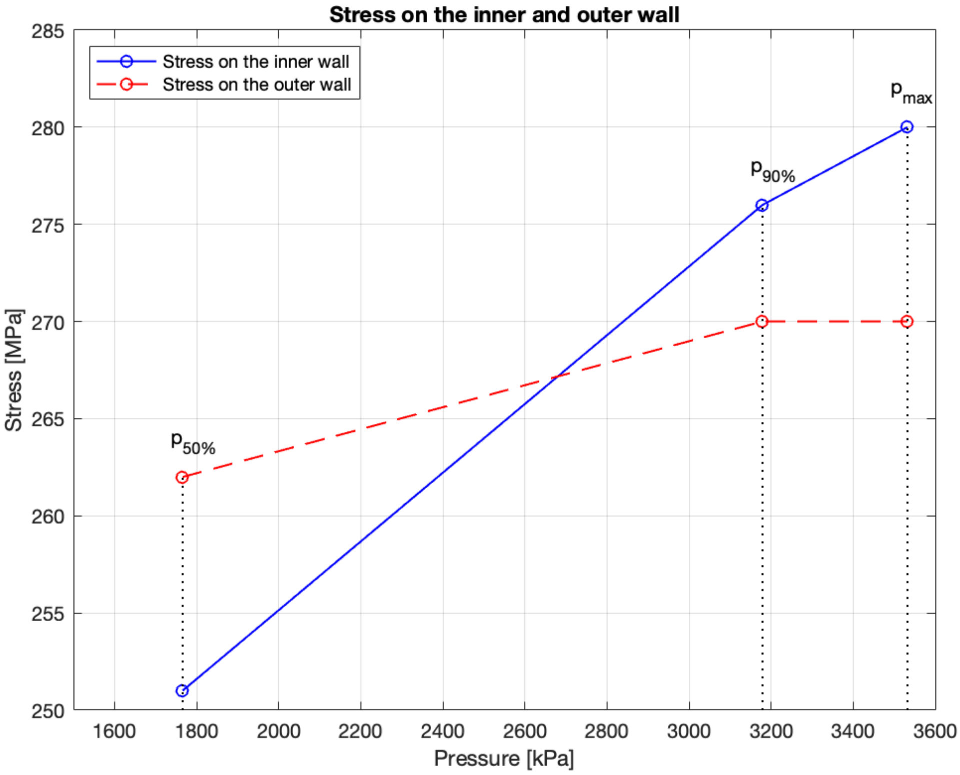

Figure 6.4: Stress on the inner and outer wall at maximum pressure (p_{max}), 90% pressure ($p_{90\%}$), and 50% pressure ($p_{50\%}$).

6.1.2. Mesh independence study

Section 4.1.2 discusses the importance of conducting a mesh independence study to determine the appropriate number of elements in different directions (radial, hoop, and longitudinal). The purpose of this study is to assess the impact of mesh density on the simulation results. In a mesh independence study, the number of elements is systematically varied while keeping other simulation parameters constant. The study is performed at maximum pressure (p_{max}). Initially, the von-Mises stress is evaluated over the entire pipeline, and a specific section with the highest stress is selected for the mesh independence study. Figure 6.5 illustrates the maximum von-Mises stress obtained from different mesh configurations, with the objective of assessing convergence and determining the mesh size that provides consistent and reliable results. The analysis starts with an initial mesh consisting of approximately 400 elements. In the next step, the initial mesh is refined, and the corresponding solution for von-Mises stress is evaluated. This iterative process continues until convergence is achieved. The analysis aims to identify a specific point where a large increase in the number of nodes no longer results in a significant increase in von-Mises stress. From the relationship between the number of elements and von-Mises stress follows that a minimum of 5000 elements is required to get a mesh independent stress. In the ANSYS simulation this corresponds to a total of 5022 elements. The specific number of divisions per direction are stated in Section 4.1.2.

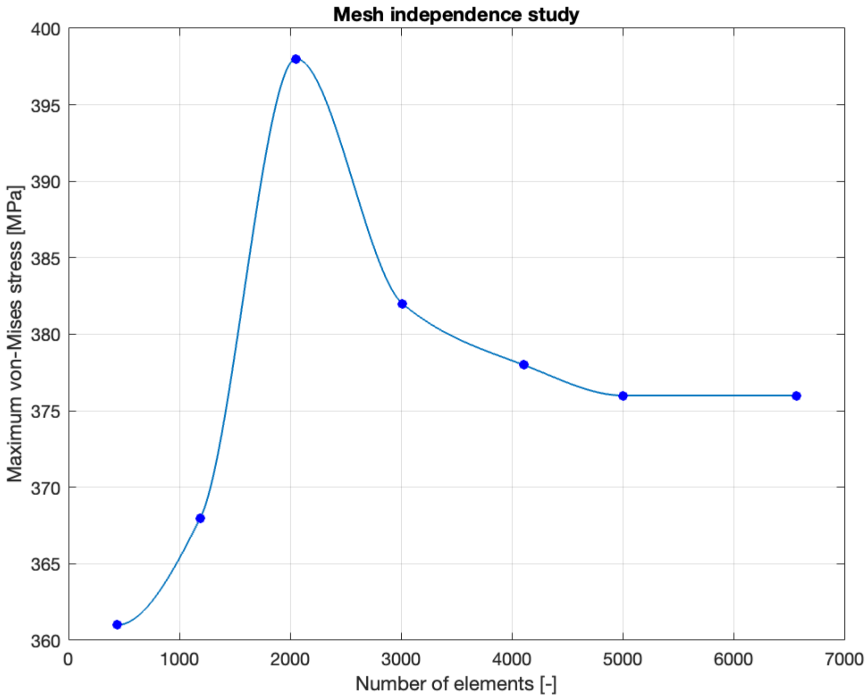

Figure 6.5: The mesh independence study shows that convergence is obtained at a minimum of 5000 elements.

6.2. Crack growth model results

This section presents the outcomes of the crack growth model, as discussed in Chapter 5. The focus is on providing the results obtained from the analysis, including the determination of the maximum allowable crack depth based on the FAD. Subsequently, the number of cycles to failure is determined using the obtained data.

6.2.1. Maximum allowable crack depth from Failure Assessment Diagram

Section 5.2.4 outlined the procedure of setting up the FAD and determining the maximum allowable crack depth, denoted as a_{max}. The assessment line K_r and cut-off value $L_{r,max}$ were introduced and illustrated in Figure 5.7. The subsequent step involves calculating the load ratio L_r at σ_{max}. This calculation procedure was previously defined in Equation 5.19. The value of σ_{max} is determined based on the stress distribution across a section, as outlined in $BS7910 : 2013$, and is calculated using Equation 6.5. This equation takes σ_m and σ_b into consideration. These values follow from the ANSYS simulation executed at the maximum pressure, indicated by $\sigma_{m,max}$ and $\sigma_{b,max}$. Consequently, the value for the load ratio is computed using Equation 6.6.

$$\sigma_{max} = k_{tm}\sigma_{m,max} + k_{tb}\left[\sigma_{b,max} + (k_m - 1)\,\sigma_{m,max}\right] \tag{6.5}$$

$$L_r = \frac{\sigma_{max}}{\sigma_Y} = \frac{285\text{MPa}}{360\text{MPa}} = 0.7917 \tag{6.6}$$

The next step is the determination of the corresponding toughness ratio, denoted as $K_{r,max}$. This is accomplished by identifying the intersection point between the vertical line from the calculated L_r value and the assessment line. Figure 6.6 provides a visual representation of this process, with the resulting value for $K_{r,\text{max}}$ at the point of intersection, which is located at L_r equal to 0.7917. The value for $K_{r,\text{max}}$ that is retrieved from this figure is 0.7967.

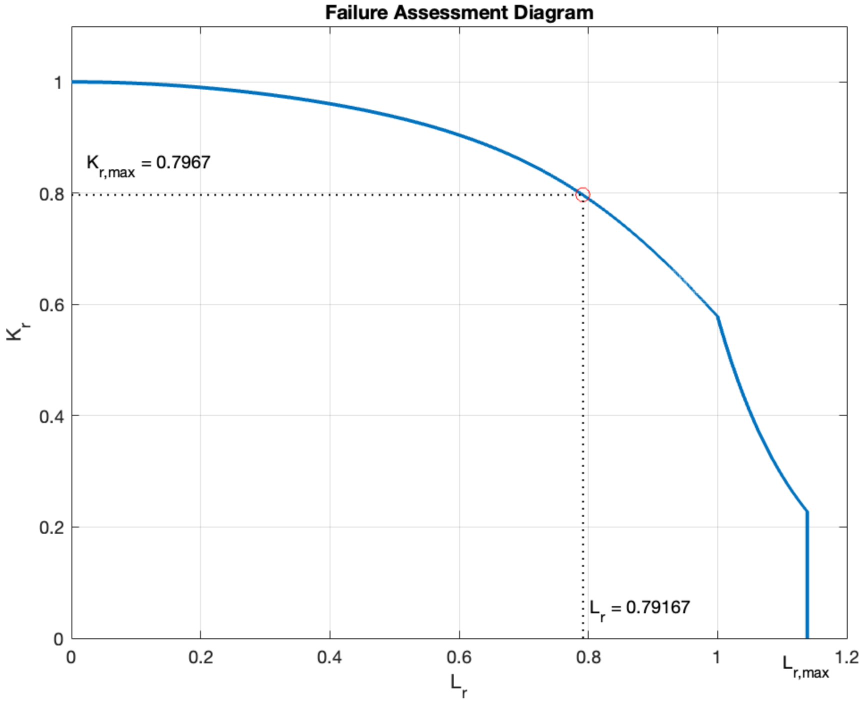

Figure 6.6: The matching value for K_r can be found by drawing the intersection at L_r = 0.8.

The final step in this process is to determine the maximum allowable crack depth, denoted as a_{max}. The calculation for a_{max} is as follows:

$$a_{max} = \frac{1}{\pi}\left(\frac{K_{I,max}}{Y\sigma_{max}}\right)^2 \tag{6.7}$$

In order to determine the maximum allowable crack depth, it is necessary to calculate the maximum stress intensity factor, denoted as $K_{I,max}$. The calculation of $K_{I,max}$ involves using the toughness ratio, defined by Equation 5.20. The calculation of $K_{I,max}$ is based on the relationship between the toughness ratio corresponding to the maximum stress ($K_{r,max}$), which is retrieved from the FAD in Figure 6.6, and the plane strain fracture toughness (K_{Ic}), which is defined in Table B.1. The resulting value for $K_{I,max}$ is:

$$K_{I,\max} = K_{r,\max} \cdot K_{Ic} \tag{6.8}$$

The factor $Y\sigma_{max}$ is determined by Equation 6.9. This equation incorporates parameters that are largely similar to those defined in Equation 5.4. However, instead of considering the stress range, it takes into account the maximum membrane and bending stresses. The maximum membrane and bending stresses are derived from the simulations in ANSYS and the corresponding values are presented in Section 6.1.1. The parameters M_m, M_b, M_{km}, and M_{kb} are dependent on the crack depth a and the crack length c. When calculating $Y\sigma_{max}$, a constant a/c ratio is assumed, as discussed in Section 5.1.4. The a/B ratio does not consider the increasing crack depth, and is calculated based on the initial crack depth, as a_0/B.

$$Y\sigma_{max} = Mf_w\left(k_{tm}M_{km}M_m\sigma_{m,max} + k_{tb}M_{kb}M_b\left[\sigma_{b,max} + (k_m - 1)\sigma_{m,max}\right]\right) \tag{6.9}$$

Implementing the obtained results and the values defined in Table B.1 for the parameters in Equation 6.8 and Equation 6.9 the following values for $K_{I,max}$ and $Y\sigma_{max}$ are established:

$$K_{I,max} = 1384\,\mathrm{N/mm}^{\frac{3}{2}}$$
$$Y\sigma_{max} = 285\,\mathrm{N/mm}$$

By solving Equation 6.7 for these values for $K_{I,max}$ and $Y\sigma_{max}$, a maximum allowable crack depth of 7.52 mm is found.

6.2.2. Number of cycles to failure

Section 5.2.3 explained the iterative process of setting up the crack growth curve, which is a plot of the crack depth (a) as a function of the number of loading cycles (N) that the material experiences. The crack growth curve shows how the crack depth evolves over time as the material is subjected to repeated loading cycles. The crack growth curve is defined for daily and yearly variations in pressure. Figure 6.7 and Figure 6.8 provide a visual representation of the crack growth curve. The figures also include two horizontal lines that represent the maximum allowable crack depth based on the FAD and the through-thickness crack depth. These failure criteria were introduced in Section 5.2.4, and the results of the FAD are presented in Section 6.2.1. The number of cycles until failure is determined by the first point at which the crack growth curve intersects either of the horizontal lines that represent the failure criteria.

Taking into account daily variations in pressure, the number of cycles required to reach the crack depth until failure is determined from Figure 6.7. The number of cycles until failure is 22421 days. For yearly variations in pressure, the number of cycles until failure is determined from Figure 6.8. The number of cycles until failure is approximately 8 years.

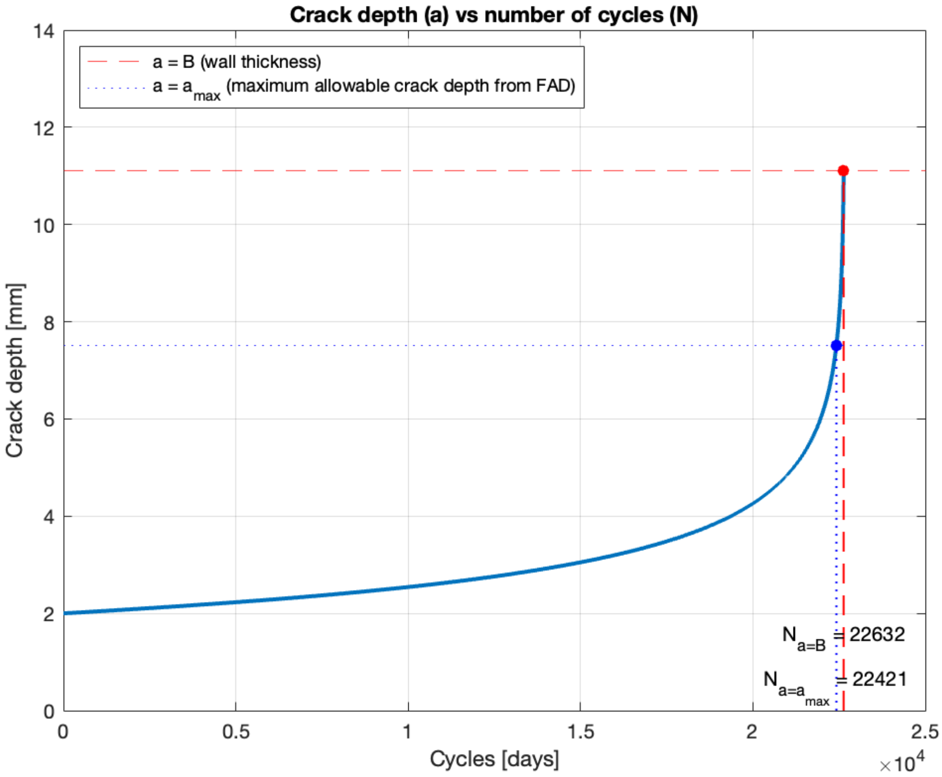

Figure 6.7: The crack growth curve with criteria for the maximum allowable crack depth, impacting the determination of post-hooking lifetime. Taking into account daily variations in pressure, the number of cycles until failure is 22421 days.

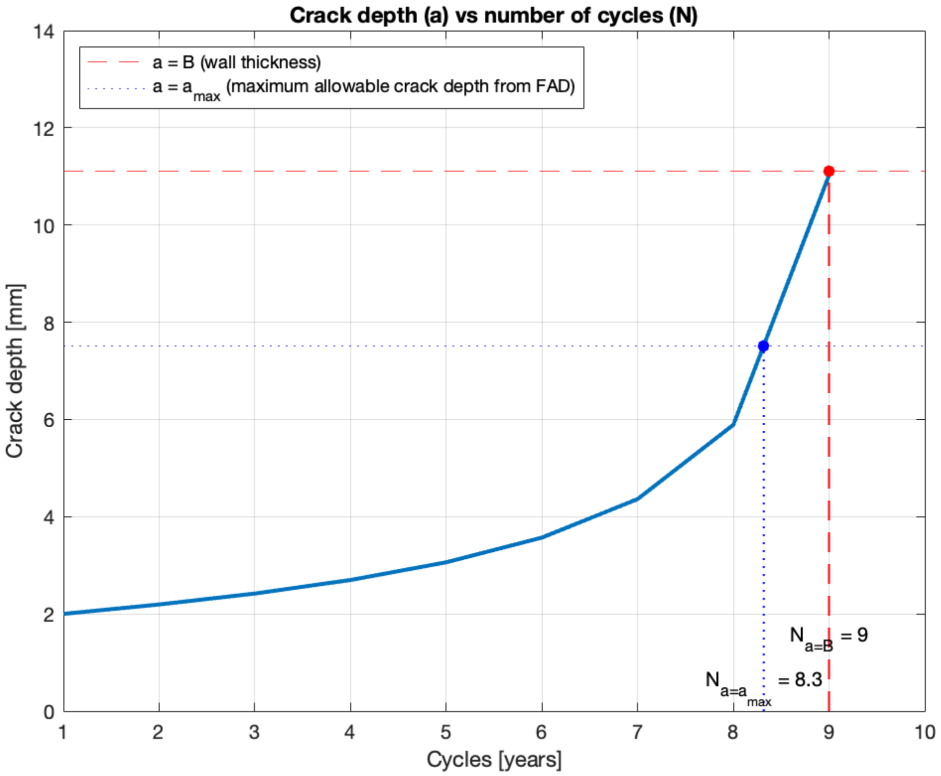

Figure 6.8: The crack growth curve with criteria for the maximum allowable crack depth, impacting the determination of post-hooking lifetime. Taking into account yearly variations in pressure, the number of cycles until failure is approximately 8 years.

7

Discussion and recommendations

7.1. Relevance

Hydrogen is expected to play a significant role in the global shift away from fossil fuels as the primary source of energy. In the near future, significant investments are expected to be made in hydrogen infrastructure, leading to the expansion of the current hydrogen pipeline network. Transportation of hydrogen by pipelines, in conjunction with wind energy generated offshore (or onshore), offers an interesting energy-storage opportunity. Currently, excess renewable electricity goes to waste when there is an oversupply on the grid. Hydrogen gas can be stored and, during periods of high energy demand, converted back into water to release electricity. This process enables efficient energy storage and utilisation, contributing to the overall viability of hydrogen as an energy solution [73].

Through a comprehensive review of existing literature, it has become evident that exisitng offshore pipeline infrastructure is susceptible to damage caused by anchor incidents and intentional sabotage, posing significant financial and environmental risks. Such risks include safety concerns, environmental impact from leakage, and costly repair operations leading to operational downtime and financial losses. Considering the increasing focus on reducing greenhouse gas emissions and the expected expansion of offshore hydrogen infrastructure, the significant risks to these pipelines should be evaluated. Comparing oil and gas pipelines with hydrogen pipelines reveals the following differences. While anchor hooking of oil pipelines poses significant risks to the environment and marine ecosystems, the presence of hydrogen introduces additional challenges compared to oil pipelines. Hydrogen has the potential to accelerate fatigue of the pipeline material and increase its brittleness, reducing the operational lifespan of a pipeline after an anchor hooking incident. Timely detection of damage is crucial to prevent further integrity issues, as it can result in pipeline failure and subsequent shutdown. The resulting downtime leads to substantial production and revenue losses.

Understanding the effects of anchor hooking on the operational life of hydrogen pipelines is crucial for ensuring their safe and reliable operation. Detecting anchor hooking incidents in a pipeline typically involves a combination of methods and technologies aimed at identifying signs of damage or potential risks. Once the damaged section of the pipeline is located, repairs or replacements can be carried out. Repairing a pipeline after an anchor hooking incident is a complex and costly operation. The necessity of (immediate) repair depends on the extent of the damage imposed on the pipeline. A small crack located near the impact point of the anchor on the pipeline can initiate or grow due to the anchor-pipeline interaction. Therefore, it is crucial to gain insight into the expected lifetime of a pipeline following an incident, enabling informed decision-making regarding repair actions based on a comprehensive understanding of the impact's consequences. This study contributes to this topic by providing valuable insights into the behaviour of hydrogen pipelines when subjected to anchor hooking. Anchor hooking leads to elevated stress levels within the pipeline material, potentially causing structural damage that significantly impacts the operational lifespan of the pipeline. By providing insights into the degradation processes and contributing to the development of targeted repair and maintenance strategies, it contributes to the broader goal of realising an efficient hydrogen infrastructure for a clean energy future.

7.2. Limitations

The present research has certain limitations that should be acknowledged. Firstly, it should be emphasised that the focus on a single anchor geometry and pipeline configuration in the research has implications for answering the main research question regarding the post-hooking lifetime of hydrogen pipelines damaged by anchors. Since the conclusions are based on a specific scenario, they provide insights into the behaviour and response of hydrogen pipelines under those particular conditions. The specific characteristics and behaviour of different anchor types and pipeline designs may lead to variations in the outcomes.

Next, three important limitations associated with fatigue crack growth are discussed. It is important to note that the fatigue crack growth analysis is based on an existing crack that has been selected considering workmanship considerations. This means that the analysis does not include fatigue crack growth that might have occurred between installation and damage. Also, this analysis does not account for any crack that could have been initiated during the hooking incident. Taking into account the potential fatigue crack growth during the pipeline's service life would result in an increased crack length compared to considering only the assumed crack at the time of the anchor incident. This extended crack length influences the stress intensity factor and the crack propagation rate. This would eventually result in a different estimation of the remaining fatigue life of the pipeline. Similarly, if the initiation of cracks from the hooking incident is considered, the effects would be comparable since the incident could have initiated a larger crack size compared to the assumed crack depth. Thirdly, the crack development in the study is restricted to one direction, specifically focusing on the critical size of crack depth. The impact of crack length and its influence on the growth of crack depth is not taken into account. Considering both the length and depth of a crack allows for a more comprehensive understanding of crack growth behaviour and its influence on the structural integrity of the material. It enables a more accurate assessment of the stress distribution and the driving force for crack growth.

Lastly, three relevant limitations related to the anchor-pipeline interaction are identified. Firstly, the analysis solely focuses on the interaction between the anchor and pipeline, disregarding the potential influence of soil. The soil surrounding a buried pipeline provides resistance to its movement. Frictional forces between the soil and pipeline contribute to its stability and help to prevent lateral or axial movement. The absence of these factors may result in conservative results, as the real-life conditions involving these elements could affect the crack growth and overall behaviour of the system. The free body diagram in Figure 7.1 illustrates the pipeline and the forces applied to it. These forces include tension near and far from the contact point, and a force due to soil pressure. The y-direction is defined in the direction of trawl, following the motion of the anchor.

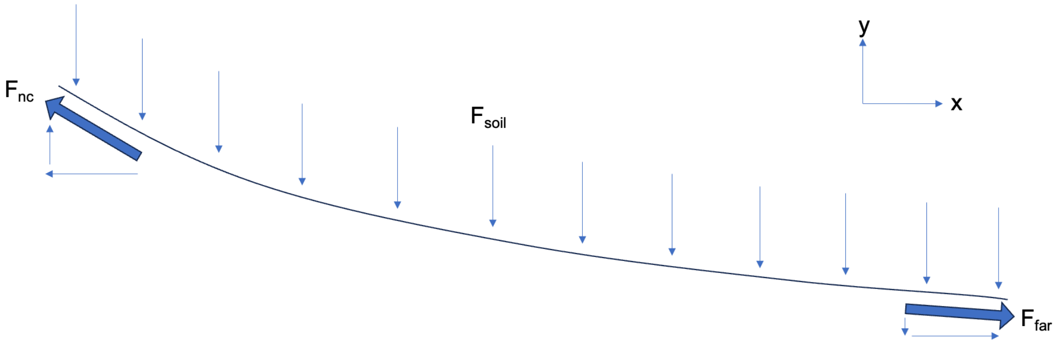

Figure 7.1: Free body diagram of the forces applied to the pipeline.

The sum of forces acting on the pipeline is balanced and equals zero when the system is in equilibrium. Equation 7.1 illustrates the sum of forces in the y-direction.

$$\sum F_y = 0 = F_{nc,y} + F_{soil,y} + F_{far,y} \tag{7.1}$$

Next, the simulation does not account for the snap-back effect when the pipeline is released, which would result in the pipeline slightly moving back from its stretched position. The snap-back motion induces changes in the strain distribution along the pipeline. Areas that were under tension during the hooking incident may experience a release of strain, while other sections of the pipeline may experience increased strain due to the sudden change in forces and deformation. The redistribution of strains leads to changes in stress distribution within the pipeline. As part of the ANSYS simulations, the stress distributions after an anchor hooking incident are analysed. However, if the snap-back effects were taken into account, the resulting stress distribution could be different. For example, in areas where strains are reduced during the snap-back motion, the stress levels may decrease as a consequence. Thirdly, the maximum reaction force reported in ANSYS was used to determine the end point of the simulation, rather than the limiting anchor force defined in Section 4.2.3. In practice, the pipeline could be able to withstand a higher force. This can lead to an increase in stress levels within the pipeline, which in turn can result in an increased crack growth rate. The implication is that the pipeline may reach its maximum allowable crack size sooner, reducing its post-hooking lifetime compared to the results presented in this study. Thus, the obtained results may represent a more optimistic estimate of the actual post-hooking lifetime.

7.3. Recommendations for future research

Based on the findings of the research, several recommendations are proposed for future research, further enhancing the understanding of the effects of anchor hooking incidents on hydrogen pipelines. In the short term, it is worthwhile to explore the influence of pipeline wall thickness on the post-hooking lifetime. Both the ANSYS anchor-pipeline model and the fatigue crack growth model in Matlab can be readily adjusted to accommodate different wall thicknesses. This insight on the relationship between the wall thickness and the post-hooking lifetime contributes to making informed design desisions on pipeline dimensions.

The second recommendation considers the implementation of a soil model in ANSYS. The incident reviewed in this thesis originally concerned a buried pipeline. Soil behavior and interaction with the pipeline influence its deformation and resistance to external forces, playing a crucial role in the structural response and integrity of the material. The resistance to the motion of a buried pipeline is a complex interaction, and is influenced by the properties of the soil, the size and shape of the pipeline, and the speed of motion. Therefore, it is suggested that further research should focus on improving the consideration of soil effects in the ANSYS simulation. A practical manner to implement soil in the existing model, is to use springs. The springs can be modeled using the COMBIN39 command, which is used to define contact properties between different surfaces in Ansys. It does this by modeling the contact behaviour between two surfaces as a series of nonlinear springs. This model can be built upon the theory on pipe-soil interaction for submarine pipeline described in DNV-RP-F114 [74].

Recommended steps for future research also consider looking into pipelines carrying different substances and examine the impact of damage caused by different relevant external factors. The analytical framework developed in this study could be applied to analyse pipelines transporting alternative gases or liquids that contribute to the realisation of renewable energy targets. Of particular interest is the transportation of liquid ammonia, which serves as an energy storage solution and addresses challenges related to excessive power grid consumption [75] [76] [77]. A future study on ammonia pipelines can be readily conducted as the ANSYS and Matlab models used in this study can be easily modified. However, it is important to note that the characteristic behaviour of the pipeline under investigation would need to be revised, considering that the application of the Paris law, implemented in this study, is not directly applicable to liquids like ammonia. Despite this limitation, conducting a comparative study involving pipelines transporting different types of gases or liquids would provide valuable insights for making informed (design) decisions regarding the transportation of renewable energy. The second recommendation suggests to evaluate different relevant external factors, which can cause damage to pipelines. The recent incidents involving leaks in the Nord Stream pipelines have raised questions about the motives and potential impacts of pipeline sabotage. The Nord Stream pipelines represent critical infrastructure for European energy security and the attack is considered as intentional sabotage. This deliberate attack not only highlights the vulnerabilities of critical energy infrastructure, because energy supplies have been disrupted, but also carries wider geopolitical implications. The leaks in the Nord Stream gas pipelines serve as a reminder of the need to address the security and vulnerability issues associated with critical energy infrastructure, and to implement strengthened protective measures [78]. Further research exploring the impact of potential sabotage can contribute to the development and implementation of appropriate security measures.

8

Conclusion

With the growing focus on reducing greenhouse gas emissions, the transportation of hydrogen through offshore pipelines has emerged as an appealing solution. However, the risks of anchor damage to these pipelines pose a significant concern in offshore pipeline technology. As offshore energy production expands and its transport via offshore pipelines increases, there is a notable risk that future hydrogen pipelines may be susceptible to anchor damage. The presence of hydrogen accelerates fatigue of the pipeline material and increase its brittleness, which affects the operational life of the pipeline. The primary objective of this research has been to determine the post-hooking lifetime of hydrogen pipelines damaged by anchors. The main research question was defined as follows:

"What is the post-hooking lifetime of a hydrogen pipeline damaged by an anchor?"

The following sub-questions are introduced to answer the main research question:

1. What is the resulting stress distribution and variation within the pipeline material after an anchor hooking incident?
2. How is the rate of fatigue crack growth in an anchor hooking problem affected in the presence of hydrogen?
3. When does the crack reach a critical depth, possibly leading to pipeline failure?

In this study, the rate of fatigue crack growth was evaluated using the commonly adopted Paris law. The analysis aimed to investigate factors that influence the application of the Paris law, addressing the first two sub-questions. Initially, the study focused on answering the first sub-question, which analyses the stress distribution within the material resulting from anchor impact. To accomplish this, numerical simulations were performed using ANSYS software, specifically examining the interaction between the anchor and the pipeline. By conducting these simulations, it was possible to assess the variations in membrane and bending stress due to changes in pressure, which directly influence the rate of fatigue crack growth.

The second sub-question specifically focuses on investigating the impact of hydrogen on the rate of fatigue crack growth. It is important to consider the influence of hydrogen on the behaviour of the Paris law, as its presence introduces additional complexities to the analysis. When hydrogen is present, an increased diffusion of hydrogen towards the crack tip occurs, leading to an accelerated rate of fatigue crack growth. In the presence of hydrogen, the Paris regime exhibits a three-stage relationship. The specific relationship and the values assigned to the material constants in the Paris law are derived from ASME B31.12-2019 [19].

The third objective of this study involves the utilisation of Matlab to analyse the crack growth curve. The crack growth curve represents the relationship between the depth of the crack and the corresponding number of cyclic loading cycles. The stress variations derived from the ANSYS simulation, in combination with the understanding of the behaviour of the Paris law, play a crucial role in establishing the crack growth curve. Two critical crack depths leading to failure are considered in this analysis. The first assumes a crack that extends completely through the thickness of the component, while the second represents a crucial point on the crack growth curve, as determined by the Failure Assessment Diagram (FAD). The FAD helps to determine the maximum allowable crack size that ensures the safety of the structure. Once the crack reaches the depth specified by the FAD, it indicates that the crack has grown to a critical size that poses a significant risk to the structural integrity of the component. If the crack is through-thickness or has reached a critical depth that exceeds the limits specified by the FAD, immediate failure of the component becomes a significant concern.

Finally, the primary research question can be addressed: *”What is the post-hooking lifetime of a hydrogen pipeline damaged by an anchor?”*. This study focuses on a hydrogen pipeline that sustains damage due to an anchor dragging incident. Despite the impact, the pipeline continues to operate under normal conditions. However, the presence of deformation from the impact amplifies the stress changes, which can have an impact on fatigue crack growth. The stress variations induced by the anchor impact contribute to the initiation and propagation of fatigue cracks within the pipeline material. As the crack depth progresses, the crack reaches a critical depth, potentially resulting in failure. The number of cycles required for the crack to reach this critical depth can be determined through a crack growth curve, which represents the relationship between crack depth and the corresponding number of cycles. The analysis takes daily and yearly variations in pressure into account. For daily variations in pressure, the crack reaches a critical depth after 22421 days. Although the attained crack depth is not yet through-thickness, the crack growth rate increase significantly after 22421 days, and a through-thickness crack is reached 22632 days after impact. Considering yearly variations in pressure, the crack reaches a critical depth after a little over 8 years. The post-hooking lifetime for daily variations in pressure exceeds the maximum number of cycles obtained from analysing the yearly variations in pressure. Therefore, the post-hooking lifetime of a hydrogen pipeline damaged by an anchor is approximately 8 years.

Based on the aforementioned conclusions, there are two important observations that need to be considered. First of all, the presented conclusions apply only to a specific anchor geometry and pipeline configuration used as a case study. The findings of this research may not be directly applicable to various anchor geometries and pipeline designs due to the limited scope of this investigation. The anchor geometry and pipeline design can influence the distribution of stresses along the pipeline, which influences the stress intensity factor and consequently the post-hooking lifetime. Also, the fatigue crack growth analysis examines an existing crack depth, which has been selected based on workmanship considerations. The analysis does not take into account any fatigue crack growth that might have occurred between installation and anchor damage, and it also does not consider any cracks that might have been initiated during the hooking incident. Considering the influences on the crack development could potentially result in a longer crack depth, affecting the stress intensity factor and propagation rate, leading to a different estimation of the remaining fatigue life. A crack depth sensitivity analysis is suggested to study how the crack depth affects the material’s post-hooking lifetime. Secondly, the outcomes of this research have several limitations that should be acknowledged, which means that the presented results cannot be considered as a definitive assessment for this case study. Relevant limitations concern the design decisions regarding anchor-pipeline interaction. The analysis is part of a case study, which considers a buried pipeline. However, the potential influence of soil is neglected, and the analysis solely focuses on the interaction between the anchor and the pipeline. Also, the simulation does not account for the snap-back effect when the pipeline is released, causing it to slightly move back from its stretched position. This snap-back motion leads to changes in strain distribution along the pipeline. These strain redistributions cause changes in stress distribution within the pipeline. Taking the snap-back effects into account could result in different stress distributions, with potential stress level reductions in areas where strains are reduced during the snap-back motion. Chapter 7 extensively covers the limitations and recommendations for this research.

The fatigue crack growth resulting from anchor impact can potentially lead to pipeline leakage if not detected in a timely manner. Such a scenario could result in risks to the safety of marine life and people, and substantial economic losses are usually involved. Understanding the post-hooking lifetime and crack behaviour is invaluable for pipeline operators, enabling them to determine the appropriate interval for maintenance activities following an impact. Balancing the economic factors in the decision-making process for pipeline repairs post-impact involves avoiding excessive and unnecessary maintenance activities. However, it is equally important to ensure that safety and environmental requirements are met. The outcomes of this study contribute to gaining valuable knowledge concerning the vulnerability of hydrogen pipelines and can be used in relevant discussions on establishing a hydrogen economy.

A

Anchor and pipeline properties numerical simulations

This appendix provides a detailed explanation of the parameters utilised in the numerical simulation within ANSYS. These parameters encompass the specifications of the anchor and pipeline, essential for accurately representing their behavior and interaction.

A.1. Pressure parameters

Table A.1 contains the parameters and values used to determine the internal pressure of the pipeline in the numerical simulations within ANSYS.

Table A.1: Model parameters to define pressure inside the pipeline.

Parameter	Symbol	Value	Unit	Description
Gravitational acceleration	g	9.81	m/s^2	Gravitational constant used to determine hydrostatic pressure
Atmospheric pressure	p_{atm}	101	kPa	Pressure of the atmosphere above sea level
Hydrostatic pressure	p_e	367	kPa	Hydrostatic pressure at 36.5 m
Gauge pressure	p_g	3532	kPa	Pressure applied to the pipeline, difference between internal and external pressure
Design pressure	p_i	4000	kPa	Internal pressure in pipeline
Seawater density	ρ_{sw}	1025	kgm^{-3}	Density of the seawater/ North Sea

A.2. Pipeline parameters

Table A.2 contains the parameters and values for the pipeline used in the numerical simulations within ANSYS.

Table A.2 also contains parameters to determine bilinear isotropic hardening to describe the behaviour of a material under plastic deformation. To describe the stress-strain relationship of a material, two parameters are defined: the yield strength (σ_y) and the tangent modulus (E_t). The second parameter refers to the slope of the stress-strain curve during the plastic deformation phase. It represents the rate at which the stress increases with respect to the strain.

Table A.2: Pipeline parameters and values.

Parameter	Symbol	Value	Unit	Description
Outside diameter	D_o	219.1	mm	The measurement of the diameter of the pipe from the outermost edge on one side of the pipe, through the center, to the outermost edge on the opposite side
Young's modulus	E	194 [79]	GPa	Measure of the elasticity of a material
Tangent modulus	E_t	10	MPa	The slope of the stress-strain curve
Beam length	L_b	16.5	m	Length of the beam attached to the solid pipeline
Solid pipeline length	L_s	3.5	m	Lenght of the pipeline section as used in the numerical simulation
Poisson's ratio	ν	0.3	$[-]$	Measure of the Poisson effect
Internal radius	r_i	98.45	mm	Distance from the center of a circular pipe to its inner surface
Outer radius	r_o	109.55	mm	Distance from the center of a circular pipe to its outer surface
Density steel	ρ	7850	kgm^{-3}	Mass per unit of volume
Tensile ultimate strength (UTS)	σ_u	460	MPa	The maximum value of the stress that a material is capable to bear or withstand
Tensile yield strength	σ_Y	360	MPa	The maximum stress that a material can withstand before it begins to deform plastically under tension
Wall thickness	t	11.1	mm	Distance between internal and outer radius of the pipeline

A.3. Anchor parameters

Table A.3 contains the parameters and values for the anchor used in the numerical simulations within ANSYS.

Table A.3: Anchor parameters and values [20].

Parameter	Symbol	Value	Unit	Description
Young's modulus	E	200	GPa	Measure of the elasticity of a material
Anchor mass	m	2300	kg	Mass of the anchor that was found next to the damaged pipeline
Poisson's ratio	ν	0.3	$[-]$	Measure of the Poisson effect
Density	ρ	7850	kgm^{-3}	Mass per unit of volume
Compressive yield strength	$\sigma_{Y,c}$	250	MPa	The maximum stress that a material can withstand before it begins to deform plastically under compression

B

Crack growth model properties

This appendix provides an in-depth exploration of the properties utilised in the crack growth model, which plays a crucial role in understanding the behavior of a crack in the pipeline structure. This appendix presents the specific parameters applied in the crack growth model and offers a detailed explanation of the equations used to determine the stress intensity magnification factor. By providing these valuable insights, the appendix enhances the overall understanding of the crack growth analysis and its implications for the integrity assessment of the pipeline.

B.1. Crack growth model parameters

To create a crack growth model, some information about the size of the crack, the threshold value, and other related factors is required. The empirical solutions needed to compute crack propagation are presented in $BS7910 : 2013$ and have been discussed in detail in Section 5.1. A complete overview of the parameters and corresponding values taken into account during the fatigue crack growth analysis is given in Table B.1 below. The values to the material constants of the Paris law used in this model have been defined earlier in Chapter 5 and can be found in Table 5.1.

In Section 5.1.4, the stress intensity magnification factors M_m, M_b, M_{km}, and M_{kb} were introduced, with the last two factors considering the presence of the weld. The calculation of M_m and M_b relies on the ratios of a/B, a/c, and B/r_i, while M_{km} and M_{kb} are determined based on the ratios of a/B, a/c, and L/B. When calculating the a/B ratio, it is important to consider the increasing crack depth in the analysis. Based on fatigue striations, the a/c ratio is assumed to remain constant throughout the fatigue crack growth process, and calculated according to the initial crack depth a_0 and half the initial crack length c_0. Also, the B/r_i and L/B ratios remain constant. Based on the values provided in Table B.1, the corresponding ratios can be calculated as follows:

$$\begin{aligned} a_0/c_0 &= 0.2667 \\ B/r_i &= 0.1127 \\ L/B &= 0.7207 \end{aligned}$$

$BS7910 : 2013$ does not directly provide specific values for M_m and M_b corresponding to the above defined ratios. The values for M_m and M_b are obtained through two stages of interpolation. Firstly, interpolation is performed to determine the values corresponding to the a/B ratio for the a_0/c_0 values presented in $BS7910 : 2013$. Subsequently, these interpolated values are further interpolated to obtain the appropriate values corresponding to the specific a_0/c_0 ratio. The calculation of M_{km} and M_{kb} is explained in Section B.2.

Table B.1: Parameters used in the crack growth model. The stress intensity magnification factors at the deepest and surface points are respectively denoted by (d) and (s).

Parameter	**Symbol**	**Value**	**Unit**	**Description**
Initial crack depth	a_0	2	mm	Initial flaw depth for surface flaw
Wall thickness	B	11.1	mm	Section thickness in plane of flaw
Crack length	c_0	7.5	mm	Initial half flaw length for surface or embedded flaws
Young's modulus	E	194 [79]	GPa	Measure of the elasticity of a material
Correction factor	f_w	1	[-]	Factor accounting for finite width effect and the stress concentrating effect of the hole
Plane strain fracture toughness	K_{Ic}	1737 [19]	$N/mm^{\frac{3}{2}}$	The critical value of stress intensity factor required to propagate a pre-existing crack
Threshold value	ΔK_{th}	200	$N/mm^{\frac{3}{2}}$	The minimum value of the stress intensity factor range below which a fatigue crack will not grow
Cycle step size	ΔN	1	[-]	Number of cycles between iterations
Stress magnification factor	k_m	1.0182	[-]	Stress magnification factor due to misalignment
Bending stress concentration factor	k_{tb}	1	[-]	The increase in stress at a specific location in a structure, compared to the nominal or average stress in the surrounding region.
Membrane stress concentration factor	k_{tm}	1	[-]	See description for k_{tb}
Attachment length	L	8	mm	The overall length of the attachment, measured from one weld toe to the other
Bulging correction factor	M	1	[-]	Correction factor for the stress intensity factor calculation
Internal radius	r_i	98.45	mm	Distance from the center of a circular pipe to its inner surface
Tensile ultimate strength (UTS)	σ_u	460	MPa	The maximum value of the stress that a material is capable to bear or withstand
Tensile yield strength	σ_Y	360	MPa	The maximum stress that a material can withstand before it begins to deform plastically under tension

B.2. Stress intensity magnification factor

In this section of the appendix, a detailed overview of the supporting formulas to calculate the stress intensity magnification factors is provided. The definitions for the stress intensity factors for membrane and bending stress have been introduced in Section 5.1.4. The definitions presented in this section follow from $BS7910:2013$ [17].

To calculate g_1 to g_8 for the membrane stress intensity magnification factor and g_1 to g_9 for the bending stress intensity magnification factor, three ratios are introduced. The a/c ratio is dependent on the crack dimensions, which are the crack depth (a) and the crack length (c). The L/B ratio is dependent on the weld dimensions, which have been explained in Section 5.1.4. The a/B ratio is dependent on the increasing crack depth and the wall thickness (B). The equations for the parameters g_1 to g_8 for membrane stress and g_1 to g_9 for bending stress follow from analyses by Bowness and Lee [80]. This study builds upon previous research by evaluating existing sets of M_k solutions and proposing improved equations for weld toe magnification factors. The investigation involves three-dimensional finite element analysis of weld toe cracks in T-butt joints. The study provides more accurate and reliable predictions of M_k factors for T-butt welds. The results of this study have been adopted by $BS7910:2013$ to examine surface cracks at weld toes.

B.2.1. Membrane stress

The stress intensity magnification factor for the deepest point, which accounts for membrane stresses, is calculated as follows:

$$M_{km} = f_1\left(\frac{a}{B},\frac{a}{c}\right) + f_2\left(\frac{a}{B}\right) + f_3\left(\frac{a}{B},\frac{L}{B}\right) \tag{B.1}$$

$$f_1\left(\frac{a}{B},\frac{a}{c}\right) = 0.43358\left(\frac{a}{B}\right)\left(g_1 + \left[g_2\left(\frac{a}{B}\right)^{g_3}\right]\right) + 0.93163e^{\left[\left(\frac{a}{B}\right)^{-0.050966}\right]} + g_4 \tag{B.2}$$

$$f_2\left(\frac{a}{B}\right) = -0.21521\left[1-\left(\frac{a}{B}\right)\right]^{176.4199} + 2.8141\left(\frac{a}{B}\right)^{-0.10740\left(\frac{a}{B}\right)} \tag{B.3}$$

$$f_3\left(\frac{a}{B},\frac{L}{B}\right) = 0.33994\left(\frac{a}{B}\right)^{g_5} + 1.9493\left(\frac{a}{B}\right)^{0.23003} + \left[g_6\left(\frac{a}{B}\right)^2 + g_7\left(\frac{a}{B}\right) + g_8\right] \tag{B.4}$$

The above presented equations are the same as in Chapter 5. The parameters g_1 through g_8 are properly introduced below:

$$g_1 = -1.0343\left(\frac{a}{c}\right)^2 - 0.15657\left(\frac{a}{c}\right) + 1.3409 \tag{B.5}$$

$$g_2 = 1.3218\left(\frac{a}{c}\right)^{-0.61153} \tag{B.6}$$

$$g_3 = -0.87238\left(\frac{a}{c}\right) + 1.2788 \tag{B.7}$$

$$g_4 = -0.46190\left(\frac{a}{c}\right)^3 - 0.67090\left(\frac{a}{c}\right)^2 - 0.37571\left(\frac{a}{c}\right) + 4.6511 \tag{B.8}$$

$$g_5 = -0.015647\left(\frac{L}{B}\right)^3 + 0.090889\left(\frac{L}{B}\right)^2 - 0.17180\left(\frac{L}{B}\right) - 0.24587 \tag{B.9}$$

$$g_6 = -0.20136\left(\frac{L}{B}\right)^2 + 0.93311\left(\frac{L}{B}\right) - 0.41496 \tag{B.10}$$

$$g_7 = 0.20188\left(\frac{L}{B}\right)^2 - 0.97857\left(\frac{L}{B}\right) + 0.068225 \tag{B.11}$$

$$g_8 = -0.027338\left(\frac{L}{B}\right)^2 + 0.12551\left(\frac{L}{B}\right) - 11.218 \tag{B.12}$$

B.2.2. Bending stress

The stress intensity magnification factor for the deepest point, which accounts for bending stresses, is calculated as follows:

$$M_{kb} = f_1\left(\frac{a}{B}, \frac{a}{c}\right) + f_2\left(\frac{a}{B}\right) + f_3\left(\frac{a}{B}, \frac{L}{B}\right) \tag{B.13}$$

$$f_1\left(\frac{a}{B}, \frac{a}{c}\right) = 0.065916\left(\frac{a}{B}\right)^{g_1 + \left[g_2\left(\frac{a}{B}\right)^{g_3}\right]} + 0.52086e^{\left[\left(\frac{a}{B}\right)^{-0.10364}\right]} + g_4 \tag{B.14}$$

$$f_2\left(\frac{a}{B}\right) = -0.02195\left[1 - \left(\frac{a}{B}\right)\right]^{2.8086} + 0.021403\left(\frac{a}{B}\right)^{g_5} \tag{B.15}$$

$$f_3\left(\frac{a}{B}, \frac{L}{B}\right) = 0.23344\left(\frac{a}{B}\right)^{g_6} - 0.14827\left(\frac{a}{B}\right)^{0.20077} + \left[g_7\left(\frac{a}{B}\right)^2 + g_8\left(\frac{a}{B}\right) + g_9\right] \tag{B.16}$$

The above presented equations are the same as in Chapter 5. The parameters g_1 through g_9 are properly introduced below:

$$g_1 = -0.014992\left(\frac{a}{c}\right)^2 - 0.021401\left(\frac{a}{c}\right) - 0.23851 \tag{B.17}$$

$$g_2 = 0.61775\left(\frac{a}{c}\right)^{-1.0278} \tag{B.18}$$

$$g_3 = 0.00013242\left(\frac{a}{c}\right) - 1.4744 \tag{B.19}$$

$$g_4 = -0.28783\left(\frac{a}{c}\right)^3 + 0.58706\left(\frac{a}{c}\right)^2 - 0.37198\left(\frac{a}{c}\right) - 0.89887 \tag{B.20}$$

$$g_5 = -17.195\left(\frac{a}{c}\right) + 12.468\left(\frac{a}{c}\right) - 0.51662 \tag{B.21}$$

$$g_6 = -0.059798\left(\frac{L}{B}\right)^3 + 0.38091\left(\frac{L}{B}\right)^2 - 0.8022037\left(\frac{L}{B}\right) + 0.31906 \tag{B.22}$$

$$g_7 = -0.35848\left(\frac{L}{B}\right)^2 + 1.3975\left(\frac{L}{B}\right) - 1.7535 \tag{B.23}$$

$$g_8 = 0.31288\left(\frac{L}{B}\right)^2 - 1.3599\left(\frac{L}{B}\right) + 1.6611 \tag{B.24}$$

$$g_9 = -0.001470\left(\frac{L}{B}\right)^2 - 0.0025074\left(\frac{L}{B}\right) - 0.0089846 \tag{B.25}$$

Bibliography

[1] "Anchor Images ." [Online]. Available: https://stock.adobe.com/search?k=anchor

[2] International Energy Agency, "Energy Technology Perspectives 2023," 2023.

[3] E. Gjertveit, "Kvitebjørn gas pipeline repair." Bergen, Norway: Underwater Technology Conference, 9 2010.

[4] Y. Liu, H. Hu, and D. Zhang, "Probability Analysis of Damage to Offshore Pipeline by Ship Factors," *Transportation Research Record: Journal of the Transportation Research*, vol. 2326, pp. 24–31, 2013.

[5] R. Orsolato, S. Fabbri, and P. Cherubini, "Transmediterranean Pipelines Repair." Ravenna, Italy: 10th Offshore Mediterranean Conference and Exhibition, 3 2011.

[6] "Line 5 in the Straits of Mackinac." [Online]. Available: https://forloveofwater.org/line5/

[7] M. Kristoffersen, T. Børvik, M. L. Odd, S. Hopperstad, H. Avar Ilstad, and E. Levold, "Damage and failure resulting from trawl gear impact in an X65 steel pipeline," in *Proceedings of the ASME 2013 32nd International Conference on Ocean, Offshore and Arctic Engineering*. Nantes, France: OMAE2013, 6 2013.

[8] M. Kristoffersen, T. Børvik, I. Westermann, M. Langseth, and O. S. Hopperstad, "Impact against X65 steel pipes - An experimental investigation," *International Journal of Solids and Structures*, vol. 50, no. 20-21, pp. 3430–3445, 10 2013.

[9] S. R. Hauch and Y. Bai, "Bending Moment Capacity of Pipes," *Journal of Offshore Mechanics and Arctic Engineering*, vol. 122, pp. 243–252, 11 2000.

[10] Det Norske Veritas (DNV), "DNV-RP-F111 Interference Between Trawl Gear and Pipelines," 2010.

[11] A. Turnbull, "Hydrogen diffusion and trapping in metals," in *Gaseous Hydrogen Embrittlement of Materials in Energy Technologies: Mechanisms, Modelling and Future Developments*, R. Gangloff and B. Somerday, Eds. Woodhead Publishing, 2012, vol. 2, ch. 4, pp. 89–128.

[12] M. Grasso, A. De Iorio, Y. Xu, G. Haritos, M. Mohin, and Y. K. Chen, "An analytical model for the identification of the threshold of stress intensity factor range for crack growth," *Advances in Materials Science and Engineering*, vol. 2017, 1 2017.

[13] R. Wei and G. Simmons, "Environment Enhanced Fatigue Crack Growth in High-Strength Steels," Office of Naval Research, Bethlehem, Pennsylvania, Tech. Rep., 3 1973.

[14] N. E. Nanninga, Y. S. Levy, E. S. Drexler, R. T. Condon, A. E. Stevenson, and A. J. Slifka, "Comparison of hydrogen embrittlement in three pipeline steels in high pressure gaseous hydrogen environments," *Corrosion Science*, vol. 59, 2 2012.

[15] N. Dowling and J. Begley, "Fatigue Crack Growth During Gross Plasticity and the J-Integral," in *Mechanics of Crack Growth, Proceedings of the Eighth National Symposium on Fracture Mechanics*. American Society for Testing and Materials, 1976, pp. 82–103.

[16] K. A. Nibur and B. P. Somerday, "Fracture and fatigue test methods in hydrogen gas," in *Gaseous Hydrogen Embrittlement of Materials in Energy Technologies: The Problem, its Characterisation and Effects on Particular Alloy Classes*. Woodhead Publishing, 2012, vol. 2, pp. 195–236.

[17] British Standards Institution, *BS 7910:2013 Guide to methods for assessing the acceptability of flaws in metallic structures.*, 3rd ed. British Standards Institution, 12 2013.

[18] A. Staroselsky, “Damage and cracking morphology,” *Advances in Fatigue, Fracture and Damage Assessment of Materials*, pp. 15–53, 9 2005. [Online]. Available: https://www.researchgate.net/publication/232726254_Damage_and_Cracking_Morphology

[19] The American Society of Mechanical Engineers, *B31.12-2019: Hydrogen Piping and Pipelines*, 2019.

[20] “AC-14 H.H.P Anchor | 3D CAD Model Library | GrabCAD.” [Online]. Available: https://grabcad.com/library/ac-14-h-h-p-anchor-1

[21] Det Norske Veritas (DNV), “DNVGL-RU-INV Pt.3 Ch.6.” 2021.

[22] European Commission, “A European Green Deal,” 2020. [Online]. Available: https://ec.europa.eu/info/strategy/priorities-2019-2024/european-green-deal_en

[23] “Offshore renewable energy.” [Online]. Available: https://energy.ec.europa.eu/topics/renewable-energy/offshore-renewable-energy_en

[24] “Pipeline for green hydrogen from North Sea.” [Online]. Available: https://www.rwe.com/en/press/rwe-renewables/2021-04-26-aquaductus-pipeline-for-green-hydrogen-gascade-gasunie-rwe-shell/

[25] “The Netherlands Chooses Site for World’s Largest Offshore Wind-to-Hydrogen Project | Offshore Wind.” [Online]. Available: https://www.offshorewind.biz/2023/03/20/the-netherlands-chooses-site-for-worlds-largest-offshore-wind-to-hydrogen-project/

[26] “Offshore hydrogen production enables far-offshore wind deployment.” [Online]. Available: https://hydrogentechworld.com/offshore-hydrogen-production-enables-far-offshore-wind-deployment

[27] “Small gas leak from Kvitebjørn pipeline,” 8 2008. [Online]. Available: https://www.equinor.com/news/archive/2008/08/20/gasleakkvitebjorn

[28] “Production resumed at Kvitebjørn,” 1 2009. [Online]. Available: https://www.equinor.com/news/archive/2009/01/27/27JanKvitebjoern

[29] “Transportation of hydrogen gas in offshore pipelines: H2Pipe.” [Online]. Available: https://www.dnv.com/article/transportation-of-hydrogen-gas-in-offshore-pipelines-h2pipe-213006

[30] M. Sand, R. B. Skeie, M. Sandstad, S. Krishnan, G. Myhre, H. Bryant, R. Derwent, D. Hauglustaine, F. Paulot, M. Prather, and D. Stevenson, “A multi-model assessment of the Global Warming Potential of hydrogen,” *Communications Earth & Environment 2023 4:1*, vol. 4, no. 1, pp. 1–12, 6 2023. [Online]. Available: https://www.nature.com/articles/s43247-023-00857-8

[31] T. Sriskandarajah and R. Wilkins, “Assessment of Anchor Dragging on Gas Pipelines,” in *Proceedings of The Twelfth (2002) International Offshore and Polar Engineering Conference*. Kitakyushu, Japan: The International Society of Offshore and Polar Engineers, 5 2002, pp. 24–31.

[32] E. Amri, N. S. Sulaiman, and F. A. Alaw, “Risk analysis of offshore pipeline due to third party damages,” in *IOP Conference Series: Materials Science and Engineering*, vol. 702, no. 1. IOP Publishing Ltd, 12 2019.

[33] “Offshore California pipeline likely damaged long before spill,” *Offshore*, 10 2021. [Online]. Available: https://www.offshore-mag.com/pipelines/article/14211893/offshore-california-pipeline-likely-damaged-long-before-spill

[34] C. Hvam, R. Bruschi, M. Tominez, and L. Vitali, “Risk of Pipe Damage from Dragging Anchors.” Trondheim, Norway: European Offshore Mechanics Symposium, 8 1990.

[35] A. Di Padova, C. Zuliani, and F. Tallone, “Dragged anchors interaction scenarios: Detailed frequency analysis for pipeline design.” Los Angeles, California: Probabilistic Safety Assessment and Management PSAM 14, 9 2018.

[36] A. AL-Wharthan, J. Chung, H. Huttelmaier, and G. Mustoe, “Effect of Ship Anchor Impact In Offshore Pipeline,” *Proc 3rd Int Offshore and Polar Eng Conf*, vol. 2, pp. 54–61, 6 1993.

[37] T. Sriskandarajah, P. Ragupathy, G. Anurudran, and R. Wilkins, “Fishing Gear Interaction On HP/HT Pipe-in-Pipe Systems,” in *Proceedings of the Ninth (1999) International Offshore and Polar Engineering Conference*. Brest, France: The International Society of Offshore and Polar Engineers, 5 1999, pp. 160–167.

[38] R. Brown, “Pipelines Can Be Designed to Resist Impact From Dragging Anchors and Fishing Boards.” Houston, Texas: Offshore Technology Conference, 4 1972.

[39] Det Norske Veritas (DNV) and Germanischer Lloyd (GL), “DNVGL-ST-F101 Submarine pipeline systems,” 2017.

[40] Det Norske Veritas (DNV), “DNV-RP-F107 Risk Assessment of Pipeline Protection,” 2010.

[41] C. Gaudin, G. Vlahos, and M. Randolph, “Investigation in Centrifuge of Anchor-pipeline Interaction,” *International Journal of Offshore and Polar Engineering*, vol. 17, no. 1, pp. 67–73, 3 2007.

[42] R. Selker, P. Liu, D. Karras, R. Bijker, and O. Aktan, “Impact of Dropped Objects and Anchor Dragging on Pipeline Integrity,” in *Proceedings of the Twenty-eighth (2018) International Ocean and Polar Engineering Conference*. Sapporo, Japan: International Society of Offshore and Polar Engineers, 6 2018, pp. 238–247.

[43] X. Li, X. Ma, J. Zhang, E. Akiyama, Y. Wang, and X. Song, “Review of Hydrogen Embrittlement in Metals: Hydrogen Diffusion, Hydrogen Characterization, Hydrogen Embrittlement Mechanism and Prevention,” *Acta Metallurgica Sinica (English Letters)*, vol. 33, no. 6, pp. 759–773, 6 2020.

[44] Q. Liu and A. Atrens, “A critical review of the influence of hydrogen on the mechanical properties of medium-strength steels,” *Corrosion Reviews*, vol. 31, no. 3-6, pp. 85–103, 12 2013.

[45] A. Trautmann, G. Mori, M. Oberndorfer, S. Bauer, C. Holzer, and C. Dittmann, “Hydrogen Uptake and Embrittlement of Carbon Steels in Various Environments,” *Materials*, vol. 13, no. 16, 8 2020.

[46] A. Sieverts, “The Absorption of Gases by Metals,” *Zeitschrift für Metallkunde*, vol. 21, pp. 37–46, 1929.

[47] N. Arnaudov, “Micromechanical Simulation of Fatigue Crack Initiation under Hydrogen Influence,” Ph.D. dissertation, Materialprufungsanstalt (MPA) Universitat Stuttgart, Stuttgart, Germany, 2021.

[48] R. Fernández-Sousa, C. Betegón, and E. Martínez-Pañeda, “Analysis of the influence of microstructural traps on hydrogen assisted fatigue,” *Acta Materialia*, vol. 199, pp. 253–263, 10 2020.

[49] A. H. Krom, H. J. Maier, R. W. Koers, and A. Bakker, “The effect of strain rate on hydrogen distribution in round tensile specimens,” *Materials Science and Engineering: A*, vol. 271, no. 1-2, pp. 22–30, 11 1999.

[50] H. R. Gray, H. G. Nelson, R. E. Johnson, W. B. McPherson, F. S. Howard, and J. H. Swisher, “Potential structural material problems in a hydrogen energy system,” *International Journal of Hydrogen Energy*, vol. 3, no. 1, pp. 105–118, 1 1978.

[51] T. Boot, T. A. Riemslag, E. T. Reinton, P. Liu, C. L. Walters, and V. Popovich, “In-Situ Hollow Sample Setup Design for Mechanical Characterisation of Gaseous Hydrogen Embrittlement of Pipeline Steels and Welds,” *Metals 2021, Vol. 11, Page 1242*, vol. 11, no. 8, p. 1242, 8 2021.

[52] I. H. Katzarov and A. T. Paxton, “Hydrogen embrittlement II. Analysis of hydrogen-enhanced decohesion across (111) planes in α-Fe,” *PHYSICAL REVIEW MATERIALS*, vol. 1, p. 33603, 2017.

[53] C. D. Beachem, “A new model for hydrogen-assisted cracking (hydrogen “embrittlement”),” *Metallurgical and Materials Transactions B 1972 3:2*, vol. 3, no. 2, pp. 441–455, 2 1972.

[54] I. H. Katzarov, D. L. Pashov, and A. T. Paxton, “Hydrogen embrittlement I. Analysis of hydrogen-enhanced localized plasticity: Effect of hydrogen on the velocity of screw dislocations in α-Fe,” *PHYSICAL REVIEW MATERIALS*, vol. 1, p. 33602, 2017.

[55] I. M. Robertson, “The effect of hydrogen on dislocation dynamics,” *Engineering Fracture Mechanics*, vol. 68, no. 6, pp. 671–692, 4 2001.

[56] M. Nagumo, M. Nakamura, and K. Takai, “Hydrogen Thermal Desorption Relevant to Delayed-Fracture Susceptibility of High-Strength Steels,” *Metallurgical and Materials Transactions A*, vol. 32A, pp. 339–347, 2 2001.

[57] M. Nagumo, “Hydrogen related failure of steels - a new aspect,” *Materials Science and Technology*, vol. 20, no. 8, pp. 940–950, 8 2004.

[58] K. Takai, H. Shoda, H. Suzuki, and M. Nagumo, “Lattice defects dominating hydrogen-related failure of metals,” *Acta Materialia*, vol. 56, no. 18, pp. 5158–5167, 10 2008.

[59] S. P. Lynch, “Hydrogen embrittlement and liquid-metal embrittlement in nickel single crystals,” *Scripta Metallurgica*, vol. 13, no. 11, pp. 1051–1056, 1979.

[60] J. A. Clum, “The role of hydrogen in dislocation generation in iron alloys,” *Scripta Metallurgica*, vol. 9, no. 1, pp. 51–58, 1975.

[61] S. Lynch and S. Lynch, “Some fractographic contributions to understanding fatigue crack growth,” *International Journal of Fatigue*, vol. 104, pp. 12–26, 11 2017.

[62] H. A. Richard and M. Sander, *Fatigue Crack Growth*. Springer, 2016, vol. 227.

[63] M. Pfeifer, “Degradation and Reliability of Materials,” *Materials Enabled Designs*, pp. 161–187, 2009.

[64] T. Anderson, *Fracture Mechanics*, 3rd ed. Taylor & Francis Group, 2005.

[65] P. Paris and F. Erdogan, “A Critical Analysis of Crack Propagation Laws,” *Journal of Basic Engineering*, 12 1963.

[66] N. Nanninga, A. Slifka, Y. Levy, and C. White, “A Review of Fatigue Crack Growth for Pipeline Steels Exposed to Hydrogen,” *Journal of Research of the National Institute of Standards and Technology*, vol. 115, no. 6, pp. 437–452, 12 2010.

[67] H. Ryan and A. Mehmanparast, “Development of a new approach for corrosion-fatigue analysis of offshore steel structures,” *Mechanics of Materials*, vol. 176, 11 2022.

[68] Y. Momotani, A. Shibata, D. Terada, and N. Tsuji, “Hydrogen Embrittlement Behavior at Different Strain Rates in Low-carbon Martensitic Steel,” *Materials Today: Proceedings*, vol. 2, pp. S735–S738, 1 2015.

[69] A. Hussein, A. H. Krom, P. Dey, G. K. Sunnardianto, O. A. Moultos, and C. L. Walters, “The effect of hydrogen content and yield strength on the distribution of hydrogen in steel: a diffusion coupled micromechanical FEM study,” *Acta Materialia*, vol. 209, p. 116799, 5 2021.

[70] A. J. Slifka, E. S. Drexler, D. G. Stalheim, R. L. Amaro, D. S. Lauria, A. E. Stevenson, and L. E. Hayden, “The Effect of Microstructure on the Hydrogen-Assisted Fatigue of Pipeline Steels,” *American Society of Mechanical Engineers, Pressure Vessels and Piping Division (Publication) PVP*, vol. 6 B, 1 2014.

[71] S. Ounnas, “Hydrogen Storage and Transportation,” 2 2020.

[72] A. J. Slifka, E. S. Drexler, R. L. Amaro, L. E. Hayden, D. G. Stalheim, D. S. Lauria, and N. W. Hrabe, “Fatigue measurement of pipeline steels for the application of transporting gaseous hydrogen,” *Journal of Pressure Vessel Technology, Transactions of the ASME*, vol. 140, no. 1, 2 2018. [Online]. Available: https://asmedigitalcollection.asme.org/pressurevesseltech/article/140/1/011407/449511/Fatigue-Measurement-of-Pipeline-Steels-for-the

[73] "How Wind Energy Can Help Clean Hydrogen Contribute to a Zero-Carbon Future | Department of Energy." [Online]. Available: https://www.energy.gov/eere/articles/how-wind-energy-can-help-clean-hydrogen-contribute-zero-carbon-future

[74] Det Norske Veritas (DNV), "DNV-RP-F114 Pipe-soil interaction for submarine pipelines ," 2021.

[75] "DNV awards AiP for a floating ammonia production unit developed by SWITCH2 and BW Offshore." [Online]. Available: https://www.dnv.com/news/dnv-awards-aip-for-a-floating-ammonia-production-unit-developed-by-switch2-and-bw-offshore--240876

[76] "New offshore export jetty design receives AiP – Ammonia Energy Association." [Online]. Available: https://www.ammoniaenergy.org/articles/new-offshore-export-jetty-design-receives-aip/

[77] C. Wu, S. Zheng, Z. Wang, R. Chen, X. Hu, and J. Chen, "Discussion on ammonia as one of the energy storage media of solar energy in China," *Energy Strategy Reviews*, vol. 38, p. 100697, 11 2021.

[78] J. Plucinska, "Nord Stream gas 'sabotage': who's being blamed and why?" 10 2022. [Online]. Available: https://www.reuters.com/world/europe/qa-nord-stream-gas-sabotage-whos-being-blamed-why-2022-09-30/

[79] J. Capelle, J. Gilgert, and G. Pluvinage, "Hydrogen effect on fatigue and fracture of pipe steels," 1 2009.

[80] D. Bowness and M. M. Lee, "Prediction of weld toe magnification factors for semi-elliptical cracks in T–butt joints," *International Journal of Fatigue*, vol. 22, no. 5, pp. 369–387, 5 2000.